

# Transport of nanoparticles into polymersomes: a minimal model system of particles passage through biological membranes

Dissertation

zur Erlangung des Grades

„Doktor der Naturwissenschaften“ (Dr. rer. nat.)

Max Planck Graduate Center

mit der Johannes Gutenberg-Universität Mainz

Angefertigt am Max-Planck-Institut für Polymerforschung

vorgelegt von

**Karmena Izabela Jaśkiewicz**

geboren am 11.09.1984 in Zgorzelec (Polen)

Mainz, 2012



Max Planck Graduate Center  
mit der Johannes Gutenberg-Universität Mainz



Die vorliegende Arbeit wurde in der Zeit von Oktober 2009 bis September 2012 in der Arbeitsgruppe Physikalische Chemie der Polymere am Max-Planck-Institut für Polymerforschung unter der Anleitung von Prof. K.L., Prof. G.F. und Dr. A.K. angefertigt.

Dekan:

1. Berichterstatter:

2. Berichterstatter:

Tag der mündlichen Prüfung: 19.12.2012

*“And once the storm is over, you won’t remember how you made it through, how you managed to survive. You won’t even be sure, whether the storm is really over. But one thing is certain. When you come out of the storm, you won’t be the same person who walked in. That’s what this storm’s all about.”*

Haruki Murakami

## Zusammenfassung

Die vorliegende Doktorarbeit behandelt die Entwicklung und die Charakterisierung eines neuartigen, künstlichen Minimalmodells eines Membransystems, das den physikalischen Prozess der Nanopartikelaufnahme allein durch Adhäsionskräfte und Elastizität der Membran imitiert. Dieses Minimalmodell besteht zum einen aus Polymersomen, die aus dem Blockcopolymer Poly(dimethylsiloxan)-*Block*-Poly(2-methyloxazolin) (PDMS-*b*-PMOXA) gebildet werden, und zum anderen aus Nanopartikeln (Polystyrol, Silica). Es wurde mit Hilfe von geeigneten Charakterisierungsmethoden untersucht.

Es wurden Polymersome aus PDMS-*b*-PMOXA mit einem Radius ( $R_h$ )  $\sim 100$  nm und einer Größendispersität von  $PD = 1.1$  mittels der Filmbildemethode hergestellt. Die Dicke der Doppelschichtmembran beträgt 16 nm. Aufgrund ihrer mechanischen Eigenschaften (Elastizitätsmodul von  $\sim 17$  MPa und Biegemodul von  $\sim 7 \cdot 10^{-8}$  J), ihrer Langzeitstabilität und ihrer Modifizierbarkeit eignen sich diese Polymersome als Modellmembrane, an denen die physikalischen und physikochemischen Aspekte des transmembranen Transport von Nanopartikeln untersucht wurden. Als Methoden der Wahl wurden dynamische Lichtstreuung (PCS) und Fluoreszenzkorrelationsspektroskopie (FCS) gewählt.

Als Demonstration des Prinzips wurde zuerst die Wechselwirkung zwischen Nanopartikeln ( $R_h$  NP SiO<sub>2</sub> = 14 nm,  $R_h$  NP PS = 16 nm;  $c_{NP} = 0.1$  gL<sup>-1</sup>) und Polymersom ( $R_h$  P = 112 nm;  $c_P = 0.045$  gL<sup>-1</sup>) mit festgelegten Größen und Konzentrationen untersucht. In Lichtstreuexperimenten wurde ein veränderter Formfaktor der Polymersome beobachtet, der die präzise Verfolgung und quantitative Beschreibung des Aufnahmeprozesses ermöglichte. Die Kombination von PCS und FCS erlaubte die Abschätzung der Anzahl der aufgenommenen Partikel pro Polymersom (ca. 8 Partikel) und die Entwicklung einer geeigneten Methodik für die kinetischen und dynamischen Aspekte des Aufnahmeprozesses.

Des Weiteren wurden die experimentellen Ergebnisse mit theoretischen Studien verglichen. Sowohl Größe als auch Konzentration der Nanopartikel wurden als die wichtigsten

Systemvariablen bestimmt ( $R_h \text{ NP} = 14 - 57 \text{ nm}$ ;  $c_{\text{NP}} = 0.05 - 0.2 \text{ gL}^{-1}$ ). Es wurde gezeigt, dass der Aufnahmeprozess maßgeblich durch Variation der Nanopartikelgröße und -Konzentration beeinflusst werden kann. Bei Nanopartikelkonzentrationen von  $0.1 - 0.2 \text{ gL}^{-1}$  wurden durchschnittlich 7 bis 11 Nanopartikel mit  $R_h = 14 \text{ nm}$  und 3 bis 6 Nanopartikel mit  $R_h = 25 \text{ nm}$  in die Polymersome aufgenommen. Der Aufnahmeprozess wurde außerdem nur oberhalb einer kritischen Nanopartikelkonzentration beobachtet, die wiederum abhängig von der Nanopartikelgröße ist.

Mit Hilfe der Cryo-Transmissions-Elektronenmikroskopie (cryo-TEM) wurden zwei unterschiedliche Aufnahmemechanismen gefunden, die von der Größe der eingesetzten Nanopartikel abhängen: gemeinsame Aufnahme von Nanopartikeln in Gruppen oder Aufnahme von einzelnen Nanopartikeln. Es wurden Bedingungen gefunden, unter denen Nanopartikelaufnahme und somit das kontrollierte Füllen von Polymersomen möglich ist.

Im Rahmen dieser Doktorarbeit wurde somit erstmalig der transmembrane Transport von sphärischen Polystyrol- und Silica-Nanopartikeln in Polymersome beobachtet und quantitativ untersucht. Die experimentellen Arbeiten, die dieser Doktorarbeit zu Grunde liegen, werden Einfluss auf die Entwicklung von Zellmodellsystemen haben und dadurch erheblich das Verständnis von transmembranen Transportprozessen verbessern. Die in dieser Arbeit vorgestellten experimentellen Ergebnisse zeigen, dass transmembraner Transport von Nanopartikeln an künstlichen Modellsystemen ohne zusätzliche Impulse möglich ist. Dies hat grundlegenden Einfluss auf das Verständnis des Prozesses der Nanopartikelaufnahme sowie auf die Wechselwirkung von Nanopartikeln mit biologischen und auch polymeren Membranen.

## Abstract

This thesis focuses on the design and characterization of a novel, artificial minimal model membrane system with chosen physical parameters to mimic a nanoparticle uptake process driven exclusively by adhesion and softness of the bilayer. The realization is based on polymersomes composed of poly(dimethylsiloxane)-*b*-poly(2-methyloxazoline) (PMDS-*b*-PMOXA) and nanoscopic colloidal particles (polystyrene, silica), and the utilization of powerful characterization techniques.

PDMS-*b*-PMOXA polymersomes with a radius,  $R_h \sim 100$  nm, a size polydispersity, PD = 1.1 and a membrane thickness,  $h = 16$  nm, were prepared using the film rehydration method. Due to the suitable mechanical properties (Young's modulus of  $\sim 17$  MPa and a bending modulus of  $\sim 7 \cdot 10^{-8}$  J) along with the long-term stability and the modifiability, these kind of polymersomes can be used as model membranes to study physical and physicochemical aspects of transmembrane transport of nanoparticles. A combination of photon (PCS) and fluorescence (FCS) correlation spectroscopies optimizes species selectivity, necessary for a unique internalization study encompassing two main efforts.

For the proof of concepts, the first effort focused on the interaction of nanoparticles ( $R_{h\text{ NP SiO}_2} = 14$  nm,  $R_{h\text{ NP PS}} = 16$  nm;  $c_{\text{NP}} = 0.1$  gL $^{-1}$ ) and polymersomes ( $R_{h\text{ P}} = 112$  nm;  $c_{\text{P}} = 0.045$  gL $^{-1}$ ) with fixed size and concentration. Identification of a modified form factor of the polymersome entities, selectively seen in the PCS experiment, enabled a precise monitor and quantitative description of the incorporation process. Combining PCS and FCS led to the estimation of the incorporated particles per polymersome (about 8 in the examined system) and the development of an appropriate methodology for the kinetics and dynamics of the internalization process.

The second effort aimed at the establishment of the necessary phenomenology to facilitate comparison with theories. The size and concentration of the nanoparticles were chosen as the most important system variables ( $R_{h\text{ NP}} = 14 - 57$  nm;  $c_{\text{NP}} = 0.05 - 0.2$  gL $^{-1}$ ). It was revealed that

the incorporation process could be controlled to a significant extent by changing the nanoparticles size and concentration. Average number of 7 up to 11 NPs with  $R_{h\text{ NP}} = 14$  nm and 3 up to 6 NPs with  $R_{h\text{ NP}} = 25$  nm can be internalized into the present polymersomes by changing initial nanoparticles concentration in the range 0.1- 0.2 gL<sup>-1</sup>. Rapid internalization of the particles by polymersomes is observed only above a critical threshold particles concentration, dependent on the nanoparticle size.

With regard possible pathways for the particle uptake, cryogenic transmission electron microscopy (cryo-TEM) has revealed two different incorporation mechanisms depending on the size of the involved nanoparticles: cooperative incorporation of nanoparticles groups or single nanoparticles incorporation. Conditions for nanoparticle uptake and controlled filling of polymersomes were presented.

In the framework of this thesis, the experimental observation of transmembrane transport of spherical PS and SiO<sub>2</sub> NPs into polymersomes *via* an internalization process was reported and examined quantitatively for the first time.

In a summary the work performed in frames of this thesis might have significant impact on cell model systems' development and thus improved understanding of transmembrane transport processes. The present experimental findings help create the missing phenomenology necessary for a detailed understanding of a phenomenon with great relevance in transmembrane transport. The fact that transmembrane transport of nanoparticles can be performed by artificial model system without any additional stimuli has a fundamental impact on the understanding, not only of the nanoparticle invagination process but also of the interaction of nanoparticles with biological as well as polymeric membranes.

## Acknowledgments

This thesis could not be accomplished without the aid and support of countless people.

I must first express my gratitude towards my advisor K.L. for giving me the opportunity of being a part of her group, for her support and many valuable meetings we had during these past three years.

My special acknowledgments I would like to give to my second advisor G.F. For introducing me to the world of light scattering, for numerous valuable scientific conversations and for his constant help and support I am really grateful. I am additionally thankful for his assistance during writing of my first scientific publications; this added substantial value to their quality.

I would like to acknowledge A.K. for offering me this interesting and challenging topic. For her support and the faith in the success of this project I am especially thankful.

This project would not head into the right direction without the help of W.M. who suggested and provided copolymer with suitable properties. Here I would like to thank also W.M. students: S.E. for the copolymer synthesis and his support with polymersome preparation, D.W. who continued work of S. and S.M. for her help with polymersome preparation and characterization.

A.L. is kindly acknowledged for her support during light scattering experiments and data evaluation. The numerous hours she spent on fitting the PCS data are greatly appreciated.

I would like to thank K.K. for fruitful collaboration and introducing me to the FCS. His help with FCS experiments and data evaluation is greatly valued. At this point I would like to express my gratitude to D.S. for performing FCS experiments and data evaluation presented in my second paper. The contribution of M.K. and M.M. who performed the AFM measurement is particularly appreciated. Additionally I would like to acknowledge M.K. for his help in preparation of the manuscript about polymersome characterization. Work and persistence of I.L. and M.B. on cryo-TEM imaging is deeply appreciated. Plentiful unsuccessful trials finally lead us to the great results. I would also like to thank U.P. for numerous syntheses of PS particles and P.V. for his help with PCS data evaluation. A.K. is acknowledged for her trials on the copolymer synthesis and also for the translation of the English abstract into German.

The assistance and help of polymer analytics group (MPIP) is greatly appreciated. Especially help and support of C.R. and B.M. needs to be acknowledged. C. is kindly acknowledged for her assistance with the measurements and arrangement of the measurement schedule. My special thanks to B. for many hours she spent trying to align the PCS setup.

I would like to acknowledge contribution of R.S. (ellipsometry experiments), G.F. (X-Ray experiments), M.D., M.H. and K.K. (theoretical simulations), S.R. (giant vesicles preparation, microscopy) and A.K. (STED and confocal microscopy) to this project.

Many thanks to my friends who share this time with me and helped me one way or another. My special thanks to (alphabetic order :)): A.B., C.C., L.C., M.D., A.P.D., V.D., H.G., N.G., E.K., M.M., T.R., A.S., A.V., S.V. and S.Y.

Szczególne podziękowania składam moim rodzicom: Irenie i Janowi, braciom: Arkowi i Kamilowi oraz całej mojej rodzinie za nieustanne wsparcie i wiarę we mnie. (*From Polish: Last but not least I would like to express special gratitude to my parents: Irena and Jan, brothers: Arek and Kamil and entire family for the unconditional support and encouragement they were giving me.*)

Είμαι ιδιαίτερα ευγνώμων για την πολύτιμη επιστημονική (και μη) υποστήριξη αλλά και την διαρκή υπομονή του, στον Μάνο. (*From Greek: For sharing this PhD time with me, both scientifically and non-scientifically, constant support and patience I am especially grateful to Manos.*)

## Abbreviations

<b>SOPC</b>	1-stearoyl-2-oleoyl phosphatidylcholine
$R_{VV}$	absolute scattering intensity for the polarized vertical-
<b>ATP</b>	adenosine-5'-triphosphate
$k_{ad}$	adhesion constant
$A$	amplitude of the autocorrelation function
$\alpha_{ir}$	angle between incident and reflected beam (TEM)
$\text{\AA}$	Angstrom
<b>ATRP</b>	atom transfer radical polymerization
<b>AFM</b>	atomic force microscopy
$\psi_i$	average "brightness" of the molecules (FCS)
$N_A$	Avogadro number
$E$	bending energy of a membrane/ Young modulus
$\kappa_B$	bending rigidity
<b>BLM</b>	black lipid membrane
$k_B$	Boltzmann constant
$Z_c$	cantilever deflection
$k_c$	cantilever spring constant
$l$	chain length normal to the interface
<b>CCD</b>	charge-coupled device
$K_a$	compression modulus
$c$	concentration
$k_D$	concentration independent constant (PCS)
$\theta_a$	contact angle
$l_c$	critical length of the hydrophobic chain
<b>CMC</b>	critical micelle concentration
<b>Cryo-TEM</b>	cryogenic transmission electron microscopy
$z$	degree of penetration of the bilayer
$\rho$	density
$\rho_0$	density of the solvent
<b>DNA</b>	deoxyribonucleic acid
$b$	diameter

<b>diAPC</b>	diarachidonyl-phosphatidylcholine
$\Delta\mu$	difference in chemical potential
<b><i>D</i></b>	diffusion coefficient (FCS)
<b>diMPC</b>	dimyristoyl-phosphatidylcholine
<b>DPPC</b>	dipalmitoylphosphatidylcholine
<b>DPD</b>	dissipative particle dynamics
$r_{ij}$	distance between two scattering centers <i>i</i> and <i>j</i>
<b><math>J(\tau)</math></b>	distribution of relaxation times
<b>DLS</b>	dynamic light scattering
<b><math>\Lambda</math></b>	edge energy
<b>EggPC</b>	egg yolk phosphatidylcholine
<b><i>F</i></b>	energy density
<b><math>C(q,t)</math></b>	field autocorrelation function
<b><math>j_1(x)</math></b>	first-order spherical Bessel function
<b><math>\chi</math></b>	Flory-Huggins parameter
<b><math>F(t)</math></b>	fluctuations of the fluorescence intensity
<b>FCS</b>	fluorescence correlation spectroscopy
<b><math>P(q)</math></b>	form factor
$\Phi_{\text{NPs}}$	fraction of nanoparticles
<b><math>f_i</math></b>	fraction of the <i>i</i> -th type of species
$\Phi_2$	fraction of water inside polymersomes
<b><math>R_{\text{gas}}</math></b>	gas constant
<b><math>\kappa_G</math></b>	Gaussian bending rigidity
<b><math>H</math></b>	Gaussian curvature
<b>GUV</b>	giant unilamellar vesicle
<b><math>T_g</math></b>	glass transition temperature
<b><math>Y</math></b>	height of a vesicle adsorbed on the surface
<b><math>v^*</math></b>	hydrophobic volume of the molecule
<b><math>k_i</math></b>	incident beam vector
<b><math>G(q,t)</math></b>	intensity autocorrelation function
<b><math>I_{\text{sol}}</math></b>	intensity of the solution
<b><math>I_{\text{solv}}</math></b>	intensity of the solvent
<b><math>u</math></b>	interfacial area
<b>KWW</b>	Kohlrausch-Williams-Watts

$\lambda_0$	laser wavelength
$s$	length scale
$m_i$	mass of particle $i$
$M_w$	mass weighted molecular weight
$K$	mean curvature
$A^*$	measured baseline (PCS)
$M_0$	molar mass of the solvent
$C_i$	molecular concentration
<b>PMI</b>	N-(2,6-Diisopropylphenyl)-perylene-3,4-dicarbonacidimide
<b>NPs</b>	nanoparticles
$c_{NP}$	nanoparticles concentration
$R_p$	n-average polymersome outer radius
$\bar{r}$	number average size of the particle
$R_n$	number averaged radius
$x$	number of hydrophobic molecules
$N_i$	number of individual molecules within that volume
$N$	number of molecules within the volume
$V$	observation volume
$K_o$	optical constant (PCS)
$a_0$	optimal surface area per molecules at interface
$\Pi$	osmotic pressure
$p$	packing parameter
$m$	parameter that measures the width of the distribution
<b>PCS</b>	photon correlation spectroscopy
$\nu_p$	Poisson ratio
$\alpha$	polarizability
<b>PMOXA</b>	poly(2-methyloxazoline)
<b>PAA</b>	poly(acrylic acid)
<b>PDMS</b>	poly(dimethylsiloxane)
<b>PS</b>	poly(styrene)
<b>PMCL-<i>b</i>-PAA</b>	poly( $\gamma$ -methyl- $\epsilon$ -caprolactone)- <i>b</i> -poly(acrylic acid)
<b>PB-<i>b</i>-PEO</b>	polybutadiene- <i>b</i> - poly(ethylene oxide)
<b>PDI/PD</b>	polydispersity index
$c_p$	polymer concentration

<b>PS-<i>b</i>-PEO</b>	polystyrene- <i>b</i> -poly(ethylene oxide)
<b><math>Z_p</math></b>	position of the piezotranslator
<b>KPS</b>	potassium persulfate
<b><math>R_1, R_2</math></b>	radii of curvature
<b><math>a</math></b>	radius of a colloidal particle
<b><math>R_v</math></b>	radius of a sphere
<b><math>R_{CV}</math></b>	radius of curvature of the vesicle
<b><math>R_g</math></b>	radius of gyration
<b><math>\zeta</math></b>	ratio between adhesion constant and tension constant
<b>RGD</b>	Rayleigh- Gantz -Debye scattering
<b><math>R_{tol}</math></b>	Rayleigh ratio for toluene
<b><math>n</math></b>	refractive index
<b><math>n_P</math></b>	refractive index of polymer
<b><math>n_{IN}</math></b>	refractive index of polymersome interior
<b><math>n_B</math></b>	refractive index of the bilayer
<b><math>n_0</math></b>	refractive index of the polymersomes external environment
<b><math>\Gamma</math></b>	relaxation rate
<b><math>\tau_D</math></b>	relaxation time
<b><math>\delta</math></b>	resolution
<b>rpm</b>	rotation per minute
<b><math>I(q)</math></b>	scattered intensity
<b><math>\theta</math></b>	scattering angle
<b><math>k_s</math></b>	scattering beam vector
<b><math>q</math></b>	scattering wave vector
<b><math>A_2</math></b>	second virial coefficient
<b><math>\beta_{KWW}</math></b>	shape parameter (PCS)
<b><math>\mu^*</math></b>	shear modulus
<b>SEC</b>	size exclusion chromatography
<b>SUV</b>	small unilamellar vesicle
<b>SDS</b>	sodium dodecyl sulfonate
<b><math>f^*</math></b>	spatial coherence factor (PCS)
<b><math>dn/dc</math></b>	specific refractive index increment
<b>SLS</b>	static light scattering
<b><math>S</math></b>	structure parameter

<b>SPR</b>	surface plasmon resonance
$\gamma$	surface tension
$T$	temperature
$d$	thickness of the membrane
$A_3$	third virial coefficient
$B$	tip-sample separation
$D_t$	translational diffusion coefficient
$R_0$	vesicle radius before nanoparticle incorporation
$\mu$	viscosity
$K_v$	volume compression modulus
$V_{\text{eff}}$	volume of the fluorescence detection
$V_{\text{site}}$	volume per site
$\lambda_e$	wavelength of electrons
$\lambda_r$	wavelength of the radiation
<b>wt %</b>	weight percent
$W$	width of a vesicle adsorbed on the surface
$m$	width of the distribution
$E$	Young Modulus
$R_h$	z-average hydrodynamic radius
$D_0$	zero angle/concentration diffusion coefficients

# *Table of Contents*

Zusammenfassung .....	vii
Abstract.....	ix
Acknowledgments .....	xi
Abbreviations.....	xiii
<b>Chapter 1. Introduction .....</b>	<b>5</b>
<b>Chapter 2. Motivation .....</b>	<b>9</b>
<b>Chapter 3. Theoretical Fundamentals .....</b>	<b>11</b>
3.1 Amphiphiles and Self Assembly Principles .....	12
3.1.1 Phospholipids .....	12
3.1.2 Block Copolymers .....	13
3.1.3 Self-Assembly Principles and Bilayer Formation .....	15
3.2 The Cell Membrane .....	20
3.2.1 Structure of the Cell Membrane .....	20
3.2.1 Mechanical Properties of the Cell Membrane .....	22
3.3 Cell Membrane Models .....	25
3.3.1 Black Lipid Bilayers (BLM) .....	26
3.3.2 Vesicles (Liposomes, Polymersomes).....	28
3.3.3 Supported Bilayers .....	30
3.3.4 Polymer Cushioned (Tethered) Bilayers .....	31

3.4	Transmembrane Transport.....	33
3.4.1	Passive Diffusion.....	35
3.4.2	Primary and Secondary Active Transport .....	35
3.4.3	Bulk Transport - Endocytosis.....	36
3.5	Theoretical Model of Transmembrane Transport.....	39
3.6	Characterization Methods.....	44
3.6.1	Photon Correlation Spectroscopy (PCS) .....	44
3.6.2	Basic Principles of Fluorescence Correlation Spectroscopy (FCS) .....	54
3.6.3	Basic Principles of Atomic Force Microscopy (AFM).....	57
3.6.4	Basic Principles of Transmission Electron Microscopy (TEM).....	61
3.7	References .....	64
<b>Chapter 4.</b>	<b>Experimental Section .....</b>	<b>71</b>
4.1	Materials .....	72
4.1.1	Block Copolymer Synthesis.....	72
4.1.2	Polymersomes Preparation.....	73
4.1.3	Fluorescent Polystyrene Nanoparticles .....	75
4.1.4	SiO <sub>2</sub> Nanoparticles.....	76
4.1.5	Polymersome/Nanoparticle Mixture Preparation .....	76
4.2	Instrumentation.....	78
4.2.1	Photon Correlation Spectroscopy (PCS) Measurements .....	78
4.2.2	Fluorescence Correlation Spectroscopy (FCS) Measurements .....	78

4.2.3	Atomic Force Microscopy (AFM) Measurements.....	80
4.2.4	Transmission Electron Microscopy (TEM) Measurements .....	82
4.2.5	Zeta - Potential Measurements .....	82
4.3	References .....	83
<b>Chapter 5. Results and Discussion .....</b>		<b>85</b>
	<i>Outline</i> .....	86
5.1	Designing of the Model System .....	89
5.1.1	Selection of Vesicle Forming Block Copolymers .....	90
5.1.1	Nanoparticles Selection .....	96
5.1.2	Justification of the Materials Selection .....	97
5.1.3	Characterization Methods with the Focus on the Application to the Presented Model.....	98
5.2	Characterization of Polymersomes and Colloidal Nanoparticles .....	101
5.2.1	PDMS- <i>b</i> -PMOXA Polymersomes Characterization.....	102
5.2.2	Polystyrene and Silica Nanoparticles Characterization.....	119
5.3	Probing Incorporation of Nanoparticles into Polymersomes .....	122
5.3.1	Cryo-TEM.....	124
5.3.2	Photon Correlation Spectroscopy (PCS) .....	125
5.3.3	Fluorescence Correlation Spectroscopy (FCS) .....	129
5.4	Incorporation of Silica Nanoparticles into Polymersomes: Size and Concentration Effects .....	131
5.4.1	Threshold Concentration .....	133

5.4.2	Concentration Dependence .....	136
5.4.3	Size Dependence.....	140
5.5	References .....	152
<b>Chapter 6.</b>	<b>Summary and Outlook.....</b>	<b>155</b>
	Curriculum Vitae and Publications .....	158
	Declaration.....	161
	Appendix.....	163
1.	Nanoparticles Used in Presented Studies .....	163
2.	Stability of PDMS- <i>b</i> -PMOXA Polymersomes at Different Temperatures .....	163
3.	Influence of the pH on the PDMS- <i>b</i> -PMOXA Polymersomes Stability.....	164

## Chapter 1. Introduction

One of the most important functions of a living cell is the selective transport of ions, molecules, or colloidal particles across the hydrophobic bilayer from the extracellular environment to the cell interior mediated by different endocytic machineries.<sup>1</sup> Mechanochemistry of such coordinated processes fascinated scientists for over a century, but we are still far from a comprehensive description.<sup>2-6</sup> Whereas in biology the term endocytosis refers to mechanisms of incorporation of molecules and particles via an invagination process assisted by bio-functional molecules and/or supplementary energy, recent studies have revealed the existence of non-endocytic pathways for nanoscaled objects.<sup>7-10</sup>

The mechanisms behind endocytosis are an object of intensive theoretical simulations,<sup>11-18</sup> while experimental studies are very limited due to the complexity of the cellular system and paucity of powerful techniques.<sup>19, 20</sup> The growing field of engineered nanosized particles for biomedical application,<sup>21, 22</sup> which are mainly taken up utilizing endocytic pathways, is still intuitive due to the lack of detailed understanding of the incorporation mechanisms.<sup>23, 24</sup>

It has been reported both theoretically and experimentally that nanoparticle uptake is strictly size and shape dependent.<sup>25, 26</sup> The size of the nanoparticles does not only influence the uptake mechanisms but also nanoparticle toxicity.<sup>27-29</sup> Influence of the nanoparticle surface on the uptake mechanism<sup>30</sup> and cell toxicity<sup>31</sup> was also reported.

In order to take the full advantages of nanoparticles as drug delivery agents, like high stability, high carrier stability, possibility of variety substances incorporation or controlled release from nanoparticles,<sup>27</sup> all relations between them and the human body have to be encrypted and fully understood.

## References

1. Conner, S. D.; Schmid, S. L., Regulated portals of entry into the cell. *Nature* **2003**, *422*, 37-44.
2. Liu, J.; Sun, Y.; Oster, G. F.; Drubin, D. G., Mechanochemical crosstalk during endocytic vesicle formation. *Curr. Opin. Cell Biol.* **2010**, *22*, 36-43.
3. Marsh, M.; McMahon, H., The structural era of endocytosis. *Science* **1999**, *285*, 215.
4. Jiang, W.; Kim, B. Y. S.; Rutka, J. T.; Chan, W. C. W., Nanoparticle-mediated cellular response is size-dependent. *Nature Nanotech.* **2008**, *3*, 145-150.
5. Cho, E. C.; Zhang, Q.; Xia, Y., The effect of sedimentation and diffusion on cellular uptake of gold nanoparticles. *Nature Nanotech.* **2011**, *6*, 385-391.
6. Summers, H. D.; Rees, P.; Holton, M. D.; Brown, M. R.; Chappell, S. C.; Smith, P. J.; Errington, R. J., Statistical analysis of nanoparticle dosing in a dynamic cellular system. *Nature Nanotech.* **2011**, *6*, 170-174.
7. Merrifield, C. J.; Feldman, M. E.; Wan, L.; Almers, W., Imaging actin and dynamin recruitment during invagination of single clathrin-coated pits. *Nat. Cell Biol.* **2002**, *4*, 691-698.
8. Jonsdottir, G. A.; Li, R., Dynamics of Yeast Myosin I: Evidence for a Possible Role in Scission of Endocytic Vesicles. *Curr. Biol.* **2004**, *14*, 1604-1609.
9. Rothen-Rutishauser, B. M.; Schürch, S.; Haenni, B.; Kapp, N.; Gehr, P., Interaction of fine particles and nanoparticles with red blood cells visualized with advanced microscopic techniques. *Environ. Sci. Technol.* **2006**, *40*, 4353-4359.
10. Liu, C.; Zhen, X.; Wang, X.; Wu, W.; Jiang, X., Cellular entry fashion of hollow milk protein spheres. *Soft Matter* **2011**.
11. Illya, G.; Lipowsky, R.; Shillcock, J., Effect of chain length and asymmetry on material properties of bilayer membranes. *J. Chem. Phys.* **2005**, *122*, 244901.
12. Fošnarič, M.; Iglič, A.; Kroll, D. M.; May, S., Monte Carlo simulations of complex formation between a mixed fluid vesicle and a charged colloid. *J. Chem. Phys.* **2009**, *131*, 105103.
13. Dietrich, C.; Angelova, M.; Pouligny, B., Adhesion of latex spheres to giant phospholipid vesicles: statics and dynamics. *J. Phys. II* **1997**, *7*, 1651-1682.
14. Deserno, M.; Gelbart, W. M., Adhesion and wrapping in colloid-vesicle complexes. *J. Phys. Chem. B* **2002**, *106*, 5543-5552.
15. Deserno, M.; Bickel, T., Wrapping of a spherical colloid by a fluid membrane. *Europhys. Lett.* **2003**, *62*, 767.
16. Yue, T.; Zhang, X., Cooperative Effect in Receptor-Mediated Endocytosis of Multiple Nanoparticles. *ACS nano* **2012**, *6*, 3196-3205.
17. Smith, K. A.; Jasnow, D.; Balazs, A. C., Designing synthetic vesicles that engulf nanoscopic particles. *J. Chem. Phys.* **2007**, *127*, 084703.
18. Lipowsky, R.; Döbereiner, H. G., Vesicles in contact with nanoparticles and colloids. *Europhys. Lett.* **1998**, *43*, 219.
19. Le Bihan, O.; Bonnafous, P.; Marak, L.; Bickel, T.; Trépout, S.; Mornet, S.; De Haas, F.; Talbot, H.; Taveau, J. C.; Lambert, O., Cryo-electron tomography of nanoparticle transmigration into liposome. *J. Struct. Biol.* **2009**, *168*, 419-425.

20. Jaskiewicz, K.; Larsen, A.; Lieberwirth, I.; Koynov, K.; Meier, W.; Fytas, G.; Kroeger, A.; Landfester, K., Probing Bioinspired Transport of Nanoparticles into Polymersomes. *Angew. Chem. Int. Ed.* **2012**, *124*, 4691-4695.
21. Michalet, X.; Pinaud, F.; Bentolila, L.; Tsay, J.; Doose, S.; Li, J.; Sundaresan, G.; Wu, A.; Gambhir, S.; Weiss, S., Quantum dots for live cells, in vivo imaging, and diagnostics. *Science* **2005**, *307*, 538.
22. Cao, Y. W. C.; Jin, R.; Mirkin, C. A., Nanoparticles with Raman spectroscopic fingerprints for DNA and RNA detection. *Science* **2002**, *297*, 1536.
23. Nel, A. E.; Mädler, L.; Velegol, D.; Xia, T.; Hoek, E. M. V.; Somasundaran, P.; Klaessig, F.; Castranova, V.; Thompson, M., Understanding biophysicochemical interactions at the nano-bio interface. *Nat. Mater.* **2009**, *8*, 543-557.
24. Yan, Y.; Such, G. K.; Johnston, A. P. R.; Best, J. P.; Caruso, F., Engineering Particles for Therapeutic Delivery: Prospects and Challenges. *ACS nano* **2012**, *6* 3663-3669.
25. Chithrani, B. D.; Chan, W. C. W., Elucidating the mechanism of cellular uptake and removal of protein-coated gold nanoparticles of different sizes and shapes. *Nano Lett.* **2007**, *7*, 1542-1550.
26. Chithrani, B. D.; Ghazani, A. A.; Chan, W. C. W., Determining the size and shape dependence of gold nanoparticle uptake into mammalian cells. *Nano Lett.* **2006**, *6*, 662-668.
27. Fadeel, B.; Garcia-Bennett, A. E., Better safe than sorry: Understanding the toxicological properties of inorganic nanoparticles manufactured for biomedical applications. *Adv. Drug Del. Rev.* **2010**, *62*, 362-374.
28. Jahnen-Dechent, W.; Simon, U., Function follows form: shape complementarity and nanoparticle toxicity. *Nanomedicine* **2008**, *3*, 601.
29. Schmid, G., The relevance of shape and size of Au<sub>55</sub> clusters. *Chem. Soc. Rev.* **2008**, *37*, 1909-1930.
30. Dausend, J.; Musyanovych, A.; Dass, M.; Walther, P.; Schrezenmeier, H.; Landfester, K.; Mailänder, V., Uptake mechanism of oppositely charged fluorescent nanoparticles in HeLa cells. *Macromol. Biosci.* **2008**, *8*, 1135-1143.
31. Goodman, C. M.; McCusker, C. D.; Yilmaz, T.; Rotello, V. M., Toxicity of gold nanoparticles functionalized with cationic and anionic side chains. *Bioconjugate Chem.* **2004**, *15*, 897-900.

## *Chapter 2. Motivation*

Due to the rapidly growing field of nanoparticles in therapeutic applications, understanding and controlling the interaction between nanoparticles and membranes is of great importance. Despite enormous effort which was put to decode transport routes through biological membranes our perception of this process is still elusive. The main difficulty arises from the structure of the biological membrane itself. Highly complex assembly of lipids, proteins and additional biological molecules which are involved in a number of processes make direct investigations very difficult. While introduced to a living system, the faith of a nanoparticle crucially depends on the size, shape and concentration that it possesses. However, these truly physical properties cannot be studied separately in the living system, as they are always assisted by the bio-chemical processes.

Decoding of the nanoparticle uptake routes and factors determining the incorporation process can be only achieved by combining the studies performed on artificial as well as biological systems. As the studies inside living cells is a mature field already, the contribution coming from artificial model systems is still minute. This knowledge, however, is necessary to design precise engineered nanoparticles with known dose and toxicity.

Therefore the main motivation of this thesis was to create a new possibility of studying nanoparticle internalization processes on the basis of an artificial model system and open a new pathway for the fundamental understanding, and hence control, of nanoparticle uptake processes in living cells. Utilization of such artificial model systems and characterization methods has important implications for studies of physical and chemical aspects of transmembrane transport processes. Such investigations hardly implemented on natural membranes can be performed in

simple model systems, yielding important insights on the parameters and pathways for nanoparticle uptake.

The main aim of this thesis was to uncouple physico-chemical and biological interactions during incorporation and characterize the process driven only by the physicochemical forces. To achieve this goal the studies described in this thesis are performed in the basis of simplified minimal model system.

To make the system accessible to powerful spectroscopy techniques and represented by long-term stability unspecified polymersomes were selected as the model membrane. Polymersomes in contrast to other available model membranes are more stable and due to the nature of block copolymers, their properties can be tuned in a wide range. While biological molecules like proteins or cholesterol are not present, polymersomes are able to mimic selectively the physicochemical properties of the membrane. This allows successful uncoupling of physico-chemical and biological contributions. Moreover, due to their spherical shape they are closer to the cells than planar bilayers. Reduced size of polymersomes ( $R_h \sim 100\text{nm}$ ) favors them over almost macroscopic size cells and opens a pathway to characterization techniques like photon (PCS) or fluorescence correlation spectroscopy (FCS). These powerful techniques allow studies of both dynamics and kinetics of the process in a real time with large number of individual structures being evaluated statistically.

Description of the polymersomes / nanoparticles interactions would lead to better understanding of the invagination process as well as nanoparticle-membrane complex interactions. Studies performed on artificial system, described in this thesis, are a significant contribution to the full enlightenment of nanoparticle uptake by living cells.

## *Chapter 3. Theoretical Fundamentals*

Basic principles of self-assembly of amphiphilic molecules phenomenon, the basis for the formation of biological membranes, are discussed in this section. In particular, structure and properties of both lipid and block copolymer and their influence on self-assembled structures are presented. Further, the structure of the cell membrane is discussed with emphasis on its mechanical properties which strongly influence the transmembrane transport. Main artificial models of cell membrane are outlined and their advantages and disadvantages are pointed out. Major routes of transmembrane transport are shortly discussed with the link to their theoretical models giving direct link to the subject of the present study: the development of an artificial model system of nanoparticles transmembrane transport.

## 3.1 Amphiphiles and Self Assembly Principles

### 3.1.1 Phospholipids

Lipids<sup>1-3</sup> are a special kind of amphiphiles (from Greek: having an affinity for both) which consist typically of two fatty acid chains linked by ester or acyl bonds to a common backbone (see *Figure 3.1*). Glycerol-based lipids are the most commonly found lipids in nature with phospholipids being the key-component of the cell membrane.

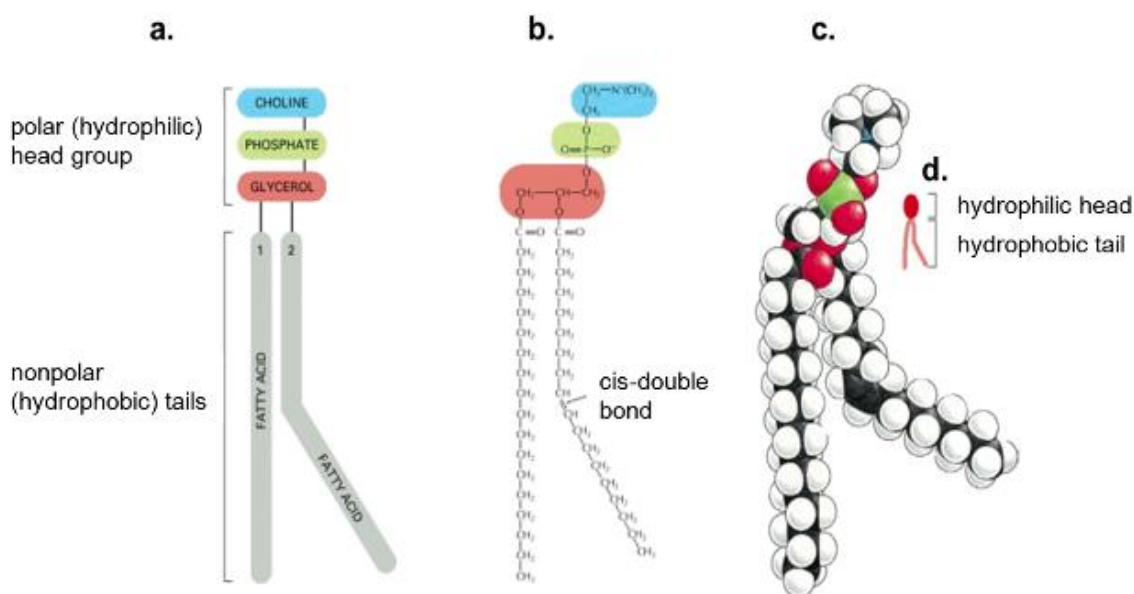


**Figure 3.1** The parts of a phospholipid molecule (phosphatidylcholine) represented **a.** schematically, **b.** by a formula, **c.** as a space-filling model, and **d.** as a symbol. The kink resulting from the *cis*-double bond is exaggerated for emphasis.<sup>4\*</sup>

Phospholipids are built from two main components: the hydrophilic “head” and the hydrophobic “tail”. The hydrophilic (from the Greek: *hydros*, meaning water, and *philia*, meaning friendship) head is attracted to water while the hydrophobic (from Greek: *phobos*:

\* Alberts B, Bray D, Lewis J, et al. *Molecular Biology of the Cell*. 3rd edition. New York: Garland Science; 1994. The Lipid Bilayer 1. Available from: <http://www.ncbi.nlm.nih.gov/books/NBK28414/>

meaning fear) tail is repelled by water and is forced to aggregate or more precisely to self-organize. The hydrophilic head contains the negatively charged phosphate group, and may contain other polar groups. The hydrophobic tail usually consists of long fatty acid hydrocarbon chains.

When introduced into water, phospholipids form a variety of structures (including micelles and vesicles) depending on the specific properties of the phospholipid and experimental conditions.<sup>5</sup> These specific properties allow phospholipids to play an important role in the phospholipid bilayer. In biological systems, the phospholipids often occur with other molecules (e.g., proteins, glycolipids, cholesterol) in a bilayer such as a cell membrane.<sup>6, 7</sup> Lipid bilayers occur when hydrophobic tails line up against one another, forming a membrane hydrophilic heads on both sides facing the water. When this bilayer rolls up and form a spherical hollow shell structure it is called a liposome.<sup>5</sup>

### 3.1.2 Block Copolymers

A polymer is a large molecule composed of repeating structural units called monomers. These low molecular weight monomers are typically connected by covalent chemical bonds to form a high molecular weight macromolecule. Polymers, based on their architecture, can be classified as linear polymers, branched polymers, and dendrimers.<sup>8</sup>

When polymers are formed from one type of monomer, they are called homopolymers (*Figure 3.2a*) in contrast to copolymers which are built from more than one type of monomer. The sequence of repeat units in a polymer chain let us classify copolymers as alternating (*Figure 3.2b*), random (*Figure 3.2c*), block (*Figure 3.2d*), and grafted (*Figure 3.2e*).

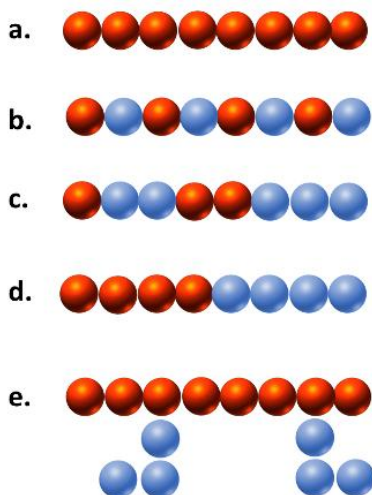


**Figure 3.2** Schematic representation of different structures of homopolymers and copolymers **a.** homopolymers; **b.** alternating copolymer; **c.** random copolymer; **d.** block copolymer; **e.** grafted copolymer.

Amphiphilic block copolymers consisting of a hydrophobic and a hydrophilic block are analogs of lipids as they can self-assemble into equivalent structures. From this point of view they are fascinating materials which can mimic lipid membranes having all the advantages of polymers, like increased stability, molecular weight adjustable in a wide range and improved chemical stability.<sup>9-11</sup>

Block copolymers consist of at least two different segments of homopolymers. Most polymers are incompatible above a certain molecular weight and due to the chemical attachment of the segments this leads to microphase separation.<sup>12</sup> As a result, depending on the relative volume fractions of the blocks, the whole spectrum of morphologies was observed for this type of polymers in bulk. These structures include spheres, lamellae, hexagonally packed cylinders, gyroids and other biocontinuous structures.<sup>13</sup> The phase behavior of the block copolymers in the bulk is controlled by the overall degree of polymerization, the Flory–Huggins interaction parameter, and the volume fraction of the components.<sup>13</sup>

For amphiphilic block-copolymers the tendency to phase separate manifests itself not only as micro-phase separation in bulk but also as self-assembly in solution.

In solution, the formation of block copolymer aggregates of various morphologies is controlled by a force balance between three different factors: the degree of stretching of the core-forming blocks, the interfacial tension between the micelle core and the solvent outside the core, and the repulsive interactions among corona forming chains.<sup>14, 15</sup> Structure analogous to liposomes (see 3.1.1) but consisting of amphiphilic block copolymers are known as polymersomes.<sup>16</sup>

### 3.1.3 Self-Assembly Principles and Bilayer Formation

Both surfactants and amphiphilic block copolymers are able to aggregate while introduced into aqueous media if their concentration is above a threshold value called critical micelle concentration (CMC). Depending on the moiety concentration, temperature and composition/geometry of hydrophobic and hydrophilic segments, micelles, vesicles or lyotropic liquid crystalline phases are formed, as shown schematically in *Figure 3.3*.<sup>5, 17</sup>

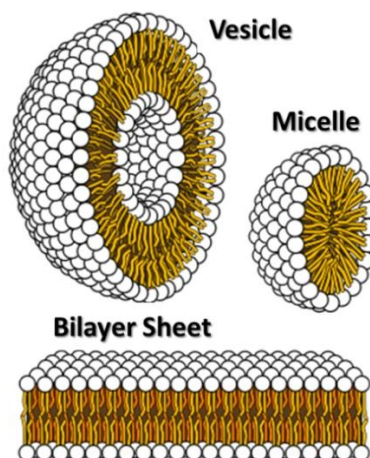


**Figure 3.3** Different self-assembled structures of amphiphilic molecules formed in solution.<sup>†</sup>

<sup>†</sup> Source of the picture: WIKIPEDIA

This selective agglomeration can be well explained by co called “hydrophobic effect” first described by Walter Kauzmann.<sup>18</sup> Briefly, the hydrophobic effect can be explained as tendency of hydrophobic substances to aggregate in aqueous medium and exclude water molecules. The introduction of hydrophobic species into water causes higher ordering of the surrounding water molecules. While  $x$  hydrophobic molecules are free in the aqueous media, the overall solvation free energy is  $x$  times the sum of the solvation free energy for any one of the molecule, and it grows linearly with the overall excluded volume of the solutes. Aggregation of these molecules changes the solvation free energy which is no longer growing linearly with the solvated volume but is growing linearly with the solvated surface area. This effect results in a favorable driving force for the cluster assembly. Simply, the cluster formation leads to a reduced contact of the molecule with neighboring water molecules.<sup>19</sup> Clustering lowers the number of objects in the system, and hence reduces the overall entropy. In this sense the agglomeration process is a result of competition between energy, which favors the formation of clusters, and entropy, which favors the distribution of molecules in the system.<sup>20</sup>

### 3.1.3.1 Principles of Vesicle Formation

Vesicles are a result of a two-step self-assembly process during which amphiphiles first form bilayers which subsequently close forming a vesicle.

The final shape of self-assembled moieties is determined by the molecular packing parameter which is defined as:

$$\frac{v^*}{ul} = 1 + Hl + \frac{Kl^2}{3}$$

**Equation 3.1**

where  $v^*$  is the hydrophobic volume of the molecule,  $u$ : the interfacial area and  $l$  is the chain length normal to the interface;  $H$  is the mean curvature and  $K$  its Gaussian curvature, both given by the two radii of curvature  $R_1$  and  $R_2$ :<sup>‡</sup>

$$H = \frac{1}{2} \left( \frac{1}{R_1} + \frac{1}{R_2} \right) \quad \text{Equation 3.2}$$

$$K = \frac{1}{R_1 R_2} \quad \text{Equation 3.3}$$

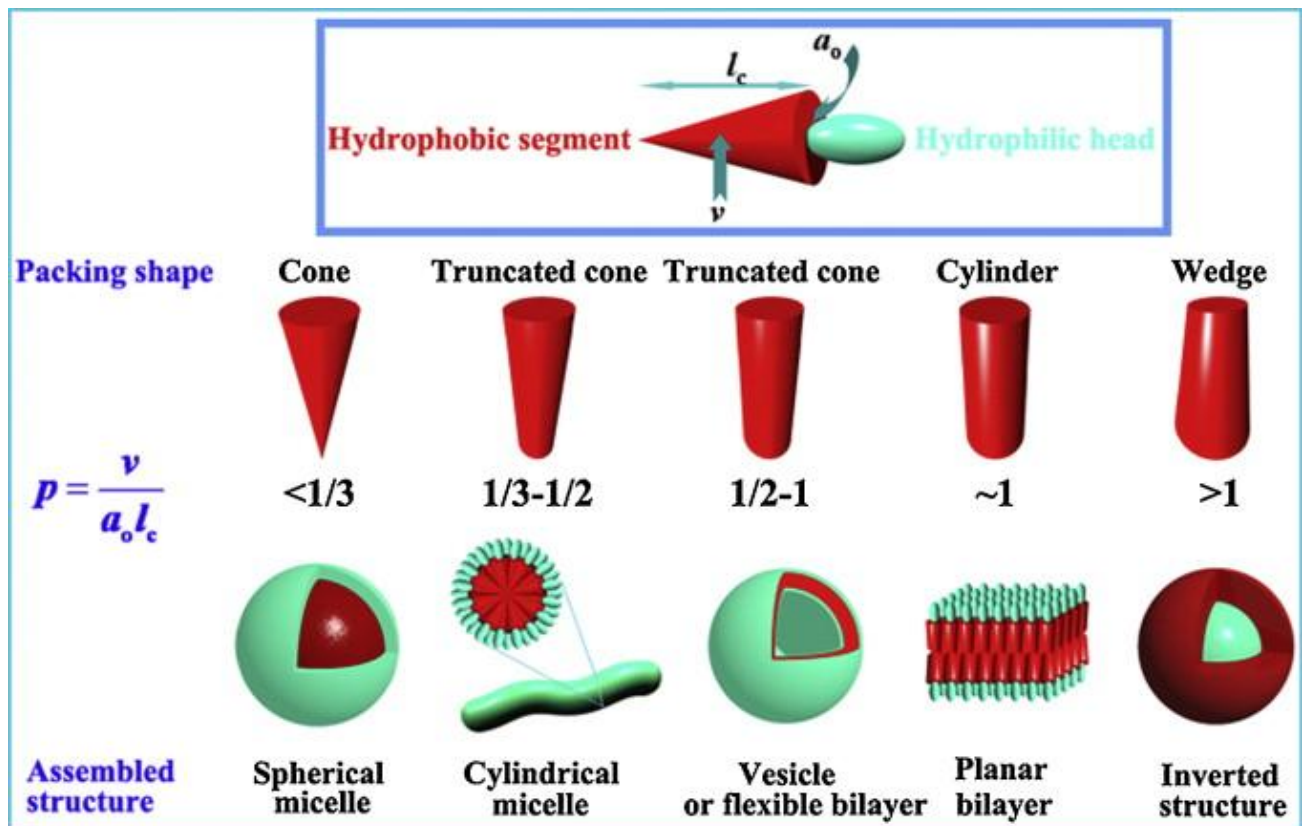


**Figure 3.4** The effect of the packing parameter  $p$  on the structures of assemblies formed (used with permission of Elsevier from Zhang, J.; Li, X., *Stimuli-Triggered Structural Engineering of Synthetic and Biological Polymeric Assemblies*. *Prog. Polym. Sci.* 2011).<sup>21, 22</sup>

<sup>‡</sup> Since sphere is a special case, two curvature parameters are needed to describe the surface.<sup>20</sup> Boal, D., *Mechanics of the Cell*. Cambridge Univ Pr: 2011.

By calculating the molecular packing parameter (or shape factor)  $p$  one can predict the structure of amphiphiles being formed or one can adjust block lengths to form desired morphologies (see *Figure 3.4*):<sup>23</sup>

$$p = \frac{v^*}{a_0 l_c} \quad \text{Equation 3.4}$$

here  $a_0$  is the optimal surface area per molecule at the interface and  $l_c$  is the critical length of the hydrophobic chain.

Closing of the planar bilayer to a vesicular structure as presented schematically in *Figure 3.5* can be described as an interplay between the energy required to bend the bilayer and the interfacial energy, associated with the formation of a large opening in the vesicle exposing the hydrophobic interior to water.<sup>6</sup> A parallel arrangement of molecules is an energetically preferable state. When, however, the sheet-like structures are large enough, the huge energy loss due to the surface tension can be compensated by the closure of this “flat” (planar) structure. Disc formation and “vesicle closing” are intermediate and mostly unstable states in this process.

The bending energy  $E_{\text{sphere}}$  required to transform a planar membrane into a spherical shape object does not depend on the sphere radius and it is represented by:<sup>20</sup>

$$E_{\text{sphere}} = 4\pi(2\kappa_B + \kappa_G) \quad \text{Equation 3.5}$$

$\kappa_b$  and  $\kappa_G$  are the bending rigidity and the Gaussian bending rigidity, respectively.

The energy of a flat disc is represented by:

$$E_{\text{disk}} = 4\pi R_V \Lambda \quad \text{Equation 3.6}$$

$R_v$  is the radius of the formed disk and  $\Lambda$  is the edge tension.

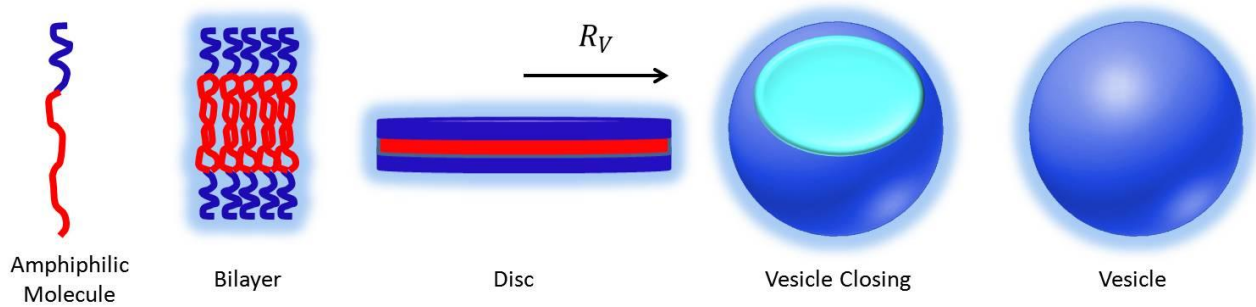


**Figure 3.5** Schematic representation of the vesicle formation process.<sup>23</sup>

At zero temperature the shape of the membrane depends only on the lowest energy which could be achieved by adopting this shape. If  $R_v$  is small, the energy of the disc is small and thus the disc is the preferred orientation. As can be concluded from *Equation 3.7* the energy of the disc increases with  $R_v$  and above certain value of  $R_v$  the spherical shape cost less energy than the disc. If no additional energy barriers are present, the critical  $R_v$  is represented by:

$$R_V^* = (2\kappa_B + \kappa_G)/\Delta$$

**Equation 3.7**

## 3.2 The Cell Membrane

### 3.2.1 Structure of the Cell Membrane

The main function of a cell membrane is to create boundaries between the cell interior and external environment. Moreover, one of the main features of the cell membrane is the so called selective permeability which allows the entire control of the molecules and ions entering and leaving the cell.<sup>24</sup>

Biological membranes<sup>1, 25-27</sup> consist of a continuous double layer of lipid molecules assisted by embedded membrane proteins, as illustrated in *Figure 3.6*. Out of the large number of available lipids nature uses only a few classes of them to build cell membranes, mainly phospholipids, cholesterol, and glycolipids. The lipid compositions of the inner and outer monolayers are different in both structure and composition, reflecting the different functions of the two faces of a cell membrane. The structure of a cell membrane is well described by the fluid mosaic model proposed by S.J. Singer and G.L. Nicolson in 1972 according to which “cell membranes are viewed as two-dimensional solutions of oriented globular proteins and lipids”.<sup>24</sup>

28

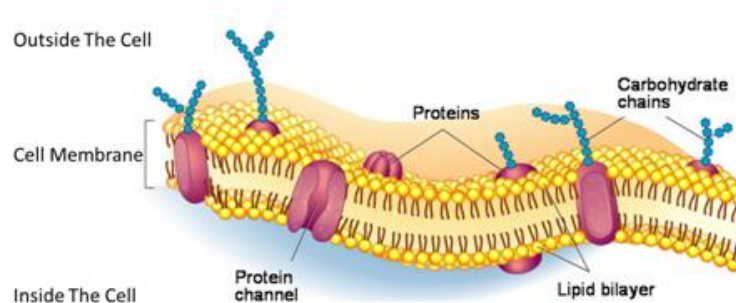


**Figure 3.6** Schematic illustration of animal cell membrane structure. Membrane proteins (dark pink) are embedded inside double lipid layer.<sup>§</sup>

<sup>§</sup> Source of the graphics: [www.goldiesroom.org](http://www.goldiesroom.org)

The entire membrane is held together via non-covalent interactions of the hydrophobic tails; however the structure is quite fluid and not fixed rigidly in place.

Under physiological conditions phospholipid molecules in the cell membrane are in the liquid crystalline state. It means that the lipid molecules are free to diffuse and exhibit a rapid lateral diffusion along the layer in which they are present. It is also known that individual lipid molecules rotate very rapidly about their long axis and that their hydrocarbon chains are flexible. Possible movements of the individual lipids inside the lipid bilayer are presented schematically in *Figure 3.7*. In contrast, the exchange of phospholipid molecules between intracellular and extracellular leaflets of the bilayer is not very common. This process, known as "flip-flop", occurs less than once a month for any individual molecule.<sup>20</sup>

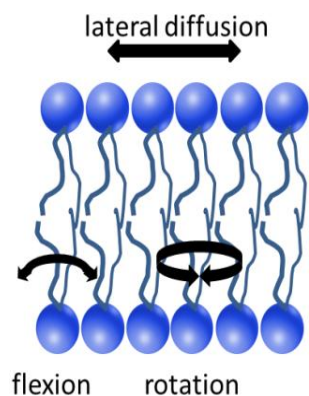


**Figure 3.7** Amphiphilic molecules inside lipid bilayer and the types of movement they exhibit.

Here it should be mentioned that the constant movement of lipids inside natural bilayers is one of the reason for the lack of long term stability. This movement of molecules is significantly reduced inside polymeric bilayers. The exchange of polymer chains between aggregates, which can be considered as kinetically trapped, is very long compared to the experimental time scales ( $t \gg 10^3$ ).

### 3.2.1 Mechanical Properties of the Cell Membrane

Mechanical features of the membrane are typically characterized in terms of three mechanical moduli: the area compression modulus  $K_a$ , the bending modulus  $\kappa_b$ , and the edge energy  $\mathcal{A}$ .

The compression modulus  $K_a$  of a bilayer differs from that of a sheet of an isotropic material which is given by:<sup>20</sup>

$$K_a = \frac{d_p K_v}{\frac{4}{9} + \frac{K_v}{3\mu}} \quad \text{Equation 3.8}$$

where  $K_v$  and  $\mu$  are the volume compression and shear moduli respectively and they are independent on the object shape. For this reason  $K_a$  should increase linearly with the thickness of the bilayer.

Unlike isotropic materials, molecules inside amphiphilic bilayers rearrange easily and thus, the resistance to expansion in a bilayer is a result of the extra hydrophobic area exposed to water upon pulling the lipids apart. This behavior results from different  $K_a$  value:

$$K_a = 2\gamma \quad \text{for the monolayer} \quad \text{Equation 3.9}$$

$$K_a = 4\gamma \quad \text{for the bilayer} \quad \text{Equation 3.10}$$

where  $\gamma$  is the surface tension of the water/amphiphile interface and as it was shown experimentally  $\gamma$  is in the range of 0.02-0.05 J/m<sup>2</sup>. From *Equation 3.10*,  $K_a$  of a lipid bilayer should be in the range of 0.08-0.2 Jm<sup>-2</sup> and should be independent of the bilayer thickness.<sup>20</sup>

The bending of a bilayer defined as the energy required in order to deform a membrane is an interplay of both stretching and compression. During bilayer bending one layer is stretched while the second one is being compressed at the same time, as shown in *Figure 3.8*.

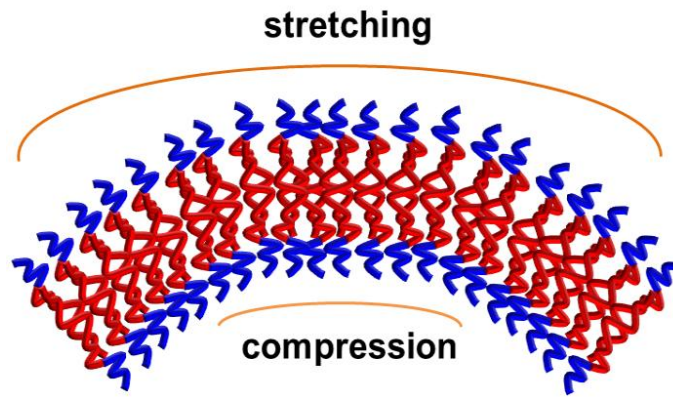


**Figure 3.8** Schematic representation of the membrane bending mechanism.

The energy required to bend a bilayer increases strongly with the curvature. The energy density  $F$  consists of the squared mean curvature and the Gaussian curvature and can be written as:<sup>20</sup>

$$F = \left(\frac{\kappa_B}{2}\right) * \left(\frac{1}{R_1} + \frac{1}{R_2}\right)^2 + \frac{\kappa_G}{R_1 R_2} \quad \text{Equation 3.11}$$

where  $\kappa_G$  is the Gaussian bending rigidity.

The bending modulus  $\kappa_b$ , compression modulus  $K_a$  and the membrane thickness  $d$  are related to each other by:

$$\kappa_b = K_a * d \quad \text{Equation 3.12}$$

Both the area compression modulus  $K_a$  and the bending rigidity  $\kappa_B$  have been measured for several lipid bilayers using a number of different techniques.<sup>29-31</sup> The area compression modulus  $K_a$  is extracted while the membrane strain is recorded as a function of the applied stress. Here the micropipette aspiration method<sup>32, 33</sup> is commonly applied. The stress induced change in the membrane area is usually extracted from microscopic images, and  $K_a$  is calculated from a fit to the stress-strain curve.<sup>29, 34</sup> In another approach the stress on the bilayer is induced by osmotic

pressure, what causes a decrease of the interface area per lipid.<sup>35</sup> X-ray scattering is also utilized and in combination with the ordering of hydrocarbon chains it determines the average interface area per lipid.<sup>30</sup> The information about the bending rigidity of a membrane is gained by analysis of the bilayer's thermal undulations as proposed by Brochard and Lennon.<sup>31</sup> Selected values of area compression moduli and bending rigidities of lipid bilayers and cell membranes are presented in *Table 3.1*.

**Table 3.1** Area compression moduli  $K_A$  and bending rigidities  $\kappa_B$  of lipid bilayers and cell membranes.<sup>20</sup>

Membrane	Apparent $K_A / \text{Jm}^{-2}$	$\kappa_B (\times 10^{-19} \text{J})$	Reference
diAPC	0.135+/- 0.020	0.44+/- 0.05	34
diMPC	0.145+/- 0.010	0.56+/- 0.06	34
SOPC	0.22	0.90+/- 0.06	30, 34
EggPC	0.14-0.17	0.8	36-38
Red Cell Plasma	0.45	1.3	39-41

As can be seen in *Table 3.1*, the compression modulus of a plasma membrane is significantly higher than in case of pure lipid membrane. This is due to the heterogeneous nature of plasma membrane, which contains not only lipids but also membrane-embedded proteins and cholesterol. It was shown that the presence of cholesterol increases the membrane's resistance to both compression and bending.<sup>20, 42</sup>

### 3.3 Cell Membrane Models

Cell membranes are very complex systems composed of lipids, proteins, and additional biomolecules which are constantly interacting with each other to coordinate all the essential processes of living organisms. Although many separate components of the membrane were identified and characterized<sup>43-45</sup> the understanding of how these components interact with each other in detail to drive the complex processes and multifarious functions of cell membranes is still elusive.

The high complexity of natural membranes and the diverse coupling of interactions within these bilayer structures have inspired the development of manifold simplified model systems, as illustrated in *Figure 3.9*. Artificial model membranes can serve as a platform to investigate physical parameters of the process in absence of any biofunctional molecules and/or supplementary energy. Utilizing of artificial model membranes facilitates decoupling of mutual interactions inside natural membranes and focusing on physical aspects while biochemical processes are missing. A wide variety of approaches including free standing<sup>46-48</sup> and tethered vesicles<sup>46, 49</sup> as well as solid-supported and planar bilayers<sup>50-52</sup> provide various experimental platforms to study systematically the physical and chemical characteristics of individual membrane components, their interplay, different aspects of structure-property relations as well as the role of interactions with the environment.<sup>16, 23, 53, 54</sup> However, functional aspects, e.g. the transmembrane transport are barely accessible to these model systems.

Depending on the application numerous different model systems were developed and systematically studied. A few important model systems of a cell membrane<sup>46</sup> can be seen in *Figure 3.9* and three of the most important concepts are briefly described below.

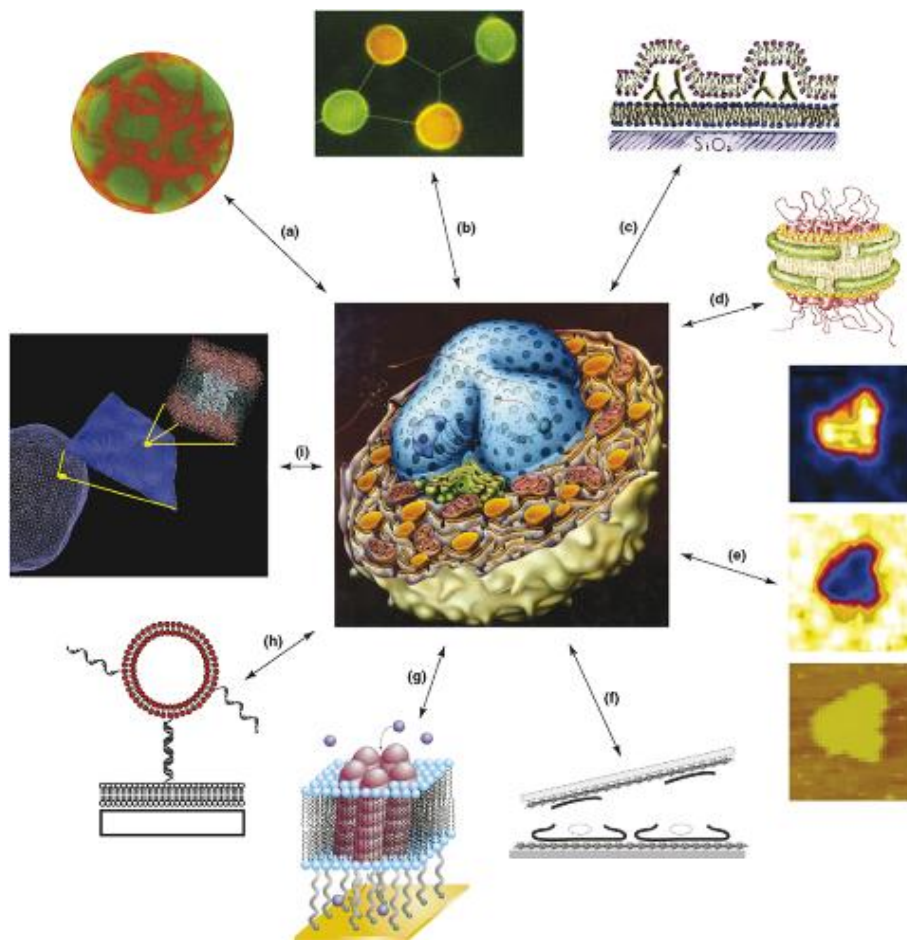


**Figure 3.9** Model membrane systems. In clockwise order, beginning from the upper left: **a.** Giant unilamellar vesicles and blebs;<sup>55</sup> **b.** networks of giant vesicles connected by lipid microtubules;<sup>56</sup> **c.** ruptured GUV's on solid supported bilayers;<sup>57</sup> **d.** membrane nanodiscs containing transmembrane proteins;<sup>58</sup> **e.** supported lipid bilayers analyzed by NanoSIMS;<sup>59</sup> **f.** ruptured cell membranes on solid supports;<sup>60</sup> **g.** bilayers tethered to a solid support containing ion channels;<sup>61</sup> **h.** vesicles tethered to a supported lipid bilayer by DNA;<sup>62</sup> **i.** visual representation of multi-scale simulations.<sup>63</sup> (*used with permission of Elsevier*).

### 3.3.1 Black Lipid Bilayers (BLM)

Black lipid membranes, which took the name from their appearance under optical microscope, were the first attempt to mimic cell membranes of a molecular-scale thickness and to study basic membrane functions.<sup>64</sup>

Several methods of preparation are known but two of them, based on painting of the lipid solution over the aperture and the formation of folded bilayer, are most common.<sup>65, 66</sup> The resulting bilayer is suspended over the aperture with an aqueous compartment on each side (see *Figure 3.10*). In this sense black lipid membranes have the advantage over supported membranes (see 3.3.3) as they do not have any contact with the underlying substrate and the aqueous phase access both sides of the membrane.<sup>67</sup> This encourages the application of this model system to perform conductance measurements to monitor transport process across membranes.

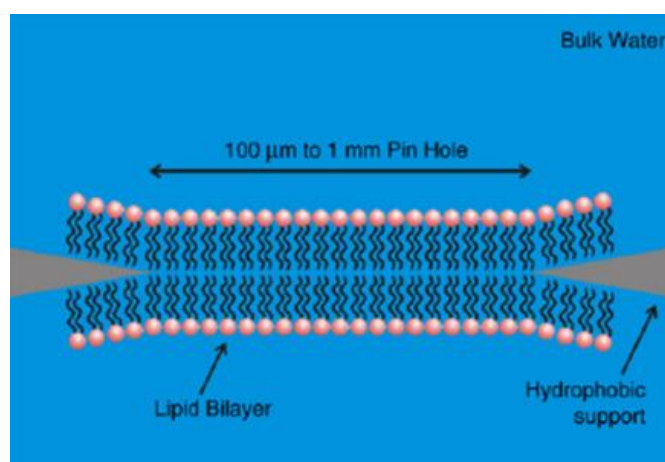


**Figure 3.10** Schematic representation of freely moving black lipid membrane in aqueous solution. (*Used with permission of Elsevier*)

The main limiting factor is the poor stability of black lipid membranes which also limits the application of powerful membrane characterization methods (e. g. AFM, SPR). One interesting attempt to increase the black lipid membrane stability was the replacement of lipids with block copolymer molecules.<sup>68</sup> These molecules behave analogous to lipids and form a 10 nm thick bilayer with improved mechanical properties. The most important methods of the black lipid membrane characterization are still optical microscopy and electrical conduction; a few more

sophisticated optical techniques were however employed lately to access black lipid membranes.<sup>66, 67</sup>

Modest stability, plane shape and poor resolution of the characterization methods accessible for this model make them insufficient to simulate transmembrane the transport of nanoparticles. Nanoparticle uptake processes and their interactions with membranes are curvature mediated, but due to its nature, planar bilayer cannot promote such interactions. Despite this fact black lipid membranes can be expected to possess great potential for the applications like: diagnostics, sensors, and even drug delivery.<sup>69</sup>

### 3.3.2 Vesicles (Liposomes, Polymersomes)

Both amphiphilic lipids and amphiphilic block copolymers are able to self-assemble in water into vesicles - bilayers (see 3.1) which enclose a portion of the aqueous phase in their interior, as shown in *Figure 3.11*.<sup>16, 70</sup> Thus, such structures are confined compartments. This fundamental architectural as well as the given structural similarity between vesicles and cell membranes make vesicles perfect candidates to study the physical and physico-chemically properties of assembled bilayers.<sup>71-75</sup>

Vesicles are surrounded by the aqueous media in which they are moving freely. The amphiphilic membrane retains its fluidity and the natural environment is kept on the both sides of the membrane. Vesicles can be prepared in different dimensions, in large quantities and using relatively simple methods. This makes them suitable for a variety of bulk measurements like spectroscopic measurements or microscopy.<sup>72, 73, 76-80</sup> Unspecialized simple vesicles are commonly utilized as a model of a membrane. Requirements for this purpose are a long-term stability, and a subtle balance between rigidity and elasticity of the model membrane.<sup>81</sup> Phospholipids, the natural constitutive units of membranes, which form spontaneously

liposomes<sup>82, 83</sup> when certain lipids are dispersed in aqueous medium, are mostly used as building blocks of the majority of membrane models established.<sup>46-52, 84</sup>

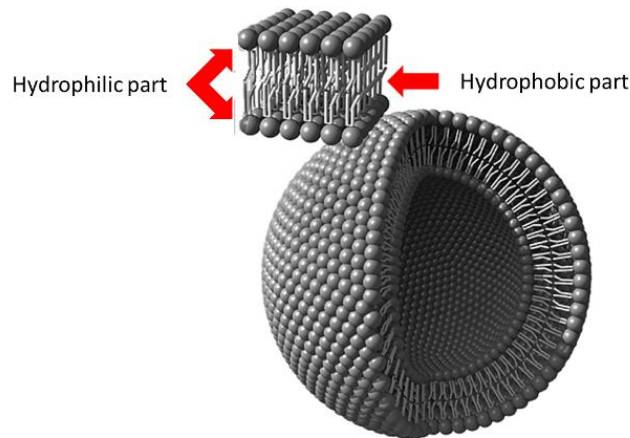


**Figure 3.11** Schematic representation of a vesicle formed from amphiphilic molecules (lipids or block copolymers) and the cross section of the shell forming membrane. Hydrophilic “heads” are pointed out to the aqueous medium while hydrophobic “tails” are pointed in to the membrane core.\*\*

The simple transmembrane model system based on liposomes and SiO<sub>2</sub> nanoparticles was recently developed.<sup>71</sup> It was proven that nanoparticles can cross the liposome membrane by an “endocytosis-like” process, however, the complex characterization and evaluation of the process was missing. The major drawback of this model has its source directly in the properties of the liposomes. Lipid membranes have poor long-term stability and the limited chemical stability caused by oxidation processes of unsaturated fatty acids and the hydrolysis of ester bonds.<sup>81</sup> One promising alternative are amphiphilic block copolymers, which are structural analogs of lipids and also self-assemble into vesicles (polymersomes) under certain conditions.<sup>16</sup>

\*\* <http://journalofcosmology.com/Abiogenesis110.html>

Both polymersome and liposome properties are strongly influenced by the characteristics of amphiphilic molecules.<sup>85-87</sup> In contrast to liposomes where lipid properties manipulation is limited, the thickness, bending and stretching moduli, and the permeability of the polymeric membrane can be easily tuned by changing the block copolymer molecular characteristics. The polymer molecular mass, the polydispersity and the structure of the building blocks are the key parameters responsible for the polymeric bilayer performance.<sup>85, 86, 88</sup> A library of amphiphilic molecules which are able to self-assemble into vesicular structures<sup>89, 90</sup> has expanded due to the progress in living polymerization methods opening new ways to polymersomes features manipulation. This flexibility makes polymersomes perfect candidates to serve as a model membrane. Unlike other model systems, in case of vesicles the membrane curvature is preserved, allowing study of curvature dependent interactions.

### 3.3.3 Supported Bilayers

Unlike a vesicle or a cell membrane in which the lipid bilayer is rolled into an enclosed shell, a supported bilayer<sup>50, 91</sup> is a planar structure sitting on a solid support (see *Figure 3.12*). The solid support improves membrane robustness and stability and a thin (10-20 Å) layer of trapped water between the substrate and the bilayer maintains the membrane fluidity. The phospholipid bilayers remains attached to the solid support due to the combination of van der Waals, electrostatic, hydration and steric forces.<sup>92</sup>

Supported membranes can be prepared by a few methods in combination, with the of Langmuir-Blodgett technique and the Langmuir-Schaefer procedure being one of the most important one.<sup>91</sup> Another common and well spread method is the formation of a supported bilayer in a result of adsorption and fusion of vesicles from aqueous solution.<sup>93, 94</sup>

The presence of a solid support make the bilayers accessible to characterization with surface specific techniques like atomic force microscopy, surface plasmon resonance, or quartz crystal microbalance. Unfortunately supported membranes are not completely decoupled from the substrate; coupling between the bilayer and the solid substrate leads to a remarkable slowing of the lateral diffusion, which is accompanied by a break-down of the 2D fluid nature of the membrane.<sup>95, 96</sup> This has also significant influence on the embedded membrane-spanning proteins, which, due to their interactions with the substrate, usually show no 2D mobility.<sup>94, 97</sup>

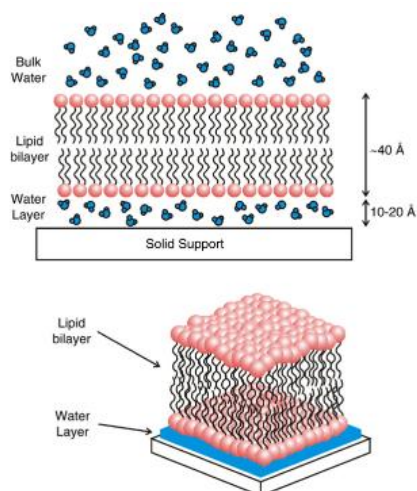


**Figure 3.12** Schematic diagram of a solid supported phospholipid bilayer. The membrane is separated from the substrate by a 10–20Å thick layer of water.<sup>67</sup> (Used with permission of Elsevier)

### 3.3.4 Polymer Cushioned (Tethered) Bilayers

Further improvement of the mechanical stability assisted by the prevention of protein-substrate unfavorable interactions was achieved by the development of polymer cushioned bilayers schematically shown in *Figure 3.13*. Polymer cushioned bilayers increase the thickness of the aqueous lubricant layer between the bilayer and the substrate by introducing a hydrophilic

polymer cushion. A polymer cushion acts as a spacer and minimizes the surface influence on the supported bilayer and still allows for investigation by an array of surface science techniques (e. g. SPR).

The polymer support needs to be soft, hydrophilic, not too highly charged, and not extensively cross-linked.<sup>50</sup> For this reason mainly polymers like dextran, cellulose, chitosan, polyelectrolytes and lypopolymer tethers were investigated.<sup>98-101</sup>

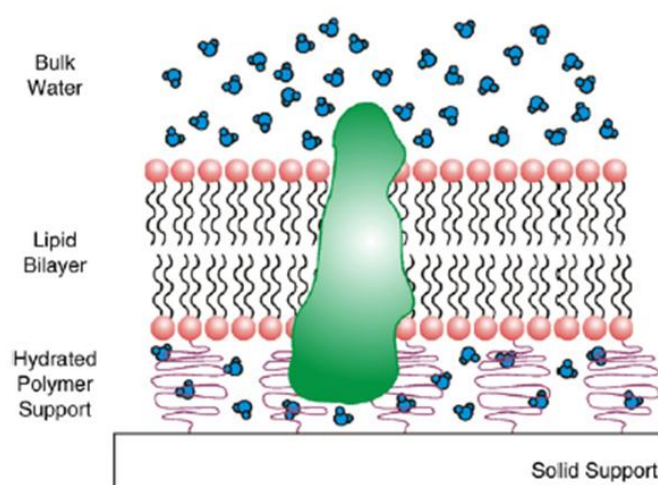


**Figure 3.13** Schematic representation of lipid proteins with embedded proteins “sitting” on the polymeric cushion.<sup>67</sup> (Used with permission of Elsevier)

Cushioned bilayers have the advantages of both black lipid membranes and supported membranes. Their stability is significantly improved in comparison to BLMs and at the same time the environment at each side of the membrane is “protein friendly”. The polymer cushion prevents unwanted interactions between the protein and the surface inhibiting protein denaturation and immobilization. This model is especially useful to probe membrane interactions with the membrane, their arrangements and interactions with external environment.

### 3.4 Transmembrane Transport

Cellular transmembrane transport is an effect of coordinated mechanisms that regulate the passage of a variety of substances through a semi-permeable membrane over a broad range, from Ångstroms to microns. Therefore it is obvious that several mechanisms have to be involved including three main processes: **1.** Fickian diffusion, **2.** facilitated diffusion and **3.** active transport, as illustrated in *Figure 3.14*. Hydrophilic substances in order to avoid contact with the lipid bilayer pass through the membrane using transport proteins. Some of them, called channel proteins, act as a hydrophilic tunnel through the membrane, some others, called carrier proteins, change their shape to shuttle molecules from one side of the membrane to the other side.<sup>102</sup>

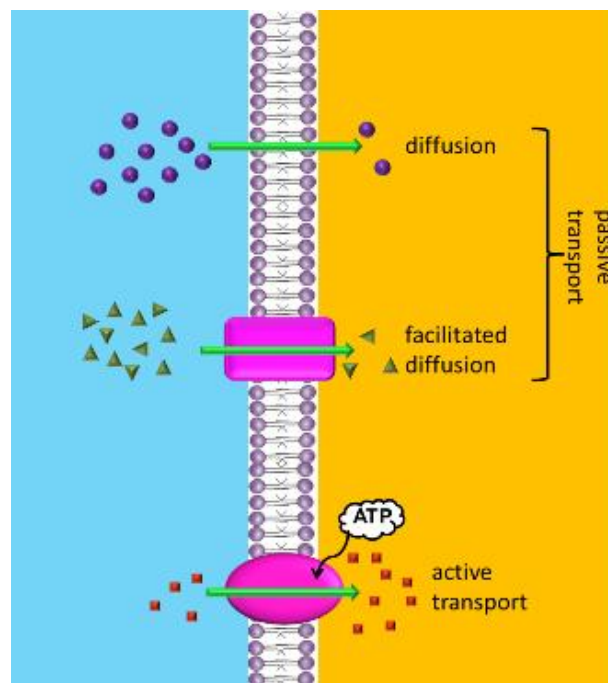


**Figure 3.14** Schematic illustration showing the difference between passive and active transmembrane transport.

Thermodynamically the flow of substances from one compartment to another occurs in the direction of a concentration or electrochemical gradient. If the exchange of substances occurs in

the direction of the gradients, there is no need of additional energy input and therefore such processes are called passive transport. If, however, the transport is against a gradient, it will require the input of energy (ATP = adenosine triphosphate) and hence the process is named active transport. *Figure 3.15* displays diverse ways of transmembrane transport (**a**) and different nanoparticles internalized by living cells (**b-d**).

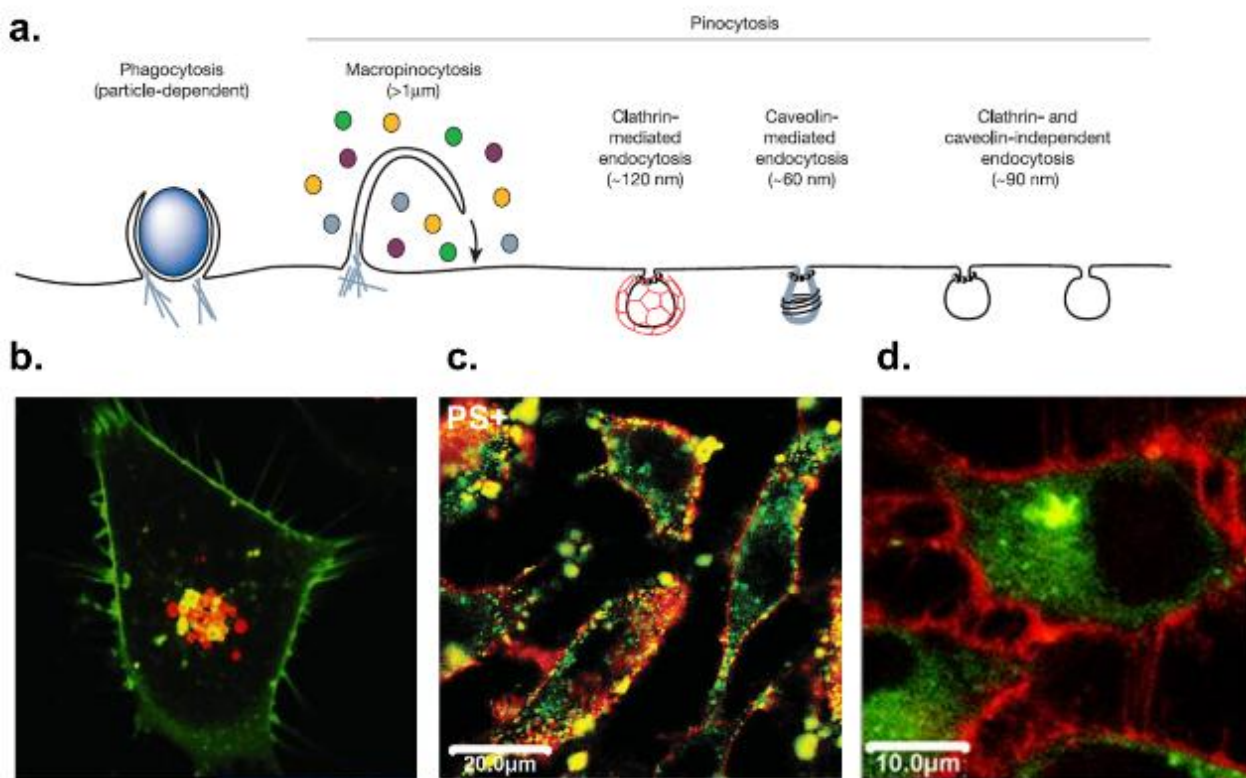


**Figure 3.15 a.** Multiple portals of entry into the mammalian cell. The endocytic pathways differ with regard to the size of the endocytic vesicle, the nature of the cargo (ligands, receptors and lipids) and the mechanism of vesicle formation (*adapted with permission of Nature Publishing Group from*<sup>103</sup>) **b.** drug release within a treated cancer cell<sup>104††</sup> **c.** Polystyrene nanoparticles incorporated inside HeLa cells; (*Adapted with permission of John Wiley and Sons from*<sup>105</sup>) **d.** Polylactide nanoparticles incorporated by HeLa cells. (*Adapted with permission of American Chemical Society from*<sup>106</sup>)

†† <http://www.purdue.edu/uns/html4ever/2006/060908.Low.reduc.html>

### 3.4.1 Passive Diffusion

Passive diffusion is a spontaneous movement of substances down to their concentration gradient (from more to less concentrated places). The diffusion of substances across biological membranes is referred as passive, because to run the process no input of additional energy is needed. The concentration gradient is itself the driving force for this process and membrane embedded proteins are usually not involved in this process. The phenomenon of diffusion process assisted by membrane proteins is known as facilitated diffusion.<sup>102</sup> Facilitated diffusion can be still considered as passive diffusion in the sense that it does not require any additional energy, it does, however, require assistance of membrane proteins. The passive transport of ions and small molecules across membranes is always coupled with the growth of entropy of the system. Therefore, passive transport is dependent on the permeability of the cell membrane, which is dependent on the organization and characteristics of the membrane lipids and proteins (*vide supra*).

### 3.4.2 Primary and Secondary Active Transport

Generally, the active transport of substances across cell membranes is a translocation against the concentration gradient (from less concentrated places to high concentration). Thus, to perform the movement against the concentration gradient, input of additional energy from outside is requested (usually the energy is provided by adenosine-5'-triphosphate molecules = ATP). The approach on how this energy is used lead to the division of active transport to primary and secondary active transport. Primary active transport uses the energy directly, to move molecules across the membrane, while secondary active transport does not involve direct consumption of metabolic energy (ATP). During the secondary active transport the hydrolysis of the energy provider (ATP) is used indirectly. Hydrolysis causes a gradient of the solute transported along with the target compound and this electrochemical gradient is a driving force for molecules

transport. The protein specialized in hydrolysis of ATP in order to generate an electrochemical gradient to confer certain membrane potential characteristics is usually referred as pump, with sodium-potassium pump being one of the most spread one.<sup>102, 107</sup>

### 3.4.3 Bulk Transport - Endocytosis

As described above, both water and other small molecules can enter and leave the cell by direct passing through the lipid bilayer (diffusion) or being pumped or carried by specialized membrane proteins. These mechanisms cannot be used, however, for the transportation of larger molecules or even particles. Cells have developed a separate mechanism, which let them transport, e. g., large proteins and polysaccharides. Colloidal nanoparticles are taken up by the cells using different endocytic mechanisms. The key-stages of this process involves the adsorption of a large object (molecule or particle) to the cell membrane, inducing a deformation of the bilayer followed by an invagination of the cell membrane, and subsequently wrapping and pinching off of the completely wrapped object into the cell interior. During this process, cells generate significant mechanical force, leading to membrane deformation. Subsequently, the membrane-coated particle is detached from the inner membrane (see *Figure 3.16*).<sup>103</sup>

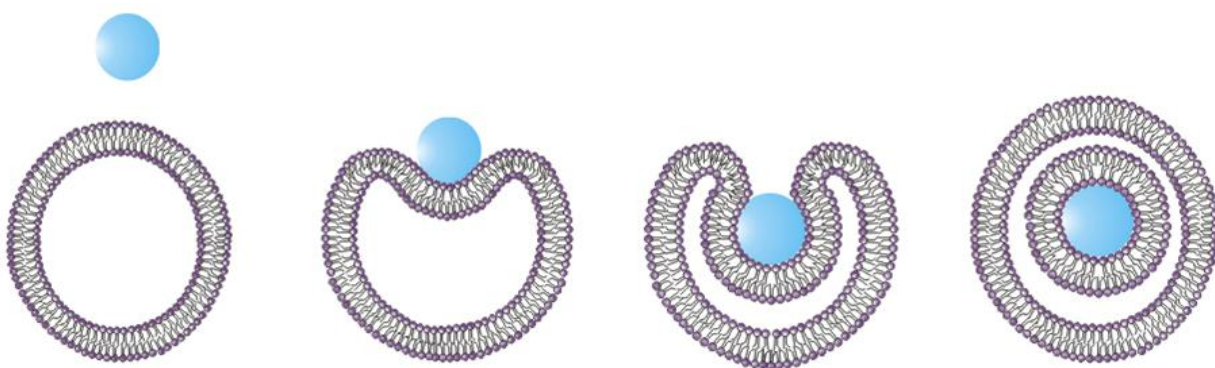


**Figure 3.16** Schematic illustration of nanoparticle internalization into polymersome. The nanoparticles are first absorbed, then wrapped by the polymeric membrane and finally completely incorporated.

As illustrated in *Figure 3.17*, endocytosis pathways could be subdivided into three categories: namely, macropinocytosis, phagocytosis and receptor-mediated endocytosis involving clathrin and caveolae mediated endocytosis).

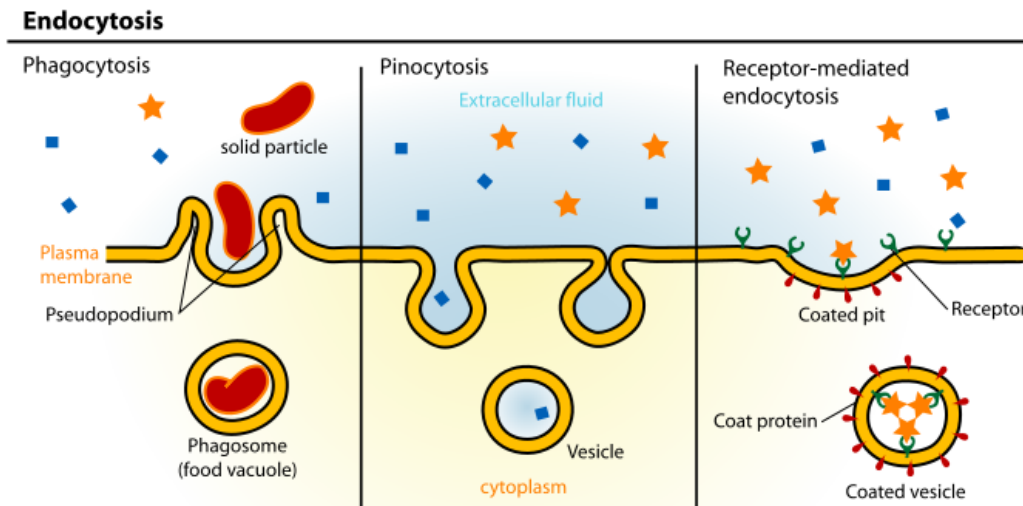


**Figure 3.17** Different types of endocytosis occurring in living cells (see text).<sup>††</sup>

### 2.4.2.1 Pinocytosis

Pinocytosis is a form of endocytosis used primarily for the absorption of extracellular fluids into very small vesicles. The cell does not need the fluid but the molecules which are dissolved in it. Unlike receptor-mediated endocytosis, pinocytosis is nonspecific in the substances that it transports, as the cell takes fluids including all solutes present.<sup>102</sup>

### 2.4.2.2 Phagocytosis

In contrast to pinocytosis, during phagocytosis the cell engulfs single particles which are not broken-down. The particle is digested after the endosome containing the particle of interest fuses with a lysosome (containing hydrolytic enzymes) inside the cell.<sup>102</sup>

<sup>††††</sup> Source of the picture: WIKIPEDIA

### 2.4.2.3 Receptor-Mediated Endocytosis (RME)

Receptor-mediated endocytosis involves membrane proteins with receptor sites specific to the molecules being internalized. Extracellular substances of interest (ligands) bind to the receptors and at the same time a coated pit forms a vesicle containing these ligands. Receptor-mediated endocytosis is widely used for the specific uptake of certain substances required by the cell: hormones, antibodies, serum transport proteins but also viruses and toxins. Receptor-mediated endocytosis can occur by at least two different pathways: clathrin-mediated and caveolae – mediated, although recently more clathrin-independent pathways were reported.<sup>108</sup>

- **Clathrin-mediated endocytosis** occurs in all cells and is mediated by small vesicles that have a morphologically characteristic crystalline coat made up of a complex of proteins that are mainly associated with the cytosolic protein clathrin.<sup>109</sup> The formation of endocytic clathrin-coated vesicles takes place through the interactions of cytosolic proteins with components of the inner leaflet of the membrane. It consists of three stages: (I) assembly of clathrin into a polygonal lattice and formation of coated pits, (II) invagination of coated pits, and (III) pinching-off of the coated vesicles.<sup>110</sup>
- **Caveolae -mediated endocytosis** is the most common reported non-clathrin-dependent pathway, which can be found in many, but not all cell types. A protein called caveolin is responsible for the formation and maintenance of caveolae, causing also the local changes in morphology of the membrane. Caveolae are capable of importing molecules and delivering them to specific locations within the cell, exporting molecules to extracellular space, and compartmentalizing a variety of signaling activities. The underlying mechanism of invagination, budding, and vesicle trafficking differs significantly from the coated pit pathway.<sup>111, 112</sup>

### 3.5 Theoretical Model of Transmembrane Transport

Due to the difficulties to achieve proper information out of experimental model systems as described above (see 3.3) one alternative is the use of computer simulations. Numerous studies focusing on the development of appropriate theoretical models describing nanoparticle interactions with membranes and transmembrane transport of such objects are published every year.

The simplest theoretical models are based on the interactions of unilamellar vesicles with colloidal particles.<sup>113, 114</sup> The internalization process in this case is driven by adhesion and mechanical properties of the bilayer, *i.e.* fluidity and elastic moduli. The uptake of nanoparticles was reported to be strictly size and shape dependent<sup>115-117</sup> and moreover, the curvature of the bilayer strongly influences the internalization process. On the theoretical side a balance between fluidity of the artificial membrane and short-ranged adhesive potential, given by a crucial size ratio is necessary for a successful incorporation process as illustrated in *Figure 3.18*. The existence of a threshold particle size,<sup>118</sup> below which single nanoparticle could not be internalized by a flexible membrane, has been proposed<sup>113, 114, 119, 120</sup> and observed in cellular systems.<sup>115-117, 121-123</sup> Nanoparticles below a certain size are simply not able to reduce the curvature energy of the membrane which is necessary for the nanoparticle engulfment.

The selection of proper parameters and model compartments is crucial in order to deliver meaningful information about the mechanism of the process. This section is focused only on the models developed based on mechanical properties of the bilayer and the adhesive interaction between the bilayer and particles, where the presence of additional biological molecules, proteins and/or additional energy is neglected.

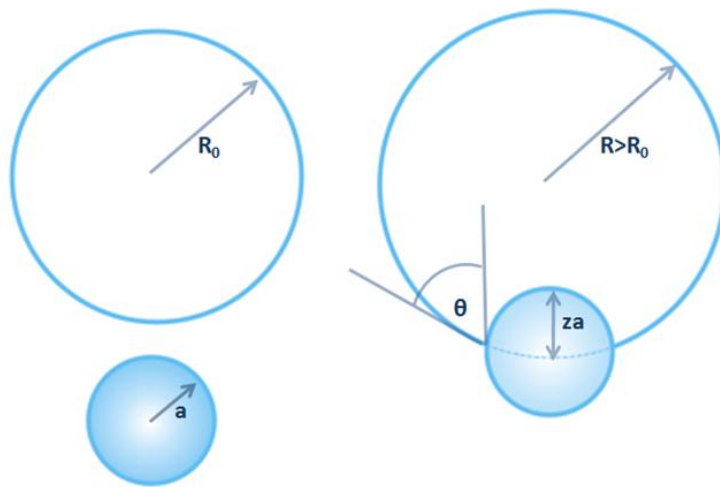


**Figure 3.18** Schematic view of a colloid adhering to a spherical vesicle. In the complexed state, the contact area gives rise to a binding energy, while the resulting expansion of the vesicle requires work to be done against the membrane tension. The degree of penetration  $z$  and the contact angle  $\theta_a$  are indicated as well.<sup>113</sup>

The simplest theoretical model proposed by Deserno and co-workers<sup>113, 114</sup> was based on mutual interactions between an unilamellar vesicle and a small colloidal particle. Here, physical properties like adhesion between the vesicle and the colloidal particle, stretching and bending energy of the membrane were considered. Adhesion energy between a particle and the membrane is believed to be a driving force for wrapping and can run the process without any additional energy involved (proteins, biomolecules *etc.*). The set of conditions for which the particle is unbound, partially wrapped and fully enveloped were established (see *Figure 3.19*). Despite the adhesion interactions, the size of both, vesicle and colloidal particle, is believed to be a factor determining the endocytosis process. If the vesicle is large enough, decreasing size of the colloidal particle leads first to progressively more wrapping, then jump to fully enveloped state, and finally to an unbinding of the complex. Curvature energy is crucial while considering the interaction of vesicles with very small particles ( $a \sim s$ ;  $s$  is a length scale equal to  $\sqrt{K_B/k_{ad}}$ ).

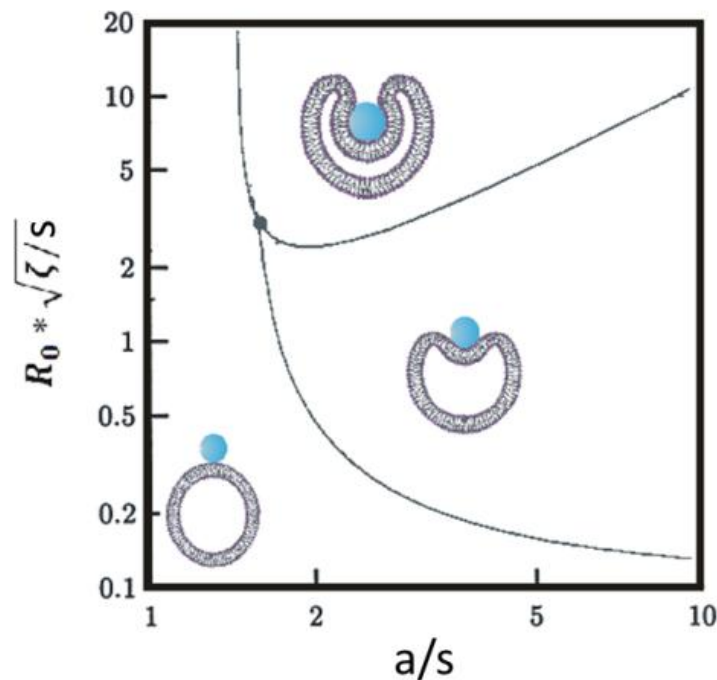


**Figure 3.19** Phase diagram of colloid-vesicle complexes in the  $(a; R_0)$  plane. The regions separated by lines correspond to unbound, partially wrapped, and enveloped states, respectively, as also indicated qualitatively by the pictures.<sup>113</sup>;

Similar observations regarding the threshold nanoparticle size were delivered by a theoretical model designed in the group of Balazs.<sup>119</sup> Here, the interactions of a lipid bilayer membrane with a nearly spherical particle with hydrophilic surface were considered with the aim of controlling the passage of particles into and out of vesicles. It was established that for a homogeneous membrane with a uniform attraction to the particle it is impossible to fully wrap this particle below a certain value of the adhesion strength. Both, a uniformly adhesive, homogeneous membrane and a nonadhesive membrane containing an adhesive raft, were considered. For the homogeneous membrane, it was established that the particle always remains attached to the vesicle membrane, even when the particle is completely wrapped; it still remains trapped at the membrane. Considering a heterogeneous membrane, it was found that if particle is in contact with an adhesive raft of comparable size, it is possible for the particle to pass across the

membrane. In this situation, when the particle is nearly fully wrapped, the raft's interfacial energy drives a fission process at the membrane neck, thus freeing the wrapped particle from the flat membrane.

In another approach Fosnarić and coworkers<sup>124</sup> performed Monte Carlo simulations on charged fluid like vesicles and oppositely charged spherical colloidal particles. Here the vesicle-colloid interactions were imposed by the migration of charges on the vesicle surface and elastic deformations of the vesicle. Wrapping process is considered as a function of the number of charges on the vesicle. This system typically exhibited a discontinuous wrapping transition from a partial to complete (or almost complete) degree of wrapping. The two energetically preferred states, partially and completely wrapped, can be separated by an energy barrier significantly larger than the thermal energy  $k_B T$ . Decreasing the bending stiffness of the vesicle weakens the wrapping transition until a critical point is reached beyond which the wrapping becomes a continuous process. When the spontaneous curvature of the charged vertices was opposite to the curvature of the colloid, the wrapping was also a continuous process.

The adhesion of nanoparticles to vesicles was studied also by Noguchi and Takasu.<sup>125</sup> They have used Brownian dynamics simulation to study interaction of vesicles with adhesive nanoparticles. The interaction between a spherical nanoparticle with the hydrophilic segments of amphiphilic molecules were considered to investigate the budding and fission of a vesicle. This process is believed to be caused by the adhesion of the nanoparticle. It was shown that the nanoparticle induces the structural changes of the vesicle: budding, stalk formation and fission. The stalk state represents a fission being intermediate between budded and separated states. The budded vesicle changes to the stalk state through pore opening at the connection region. It was also shown that the nanoparticle promotes the fusion process from the stalk intermediate to the fusion-pore opening.

Mechanisms of nanoparticle uptake by cells were very recently addressed by dissipative particle dynamics (DPD) simulation.<sup>120</sup> It has shown that the mechanism of nanoparticle incorporation depends on the size, membrane tension, and nanoparticle concentration. Small neighboring particles might cluster prior to internalization in order to reduce curvature energy of the membrane. An increase of the nanoparticle size would weaken the curvature mediated interactions since large nanoparticle sizes reduce the perturbation of the membrane curvature. Thus the delicate balance of interactions renders different assemblies for small and large nanoparticles.

Here only a few key theoretical models were described giving the reader insight into approaches used and parameters being considered. This field is still developing and delivering new insight into nanoparticles uptake mechanisms. It is also stimulating for experimentalist providing the directions how to design their experiments in order to probe specific mechanisms.

## 3.6 Characterization Methods

### 3.6.1 Photon Correlation Spectroscopy (PCS)

#### 3.6.1.1 Basic Principles of Photon Correlation Spectroscopy

Photon correlation spectroscopy (PCS)<sup>126-128</sup> including static (SLS) as well dynamic (DLS) experiments, has become a powerful non-invasive technique for characterizing the properties of suspensions and solutions of macromolecules, colloids, and particles. When light impinges on matter, the electric field of the light induces an oscillating dipole in the molecules. Hence the molecules provide a secondary source of light and subsequently scatter light. The frequency shifts, the angular distribution, the polarization, and the intensity of the scatter light are determined by the size, shape, and molecular interactions in the scattering material.

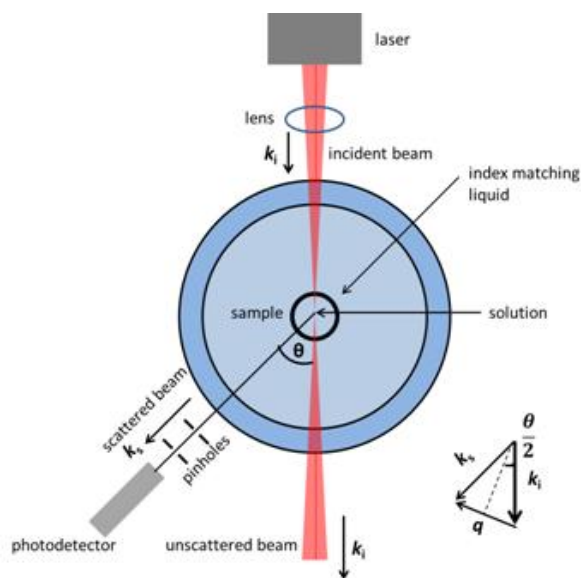


**Figure 3.20** Schematic illustration of a typical light scattering setup. A polarized laser beam impinges in the tube that contains the sample, and is scattered at all directions. A photodetector collects the scattered light at a desired scattering angle  $\theta$ . The inset shows the scattering wave vector  $q$ , which is defined as the difference between the scattered and the incident beam,  $k_s$  and  $k_i$ , respectively. (Drawn based on Teraoka, I., *Polymer solutions. An Introduction to Physical properties*. Wiley Online Library: 2002)

In order to probe the uptake of nanoparticles by polymersomes, which influence the static as well the dynamic behavior of the system due to kinetic processes SLS and DLS experiments, were performed.

A schematic representation of a typical light scattering setup<sup>126</sup> is shown in *Figure 3.20*. In such an experiment, a laser beam impinges the sample placed in a transparent liquid matching bath and this incident light is scattered at scattering objects into all directions (Rayleigh scattering). A photodetector, placed on a goniometer arm which can move around the sample to reach different scattering angle  $\theta$ , collects the photons of the scattered light. Polarizers and analyzers are used to define the polarizations of the incident and scattered light beams, respectively.

For a given incident beam of a wavelength  $\lambda$  and at a scattering angle  $\theta$ , the scattered time average intensity  $I(q)$  is related to the spatial density distribution of the scatters through the following relationship:

$$I(q) = \int \vec{\rho}(-\vec{r}') \vec{\rho}(\vec{r}') \exp(i\vec{q} \cdot \vec{r}) d^3\vec{r} d^3\vec{r}' \quad \text{Equation 3.13}$$

where:

$$q = \frac{4\pi n}{\lambda} \sin\left(\frac{\theta}{2}\right) \quad \text{Equation 3.14}$$

is the scattering wave vector,  $n$  the refractive index of the medium, and  $\vec{\rho}(\vec{r})$  describes the distribution of the scattering density. Virtually  $\vec{\rho}(\vec{r})$  is the property of matter that interacts with the incoming electromagnetic waves of the incident laser beam. The scattered intensity consequently probes how a density fluctuation  $\delta\rho(q)$  spontaneously arises and decays due to thermal motions of the molecules. In light scattering,  $\vec{\rho}(\vec{r})$  is the distribution function of the refractive index (or the local polarizability) being proportional to the spatial density or

concentration fluctuations .<sup>128</sup> Since the latter fluctuates also in time, the measured quantity is  $I(\vec{q}, t)$ , which relates to dynamic properties of the system probed at the selected length scale of  $2\pi/q$ .

### 3.6.1.1.1 Dynamic Light Scattering (DLS)

Due to the Brownian motion of scattered objects in a solution or suspension, a time-dependent fluctuation in the scattering intensity is observable. The inherent correlation times are obtained from the measured intensity autocorrelation function  $G(q,t)$ , can be written as:

$$G(q, t) = \frac{\langle I(q, 0)I(q, t) \rangle}{\langle I(q) \rangle^2} \quad \text{Equation 3.15}$$

The polarized (VV) geometry (both incident and scattered light polarized normal to the scattering plane) provides information about the fluctuations of the concentration and/or the density of the material. The desired quantity which is related with the dynamic response of the system is the autocorrelation function of the scattered field  $C(q,t)$ . Under homodyne beating conditions the two autocorrelation functions are related via the Siegert's relation:

$$G(q, t) = A^*(1 + f^*|C(q, t)|^2) \quad \text{Equation 3.16}$$

where  $A^*$  ( $= \langle I(q) \rangle^2$ ) is the measured baseline and  $f^*$  is a spatial coherence factor that depends on the experimental setup, the scattered volume and the number of coherence areas viewed.

To analyze the computed relaxation functions  $C(q,t)$ , different algorithms can be used. In this work three different methods are used:

**The stretched exponential (Kohlrausch-Williams-Watts, KWW) method<sup>129</sup>** assumed that for single but nonexponential decay, the computed relaxation function  $C(q, t)$  can be represented by:

$$C(q, t) = \exp \left[ - \left( \frac{t}{\tau_{KWW}} \right)^{\beta_{KWW}} \right] \quad \text{Equation 3.17}$$

where  $\tau_{\text{KWW}}$  is the “average” relaxation time and  $\beta_{\text{KWW}}$  is the shape parameter ranging between  $0 \leq \beta_{\text{KWW}} \leq 1$  characterizing the distribution of relaxation times.

**The CONTIN method**<sup>130</sup> is based on the inverse Laplace transform of  $C(q,t)$  which then can be written as:<sup>131</sup>

$$C(q, t) = \int_0^{\infty} G(\Gamma) \exp(-\Gamma t) d\Gamma \quad \text{Equation 3.18}$$

where  $G(\Gamma)$  is the normalized decay constant distribution. The CONTIN method is more appropriate for a sample with a certain size distribution, which makes  $C(q,t)$  deviate from single exponential.

**The CUMULANT method**<sup>126, 132</sup> is used when the distribution is narrow and  $C(q,t)$  does not deviate much from a single exponential decay. In this method  $\ln(C(q,t))$  is approximated by a second order polynomial of  $t$ . The first two cumulants represent the mean  $\Gamma$  and its variance respectively:

$$\ln(C(q, t)) = -\langle\Gamma\rangle t + \frac{1}{2} \langle\Delta\Gamma^2\rangle t^2 - \frac{1}{6} \langle\Delta\Gamma^3\rangle t^3 \quad \text{Equation 3.19}$$

When there is no interactions between dissolved molecules,  $C(q,t)$  describes the decay of concentration fluctuations, due to mass diffusion:

$$C(q, t) = \exp(-\Gamma t) \quad \text{Equation 3.20}$$

where  $\Gamma$  is the so called relaxation rate and can be written as:

$$\Gamma = D_t q^2 \quad \text{Equation 3.21}$$

with  $D_t$  being the translational diffusion coefficient. The dynamic Zimm<sup>§§</sup> plot is often used to obtain the z-average  $D_t$  as  $q \rightarrow 0$  and  $c \rightarrow 0$ :

<sup>§§</sup> [http://www.uni-mainz.de/FB/Chemie/AK-Maskos/Dateien/PC\\_Makroskript\\_081017.pdf](http://www.uni-mainz.de/FB/Chemie/AK-Maskos/Dateien/PC_Makroskript_081017.pdf)

$$D_t = D_0(1 + C^* q^2 R_q^2 + \dots)x(1 + k_D c + \dots) \quad \text{Equation 3.22}$$

$C^*$  is a coefficient that describes the contribution of the shape fluctuations to the relaxation of the autocorrelation function  $G(q,t)$ .

As can be seen in *Equation 3.22*, the diffusion coefficient depends on the overall sample concentration  $c$  and this relation can be written as:

$$D_t = D_0(1 + k_D c + \dots) \quad \text{Equation 3.23}$$

with  $D_0$  being the diffusion at zero-concentration and  $k_D$  being linear coefficient represented by:

$$k_D = 2A_2M - \zeta_1 - v_{SP} \quad \text{Equation 3.24}$$

In a good solvent  $2A_2M > \zeta_1 - v_{SP}$  and  $D_t$  increases with concentration. In a poor solvent  $A_2$  decreases leading eventually to the negative values of  $k_D$ .

The diffusion coefficient  $D_t$  is related to the radius of diffusing objects by the Stokes-Einstein equation:

$$D_t = \frac{k_B T}{6\pi\eta R} \quad \text{Equation 3.25}$$

where  $k_B$  is a Boltzmann constant,  $T$  is temperature,  $\eta$  is the viscosity of the solvent, and  $R$  the z-average hydrodynamic radius of the particles.

### 3.6.1.1.2 Static Light Scattering (SLS)

The instantaneous scattering intensity  $I(\vec{q}, t)$  depends on the spatial arrangements of scattering centers (positions and conformations of molecules) at time  $t$ . As molecules move, changing their conformations and locations in space, the scattering intensity fluctuates in time.<sup>126</sup> The value of the scattering intensity averaged over a long time interval  $T^*$ , is the static scattering intensity  $I_{sc}(q)$ :

$$I_{sc}(q) = \langle I_{sc}(q, 0) \rangle = \lim_{t \rightarrow \infty} \frac{1}{T^*} \int_0^T I_{sc}(q, T^{**'}) dT^{**'} \quad \text{Equation 3.26}$$

The absolute scattering intensity for the polarized geometry  $R_{vv}$ , is given by:

$$R_{vv} = \frac{(I_{sol}(q) - I_{solv}(q))R_{tol}}{I_{tol}(q)} \quad \text{Equation 3.27}$$

where  $R_{tol}$  is the Rayleigh ratio for toluene,  $I_{sol}$  is the intensity of the solution and  $I_{solv}$  the intensity of the solvent. According to the Einstein fluctuation theory scattering can only occur if the object of interest has the refractive index different that the surrounding media.<sup>\*\*\*</sup> The polarizability  $\alpha$  in solution is a function of the density and of concentration fluctuations caused by the thermal movement of the molecules.

Then one can write:

$$\frac{K_o c}{R_{vv}} = \left( \frac{1}{M} + 2A_2 c + 3A_3 c^2 + \dots \right) \quad \text{Equation 3.28}$$

Where  $M$  is the mass of the dissolved material and  $K_o$  is the optical constant:

$$K_o = \frac{4\pi^2 n^2}{\lambda^4 N_A} \left( \frac{dn}{dc} \right)^2 \quad \text{Equation 3.29}$$

$A_2$  and  $A_3$  are the second and third virial coefficients, respectively, represented by:<sup>126</sup>

\*\*\* [http://www.uni-mainz.de/FB/Chemie/AK-Maskos/Dateien/PC\\_Makroskript\\_081017.pdf](http://www.uni-mainz.de/FB/Chemie/AK-Maskos/Dateien/PC_Makroskript_081017.pdf)

$$A_2 = \left(\frac{1}{2} - \chi\right) N_A v_{\text{site}} \left(\frac{N_s}{M}\right)^2 \quad \text{Equation 3.30}$$

$$A_3 = \frac{1}{3} (N_A v_{\text{site}})^2 \left(\frac{N_s}{M}\right)^3 \quad \text{Equation 3.31}$$

Here  $\chi$  is the Flory-Huggins parameter<sup>126</sup> and  $v_{\text{site}}$  is the volume per site and  $N_s$  the number of sites in the lattice theory. When  $A_2 = 0$ , the entropy of mixing compensates the repulsive polymer–solvent interactions or attractive polymer–polymer interactions and the solution is close to an ideal solution. Values lower than zero suggest poor quality of the solvent and higher than zero good solvents.

For particles larger than  $\lambda/20$ , interference of the scattered light is observed. Only at  $q=0$  the scattered intensity of large particles is not influenced by interference effects. In order to interpret the results in terms of Rayleigh theory the scattering intensity should be extrapolated to the zero angle. In this case the dependence of the scattered intensity on the scattering wave vector is expressed by the form factor  $P(q)$  which for small scattering vector  $q$  can be written as:

$$P(q) = 1 - \frac{q^2}{3! N_c^2} \sum_i^{N_c} \sum_j^{N_c} \langle r_{ij}^2 \rangle \quad \text{Equation 3.32}$$

$N_c$  is the number of scattering centers within a particle,  $r_{ij}$  is the distance between two scattering centers  $i$  and  $j$ .

The mean squared radius of gyration is defined as:

$$\langle R_g^2 \rangle = \frac{1}{2N_c^2} \sum_i^{N_c} \sum_j^{N_c} \langle r_{ij}^2 \rangle \quad \text{Equation 3.33}$$

what leads in monodisperse case to:

$$P(q) = 1 - \frac{1}{3}q^2\langle R_g^2 \rangle + \dots \quad \text{Equation 3.34}$$

Polydispersity influences the mean squared radius of gyration:

$$\langle R_g^2 \rangle_z = \frac{\sum_i m_i M_i \langle R_g^2 \rangle_i}{\sum_i m_i M_i} \quad \text{Equation 3.35}$$

$\langle R_g^2 \rangle_z$  is the  $z$ -average of the square of the radius of gyration and  $\langle R_g^2 \rangle_i$  is the square of the radius of gyration of the particle  $i$ ;  $m_i$  and  $M_i$  are the mass and the molar mass of particle  $i$ , respectively.

Equation 3.28 can be now rewritten as:

$$\frac{K_o c}{R_{vv}} = \left( \frac{1}{M_w P_z(q)} + 2A_2 c + 3A_3 c^2 + \dots \right) \quad \text{Equation 3.36}$$

from where the weight averaged molecular weight  $M_w$ , and the radius of gyration  $R_g$  can be calculated through the relation:

$$\frac{c K_o}{R_{vv}} = \frac{1}{M_w} \left( 1 + 2A_2 M_w c + \frac{q^2 R_g^2}{3} \right) \quad \text{Equation 3.37}$$

In case of particles larger than 50 nm, the Berry plot is commonly used to extract the weight averaged molecular weight  $M_w$ , and the radius of gyration  $R_g$  according to the following equation:

$$\left( \frac{c K_o}{R_{vv}} \right)^{1/2} = \left( \frac{1}{M_w} \right)^{1/2} \left\{ 1 + \frac{q^2 R_g^2}{6} + \dots \right\} \quad \text{Equation 3.38}$$

### 3.6.1.3 Application of PCS to the Polymersomes Characterization

Polymersomes are represented by a modified Rayleigh-Gans-Debye (RGD) approach of the total scattered intensity  $I_p$  for a coated sphere<sup>133</sup>:

$$I(q) = \left[ (m_1 - 1) \left( \frac{3j_1(x)}{x} + f^3 \frac{m_2 - m_1}{m_1 - 1} \frac{3j_1(fx)}{fx} \right) \right]^2 \quad \text{Equation 3.39}$$

$R_p$  – polymersome outer radius and

$$x = R_p \cdot q, \quad f = 1 - d/R_p,$$

$d$  – bilayer thickness

$m_1 = n_B/n_0$  the relative refractive index of the shell divided by the refractive index of the solvent

$m_2 = n_{IN}/n_0$  the relative refractive index of the lumen divided by the refractive index of the solvent

$j_1(x)$  is the first-order spherical Bessel function.

The schematic optical model of a polymersome is presented in *Figure 3.21*.

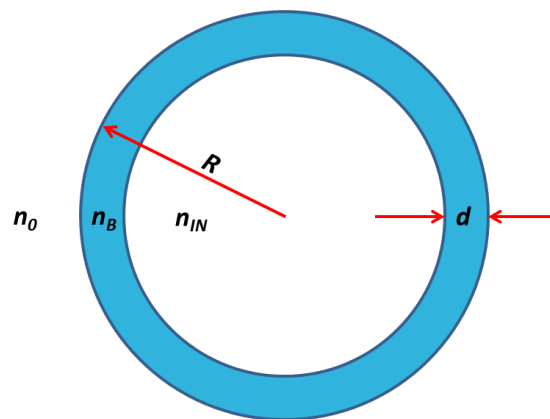


**Figure 3.21** Optical model of a vesicle;  $n_0$ ,  $n_B$  and  $n_{IN}$  are refractive indices of the medium (solvent), bilayer and lumen of the vesicle, respectively;  $d$  is the thickness of the bilayer

The scattered intensity of a polydisperse polymersomes system is given by:

$$I(q, R) = \frac{\int R^6 f_g(R) I_p dR}{\int R^6 f_g(R) dR} \quad \text{Equation 3.40}$$

with  $f_g(R)$  - two-parameter unimodal Schulz distribution for fraction of particles having a radius  $R$ <sup>134</sup>

$$f_g(R) = \frac{1}{m!} \left[ \left( \frac{m+1}{\bar{R}} \right)^{m+1} R^m e^{-\frac{(m+1)r}{\bar{R}}} \right] \quad \text{Equation 3.41}$$

$\bar{R}$  the number average size of the particle

$m$  a parameter that measures the width of the distribution with

$$m = \frac{1}{PD-1}, m \in \mathbb{N}. \quad \text{Equation 3.42}$$

The description of the translational diffusion employs usually polydispersity which improves the quality of the information gained from the data analysis. As PCS experiment is in some sense insensitive to the macromolecular polydispersity, incorporation of  $f_g(R)$  into the description of the diffusion provides information with reasonable degree of accuracy. For the accurate description of polymersomes incorporation of not only the polydispersity parameter but also parameter sensitive to the refractive index change is necessary. This can be achieved by using an average refractive index for the lumen differing from the outside refractive index of the vesicle. To describe the  $q$ -dependence of the diffusion coefficient (Equation 3.25) the following formula was used:<sup>135</sup>

$$\frac{\Gamma(q)}{q^2} = \frac{\int \frac{f_g(R) I_p D_i}{R^2} dR}{\int \frac{f_g(R) I_p}{R^2} dR} \quad \text{Equation 3.43}$$

### 3.6.2 Basic Principles of Fluorescence Correlation Spectroscopy (FCS)

The use of fluorescence correlation spectroscopy (FCS) is rapidly growing in biological and biophysical research due to the possibility of a precise characterization of the chemical, physical, and dynamic properties of versatile molecules.<sup>136, 137</sup>

Berland writes in his text book about FCS: “Fluorescence correlation spectroscopy is a form of fluctuation spectroscopy in which the properties of an experimental system are revealed through statistical analysis of spontaneous equilibrium fluctuations in the fluorescence signal measured from within a minute sample volume. Fluctuations may arise due to molecules diffusing into or out of the volume, as well as from chemical or photophysical reactions.”<sup>136</sup>

Figure 3.22 illustrates the basic principle of FCS.

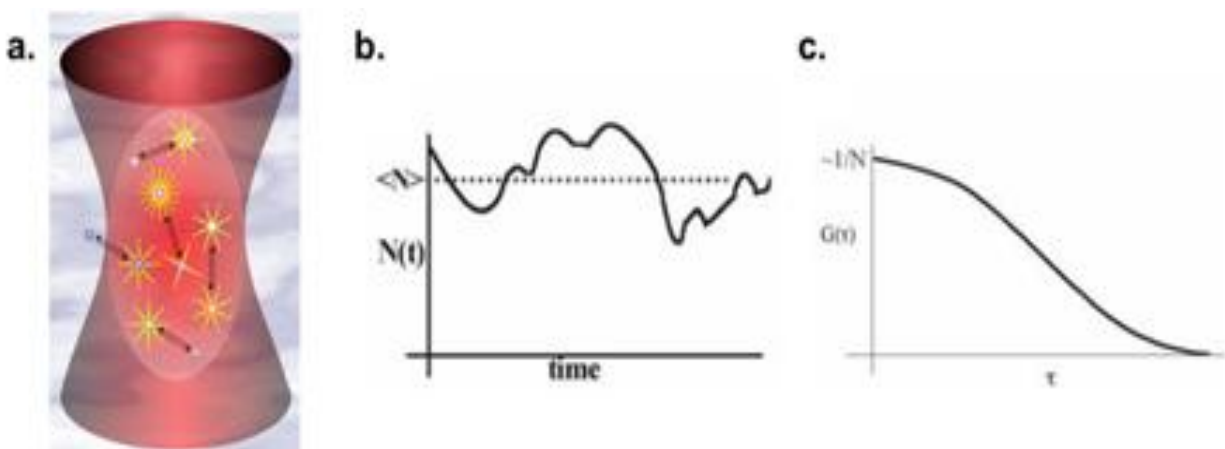


**Figure 3.22** **a.** Molecular mechanisms that might give rise to fluorescence fluctuations comprise particle movements, conformational changes, chemical or photophysical reactions;<sup>†††</sup> **b.** as molecules diffuse in and out of the volume, the number in the volume will fluctuate as described in the text; **c.** correlation functions calculated from the fluctuation data are analyzed to determine diffusion coefficients and molecular concentrations.<sup>136</sup> (Used with permission of Springer)

<sup>†††</sup> <http://www.biophysics.org/portals/1/pdfs/education/schwille.pdf>

The average fluorescence signal  $\langle F_i \rangle$  is proportional to the number of molecules ( $N$ ) that occupy the detection volume ( $V_{\text{eff}}$ ). The size of the detection volume can be calculated from the reference measurements of the species with known diffusion coefficient. By knowing the size of the detection volume one can calculate absolute molecular concentration  $C_i$ . One may write:

$$\langle F_i \rangle = \psi_i \langle C_i \rangle V_{\text{eff}} = \psi_i \langle N_i \rangle \quad \text{Equation 3.44}$$

where  $\psi_i$  is the average “brightness” of the fluorescent species.

The theoretical form for the fluorescence autocorrelation functions,  $G(\tau)$ , can be written as:<sup>136</sup>

$$G(\tau) = \frac{\langle \delta F \delta F(t + \tau) \rangle}{\langle F(t) \rangle} \quad \text{Equation 3.45}$$

where:

$$\delta F(t) = F(t) - \langle F(t) \rangle \quad \text{Equation 3.46}$$

is the fluorescence fluctuation. Assuming that the fluorescence fluctuation arises only due to the concentration fluctuations of the detected fluorescent species the problem can be described by:

$$\delta F(t) = \int E(r) \delta(C_r, t) dV \quad \text{Equation 3.47}$$

where  $\delta(C_r, t)$  is the concentration fluctuation and  $E(r)$  are the temporarily independent emission characteristics, including the brightness of the fluorescent species and the spatial detection function. Considering only the three dimensional diffusion being the reason for the concentration fluctuation, it has been shown theoretically for an ensemble of  $m$  different types of freely diffusing fluorescence species,  $G(t)$  has the following analytical form:<sup>138</sup>

$$G(t) = 1 + \frac{1}{N_F} \sum_{i=1}^m \frac{f_i}{\left[1 + \frac{t}{\tau_{Di}}\right] \sqrt{1 + \frac{t}{S^2 \tau_{Di}}}} \quad \text{Equation 3.48}$$

Here,  $N_F$  is the average number of diffusing fluorescence species in the observation volume,  $\tau_{Di}$  is the diffusion time of the  $i$ -th type of species,  $f_i$  is their fraction and  $S$  is the so-called structure parameter  $S = z_0/r_0$ , where  $z_0$  and  $r_0$  represent the axial and the radial dimensions of the confocal observation volume, respectively. With other words the amplitude of the correlation functions  $G(0)$  is directly related to the average number of molecules within the observation volume (approx.  $1/N$ ), and the temporal decay of the correlation function specifies the average occupancy time of molecules diffusing through the volume. Furthermore the diffusion time,  $\tau_{Di}$ , is related to the respective diffusion coefficient,  $D_i$ , through:

$$D_i = \frac{r_0^2 + R_{h,i}^2}{4\tau_i} \quad \text{Equation 3.49}$$

where  $R_{h,i}$  is the hydrodynamic radius of the observed objects, which is also connected to the diffusion coefficient through the Stokes-Einstein relationship (*Equation 3.25*). Thus a fit of an experimental autocorrelation function with *Equation 3.48* provides the overall concentration of the fluorescent species  $c=N/V$ , as well as the hydrodynamic radius  $R_{h,i}$  and the number fraction  $f_i$  of each diffusing component.

### 3.6.3 Basic Principles of Atomic Force Microscopy (AFM)

During the atomic force measurement, a sharp tip attached to the end of a cantilever is brought in contact with the sample. The tip is then scanned over the surface of the sample by moving either the tip or the sample. The surface topography causes deflection of the cantilever and this deflection is measured using a laser beam that is reflected from the backside of the cantilever onto a split photodiode (see schematic setup on *Figure 3.23*). Height traces of the single scan lines are then put together to a three-dimensional surface topography by software on the control computer.<sup>139</sup>

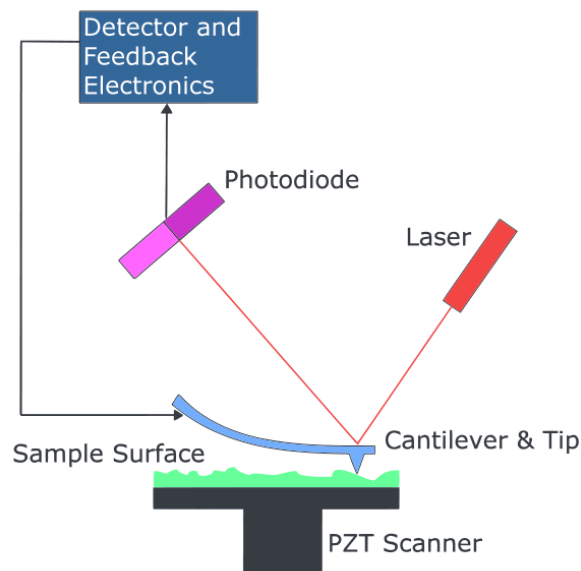


**Figure 3.23** Schematic of an AFM setup (see text)<sup>†††</sup>

Atomic force microscopy studies can be performed in different gases, in vacuum, or in liquids by using specially designed cells. Measurements in liquid environments can be performed in a variety of different liquid cells which typically, consist of a special transparent cantilever

<sup>†††</sup> [http://en.wikipedia.org/wiki/Atomic\\_force\\_microscopy](http://en.wikipedia.org/wiki/Atomic_force_microscopy)

holder that forms the upper lid of the cell, an O-ring sealing the cell from the side, and the sample surface forming the bottom of the cell.<sup>139</sup>

An atomic force microscope can be operated in both contact and non-contact mode. In the contact mode operation, the static tip deflection is used directly as a feedback signal. In this mode, the tip of the cantilever does not contact the sample surface. In the non-contact mode the cantilever is oscillated at a frequency slightly above its resonant frequency. Long range forces which extend above the surface (for example van der Waals forces) act to decrease the resonance frequency of the cantilever. This decrease in resonant frequency combined with the feedback loop system maintains a constant oscillation amplitude or frequency by adjusting the average tip-to-sample distance. The measurement of the tip-to-sample distance at each  $(x,y)$  data point allows the scanning software to construct a topographic image of the sample surface. The third commonly used operation mode is called tapping-mode in which the cantilever is driven to oscillate up and down near to resonance frequency by a small piezoelectric element mounted in the AFM tip holder similar to non-contact mode. The difference however is in the amplitude of these oscillations which is much higher in the tapping mode (100 - 200 nm) than in the non-contact mode (less than 10 nm). However, the amplitude of this oscillation is greater than 10 nm, typically 100 to 200 nm. The interaction of forces acting on the cantilever when the tip comes close to the surface cause the amplitude of this oscillation to decrease as the tip gets closer to the sample. The height of the cantilever above the sample is controlled by a piezoelectric actuator. The tapping-mode is the least destructive method allowing visualization of very sensitive objects like supported lipid bilayers of vesicles adsorbed on the surface.<sup>140</sup>

Besides imaging, another major application of AFM is force spectroscopy, as described by Butt and Kappel:<sup>139</sup> "In a force spectroscopy measurement the piezoelectric translator moves with constant velocity up and down so that its position versus time can be described by a

triangular function while the detector signal of the photodiode is recorded. The outcome of such a measurement is a measure of the cantilever deflection,  $Z_c$ , versus position of the piezotranslator,  $Z_p$ , normal to the sample surface.” A schematic example is described in *Figure 3.24*.

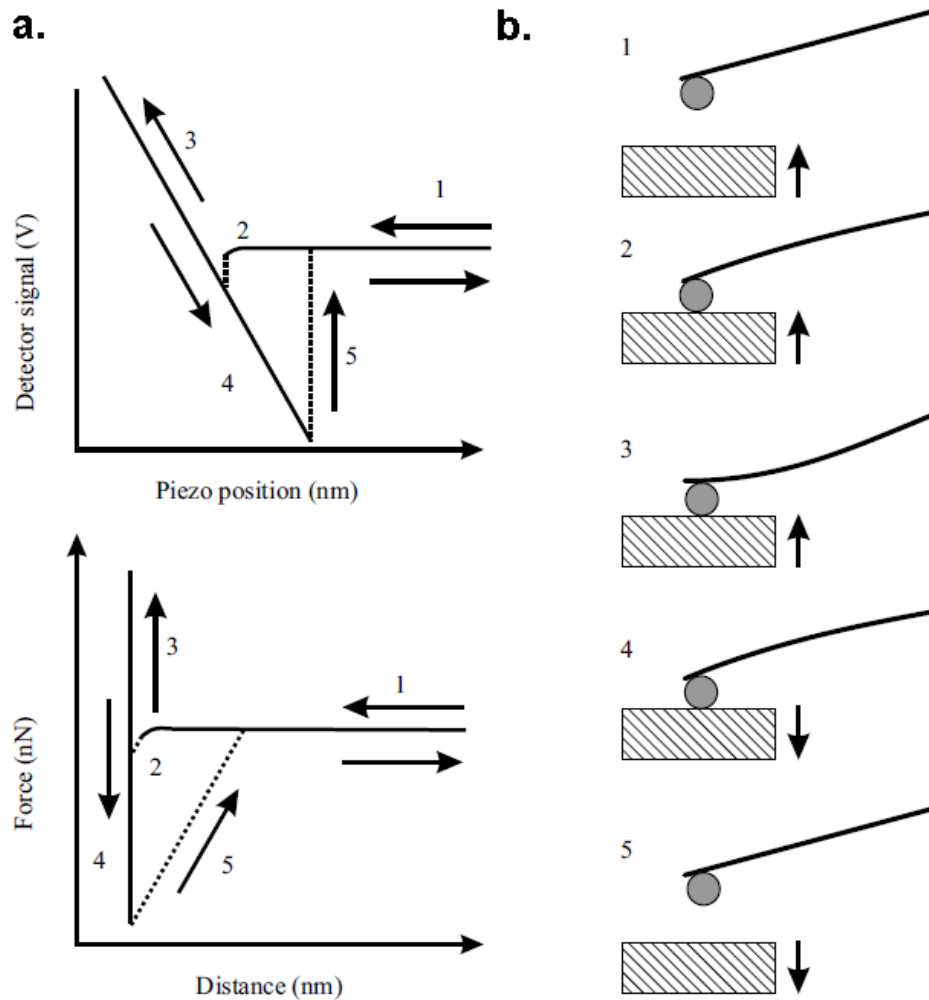


**Figure 3.24** Schematic of an AFM measurement. (1) Zero force region, where probe and surface are far from each other; (2) snap-in to surface due to attractive force; (3) approach part of the constant compliance region, where probe and surface move up in parallel; (4) retract part of the constant compliance region, where probe and surface move down in parallel and adhesion leads to negative bending; and (5) jump-out occurs when the restoring force of the cantilever exceeds the adhesion force. **a.** Detector signal versus piezoactuator position. **b.** Force versus distance curve derived from a. (Used with permission of Wiley-VCH Verlag GmbH & Co. KGaA)<sup>§§§</sup>

<sup>§§§</sup> Butt, H. J.; Kappl, M., *Surface and interfacial forces*. Wiley-VCH Verlag GmbH & Co. : 2010

When the distance between the cantilever and the surface is large enough, the deflection is equal to zero as there are no forces acting on the cantilever (*Figure 3.24b.1*). As the distance between the cantilever and the surface decreases, the deflection of the cantilever due to the surface forces is observed (*Figure 3.24b.2*). When the attractive forces exceed the spring constant of the cantilever, the probe jump in contact with the surface is observed (dotted line). Afterwards the cantilever and surface are moving in parallel.

To extract a real force-versus-distance curve, the cantilever deflection and position of the piezotranslator need to be converted to force and distance. This according to Butt and Kappl can be done in following steps:<sup>139</sup> “First, a line fit is done on the zero force region to subtract any offset in the detector signal. Then, a linear fit of the constant compliance region is done to obtain the slope that is equal to the conversion factor between detector signal in Volts and cantilever deflection in nanometers. The tip–sample separation  $B$  is calculated by adding the deflection to the piezotranslator position  $B = Z_p + Z_c$  and the force  $F$  is obtained by multiplying the deflection  $Z_c$  with the spring constant  $K_c$  of the cantilever. A critical point in the evaluation of AFM force curves is the determination of zero distance, meaning the point where the probe starts to touch the surface.”

Spectroscopy force measurements have been successfully applied to probe van der Waals and Casimir forces, nanoscale contacts, atomic bonding, dissolution forces in liquids and single molecule stretching and rupture forces. Forces of the order of a few piconewtons were proven to be accessible during routine measurement with a vertical distance resolution of better than 0.1 nanometers.<sup>141</sup>

### 3.6.4 Basic Principles of Transmission Electron Microscopy (TEM)

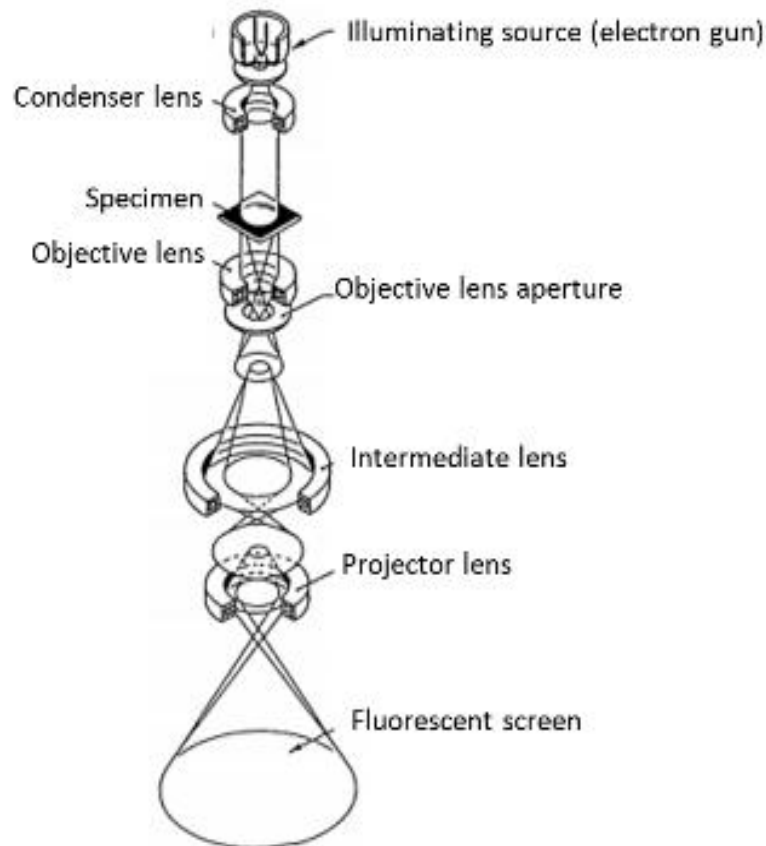
The smallest distance that can be resolved by a microscope is called resolution of a microscope and it can be calculated using the Abbe theory of images formation for optic systems.

For incoherent light or electron beam it is:

$$\delta = \frac{0.61\lambda_r}{\sin\alpha_{ir}}$$

**Equation 3.50**

where  $\lambda_r$  is the wavelength of the radiation,  $\alpha_{ir}$  is the maximum angle between the incident and deflected beam in the limit of the lens aberrations.



\*\*\*\*

**Figure 3.25** Schematic representation of the transmission electron microscope with the most important compartments.

\*\*\*\* adapted from [http://www.stcloudstate.edu/cmia/documents/Invitation\\_to\\_the\\_SEM\\_World.pdf](http://www.stcloudstate.edu/cmia/documents/Invitation_to_the_SEM_World.pdf)

For optical microscopy the resolution is limited by the wavelength of incident light (410-660 nm). Since according to de Broglie's the wavelength of electrons is related to their energy,  $E$ .<sup>142</sup>

$$\lambda_e \sim \frac{1.22}{E^{\frac{1}{2}}}$$

**Equation 3.51**

So for 100 keV electrons, we see that  $\lambda_e \sim 4$  pm, which is much smaller than the diameter of the atom.<sup>142</sup>

A schematic picture of a transmission electron microscope construction is shown in *Figure 3.25*. A typical transmission electron microscope can be divided into two main parts: the illumination system and the imaging system. The illumination system consists of a source of the electron (electron gun) and the condenser lens which focus this beam on the specimen. The specimen is located between the illumination and the imaging system. The imaging system is a series of lenses, which focuses the beam after it passes through the specimen and recording system which converts the radiation. In a typical transmission electron microscopy experiment a beam of electrons is transmitted through a very thin specimen. Transmission electron microscopy relies on electron density contrast within a thin film of a sample to provide an image due to spatial variations in transmission of the electron beam.<sup>143</sup> Subsequently the image is magnified and focused onto an imaging device, such as a fluorescent screen or CCD camera.

Cryogenic transmission electron microscopy (cryo-TEM) is a technique where transmission electron microscopy is used to image cryogenically cooled samples. Rapid cooling into cryogenic liquids is intended to 'trap' structures formed in solution, by vitrifying the sample and avoiding crystallization in the solvent.<sup>143</sup> It is the only technique available, which provides nanometer-scale resolution three-dimensional imaging directly in complex fluids. It is desired especially in study of complex self-assembled colloids that the visualized object is same as the one present in

solution. As these self-assembled structures are very sensitive to the environmental condition, even small deviations in the solvent composition result in changes of the object morphology. Particularly for biological samples, self-assemblies of lipids and “soft” copolymers imaging conditions are crucial in order to visualize exact structures which are present in solution. Drying or vitrification can lead to permanent change in sample morphology.

The artifact that simply cannot be avoided is the size segregation of dispersed particles.<sup>144</sup> This is rooted directly in the thickness of the formed film. Particles larger than the film thickness are excluded from the center of the sample and usually gathered around the edge of a hole. In this sense also, interpretation of images of objects greater than the film thickness (200-400nm) can be misleading. Another type of artifact arises from the sample preparation. The blotting process may have a significant influence on the structure/shape of imaging objects; it can be however controlled to a great extent. At this point also humidity control needs to be monitored in order to avoid any water evaporation.<sup>144, 145</sup>

In order to image interactions of flexible PDMS-*b*-PMOXA vesicles with colloidal nanoparticles cryogenic microscopy is essential. As the shape of the vesicle (curvature) is very important for successful nanoparticle incorporation, in order to make comparison between microscopy and spectroscopic measurements, one needs to image samples in their native environment. Careful sample preparation is crucial here, allowing diminution of artifacts. As we cannot completely avoid artifacts, awareness of them still can lead to reliable interpretation (See Chapter. 5.1.3.4).

### 3.7 References

1. Vance, D. E., *Biochemistry of lipids, lipoproteins and membranes*. Elsevier Science: **2008**; Vol. 42.
2. Van Meer, G.; Voelker, D. R.; Feigenson, G. W., Membrane lipids: where they are and how they behave. *Nat. Rev. Mol. Cell Biol.* **2008**, *9*, 112-124.
3. Gurr, M. I.; Harwood, J. L.; Frayn, K. N., *Lipid biochemistry*. Wiley Online Library: **2002**.
4. Alberts, B.; Johnson, A.; Lewis, J.; Raff, M.; Roberts, K.; Walter, P., *Molecular biology of the cell*. Garland Science: **2002**; Vol. 5.
5. Lasic, D. D., *Liposomes: from physics to applications*. Elsevier Amsterdam **1993**.
6. Lipowsky, R.; Sackmann, E., *Structure and dynamics of membranes: From cells to vesicles*. Elsevier Science: **1995**.
7. Yeagle, P. L., Cholesterol and the cell membrane. *BBA-Biomembranes* **1985**, *822*, 267-287.
8. Odian, G. G., *Principles of polymerization*. John Wiley and Sons: **2004**.
9. Kita-Tokarczyk, K.; Grumelard, J.; Haefele, T.; Meier, W., Block copolymer vesicles—using concepts from polymer chemistry to mimic biomembranes. *Polymer* **2005**, *46*, 3540-3563.
10. Taubert, A.; Napoli, A.; Meier, W., Self-assembly of reactive amphiphilic block copolymers as mimetics for biological membranes. *Curr. Opin. Chem. Biol.* **2004**, *8*, 598-603.
11. Mecke, A.; Dittrich, C.; Meier, W., Biomimetic membranes designed from amphiphilic block copolymers. *Soft Matter* **2006**, *2*, 751-759.
12. Helfand, E.; Wasserman, Z., *Microdomain Structure and the Interface in Block Copolymers*. **1982**; Vol. 1, p 99-125.
13. Bates, F. S.; Fredrickson, G. H., Block copolymer thermodynamics: theory and experiment. *Annu. Rev. Phys. Chem.* **1990**, *41*, 525-557.
14. Lim Soo, P.; Eisenberg, A., Preparation of block copolymer vesicles in solution. *J. Polym. Sci., Part B: Polym. Phys.* **2004**, *42*, 923-938.
15. Zhang, L.; Eisenberg, A., Formation of crew-cut aggregates of various morphologies from amphiphilic block copolymers in solution. *Polym. Adv. Technol.* **1998**, *9*, 677-699.
16. Discher, D. E.; Eisenberg, A., Polymer vesicles. *Science* **2002**, *297*, 967.
17. Lindman, B., *Amphiphilic block copolymers: self-assembly and applications*. Elsevier Science: **2000**.
18. Kauzmann, W., Some factors in the interpretation of protein denaturation. *Adv. Protein Chem* **1959**, *14*, 63.
19. Chandler, D., Interfaces and the driving force of hydrophobic assembly. *Nature* **2005**, *437*, 640-647.
20. Boal, D., *Mechanics of the Cell*. Cambridge Univ Pr: **2011**.
21. Israelachvili, J. N., *Intermolecular and surface forces*. Academic press: **2011**.
22. Zhang, J.; Li, X., Stimuli-Triggered Structural Engineering of Synthetic and Biological Polymeric Assemblies. *Prog. Polym. Sci.* **2011**.
23. Antonietti, M.; Förster, S., Vesicles and Liposomes: A Self-Assembly Principle Beyond Lipids. *Adv. Mater.* **2003**, *15*, 1323-1333.
24. Singer, S. J.; Nicolson, G. L., The fluid mosaic model of the structure of cell membranes. *Science* **1972**, *175*, 720-731.
25. Marsh, D., *Handbook of Lipid Bilayers, Second Edition*. Taylor & Francis: **2010**.

26. Sten-Knudsen, O., *Biological membranes: theory of transport, potentials and electric impulses*. Cambridge Univ Pr: **2002**.
27. Luckey, M., *Membrane structural biology: with biochemical and biophysical foundations*. Cambridge Univ Pr: **2008**.
28. Singer, S.; Nicolson, G. L., The fluid mosaic model of the structure of cell membranes. *Landmark Papers in Cell Biology* **1972**, 296-307.
29. Needham, D.; Nunn, R. S., Elastic deformation and failure of lipid bilayer membranes containing cholesterol. *Biophys. J.* **1990**, *58*, 997-1009.
30. Koenig, B. W.; Strey, H. H.; Gawrisch, K., Membrane lateral compressibility determined by NMR and x-ray diffraction: effect of acyl chain polyunsaturation. *Biophys. J.* **1997**, *73*, 1954-1966.
31. Brochard, F.; Lennon, J., Frequency spectrum of the flicker phenomenon in erythrocytes. *J. Phys.* **1975**, *36*, 1035-1047.
32. Hochmuth, R. M., Micropipette aspiration of living cells. *J. Biomech.* **2000**, *33*, 15-22.
33. Evans, E., New membrane concept applied to the analysis of fluid shear-and micropipette-deformed red blood cells. *Biophys. J.* **1973**, *13*, 941.
34. Evans, E.; Rawicz, W., Entropy-driven tension and bending elasticity in condensed-fluid membranes. *Phys. Rev. Lett.* **1990**, *64*, 2094-2097.
35. Parsegian, V.; Fuller, N.; Rand, R., Measured work of deformation and repulsion of lecithin bilayers. *Proc. Natl. Acad. Sci.* **1979**, *76*, 2750.
36. Kwok, R.; Evans, E., Thermoelasticity of large lecithin bilayer vesicles. *Biophys. J.* **1981**, *35*, 637.
37. Zhelev, D. V., Material property characteristics for lipid bilayers containing lysolipid. *Biophys. J.* **1998**, *75*, 321-330.
38. Mutz, M.; Helfrich, W., Bending rigidities of some biological model membranes as obtained from the Fourier analysis of contour sections. *J. Phys.* **1990**, *51*, 991-1001.
39. Evans, E.; Waugh, R., Osmotic correction to elastic area compressibility measurements on red cell membrane. *Biophys. J.* **1977**, *20*, 307-313.
40. Evans, E.; Waugh, R., Mechano-chemistry of closed, vesicular membrane systems. *J. Colloid Interface Sci.* **1977**, *60*, 286-298.
41. Evans, E. A., Bending elastic modulus of red blood cell membrane derived from buckling instability in micropipet aspiration tests. *Biophys. J.* **1983**, *43*, 27-30.
42. Henriksen, J.; Rowat, A. C.; Brief, E.; Hsueh, Y.; Thewalt, J.; Zuckermann, M.; Ipsen, J. H., Universal behavior of membranes with sterols. *Biophys. J.* **2006**, *90*, 1639-1649.
43. Sweitzer, S. M.; Hinshaw, J. E., Dynamin undergoes a GTP-dependent conformational change causing vesiculation. *Cell* **1998**, *93*, 1021-1029.
44. Merrifield, C. J.; Perrais, D.; Zenisek, D., Coupling between clathrin-coated-pit invagination, cortactin recruitment, and membrane scission observed in live cells. *Cell* **2005**, *121*, 593-606.
45. Merrifield, C. J.; Feldman, M. E.; Wan, L.; Almers, W., Imaging actin and dynamin recruitment during invagination of single clathrin-coated pits. *Nat. Cell Biol.* **2002**, *4*, 691-698.
46. Chan, Y. H. M.; Boxer, S. G., Model membrane systems and their applications. *Curr. Opin. Chem. Biol.* **2007**, *11*, 581-587.
47. Zepik, H.; Walde, P.; Kostoryz, E.; Yourtee, D., Lipid vesicles as membrane models for toxicological assessment of xenobiotics. *Crit. Rev. Toxicol.* **2008**, *38*, 1-11.

48. Ringsdorf, H.; Schlarb, B.; Venzmer, J., Molecular architecture and function of polymeric oriented systems: models for the study of organization, surface recognition, and dynamics of biomembranes. *Angew. Chem. Int. Ed.* **1988**, *27*, 113-158.
49. Naumann, R.; Schiller, S. M.; Giess, F.; Grohe, B.; Hartman, K. B.; Kärcher, I.; Köper, I.; Lübber, J.; Vasilev, K.; Knoll, W., Tethered lipid bilayers on ultraflat gold surfaces. *Langmuir* **2003**, *19*, 5435-5443.
50. Sackmann, E., Supported membranes: scientific and practical applications. *Science* **1996**, *271*, 43-48.
51. Tanaka, M.; Sackmann, E., Polymer-supported membranes as models of the cell surface. *Nature* **2005**, *437*, 656-663.
52. Belegriou, S.; Dorn, J.; Kreiter, M.; Kita-Tokarczyk, K.; Sinner, E. K.; Meier, W., Biomimetic supported membranes from amphiphilic block copolymers. *Soft Matter* **2009**, *6*, 179-186.
53. Tanner, P.; Egli, S.; Balasubramanian, V.; Onaca, O.; Palivan, C. G.; Meier, W., Can polymeric vesicles that confine enzymatic reactions act as simplified organelles? *FEBS Lett.* **2011**.
54. Marguet, M.; Edembe, L.; Lecommandoux, S., Polymersomes in Polymersomes: Multiple Loading and Permeability Control. *Angew. Chem. Int. Ed.* **2012**, *124*, 1199-1202.
55. Feigenson, G. W., Phase boundaries and biological membranes. *Annu. Rev. Biophys. Biomol. Struct.* **2007**, *36*, 63.
56. Voeltz, G. K.; Prinz, W. A.; Shibata, Y.; Rist, J. M.; Rapoport, T. A., A class of membrane proteins shaping the tubular endoplasmic reticulum. *Cell* **2006**, *124*, 573-586.
57. Groves, J. T., Bending mechanics and molecular organization in biological membranes. *Annu. Rev. Phys. Chem.* **2007**, *58*, 697-717.
58. Nath, A.; Atkins, W. M.; Sligar, S. G., Applications of phospholipid bilayer nanodiscs in the study of membranes and membrane proteins. *Biochemistry* **2007**, *46*, 2059-2069.
59. Kraft, M. L.; Weber, P. K.; Longo, M. L.; Hutcheon, I. D.; Boxer, S. G., Phase separation of lipid membranes analyzed with high-resolution secondary ion mass spectrometry. *Science* **2006**, *313*, 1948-1951.
60. Danelon, C.; Perez, J. B.; Santschi, C.; Brugger, J.; Vogel, H., Cell membranes suspended across nanoaperture arrays. *Langmuir* **2006**, *22*, 22-25.
61. Atanasov, V.; Atanasova, P. P.; Vockenroth, I. K.; Knorr, N.; Köper, I., A molecular toolkit for highly insulating tethered bilayer lipid membranes on various substrates. *Bioconjugate Chem.* **2006**, *17*, 631-637.
62. Yoshina-Ishii, C.; Chan, Y. H. M.; Johnson, J. M.; Kung, L. A.; Lenz, P.; Boxer, S. G., Diffusive dynamics of vesicles tethered to a fluid supported bilayer by single-particle tracking. *Langmuir* **2006**, *22*, 5682-5689.
63. Ayton, G. S.; Voth, G. A., Multiscale simulation of transmembrane proteins. *J. Struct. Biol.* **2007**, *157*, 570-578.
64. Mueller, P.; Rudin, D. O.; Ti Tien, H.; Wescott, W. C., Reconstitution of cell membrane structure in vitro and its transformation into an excitable system. *Nature* **1962**, *194*, 979-980.
65. Montal, M.; Mueller, P., Formation of bimolecular membranes from lipid monolayers and a study of their electrical properties. *Proc. Natl. Acad. Sci.* **1972**, *69*, 3561.
66. Tien, H. T.; Ottova-Leitmannova, A., *Membrane biophysics: as viewed from experimental bilayer lipid membranes (planar lipid bilayers and spherical liposomes)*. Elsevier Science: **2000**; Vol. 5.

67. Castellana, E. T.; Cremer, P. S., Solid supported lipid bilayers: From biophysical studies to sensor design. *Surf. Sci. Rep.* **2006**, *61*, 429-444.
68. Nardin, C.; Winterhalter, M.; Meier, W., Giant free-standing ABA triblock copolymer membranes. *Langmuir* **2000**, *16*, 7708-7712.
69. Meier, W.; Nardin, C.; Winterhalter, M., Reconstitution of channel proteins in (polymerized) ABA triblock copolymer membranes. *Angew. Chem. Int. Ed.* **2000**, *39*, 4599-4602.
70. Olson, F.; Hunt, C.; Szoka, F.; Vail, W.; Papahadjopoulos, D., Preparation of liposomes of defined size distribution by extrusion through polycarbonate membranes. *BBA-Biomembranes* **1979**, *557*, 9-23.
71. Le Bihan, O.; Bonnafous, P.; Marak, L.; Bickel, T.; Trépout, S.; Mornet, S.; De Haas, F.; Talbot, H.; Taveau, J. C.; Lambert, O., Cryo-electron tomography of nanoparticle transmigration into liposome. *J. Struct. Biol.* **2009**, *168*, 419-425.
72. Jaskiewicz, K.; Larsen, A.; Lieberwirth, I.; Koynov, K.; Meier, W.; Fytas, G.; Kroeger, A.; Landfester, K., Probing Bioinspired Transport of Nanoparticles into Polymersomes. *Angew. Chem. Int. Ed.* **2012**, *124*, 4691-4695.
73. Jaskiewicz, K.; Larsen, A.; Schaeffel, D.; Koynov, K.; Lieberwirth, I.; Fytas, G.; Landfester, K.; Kroeger, A., Incorporation of Nanoparticles into Polymersomes: Size and Concentration Effects. *ACS nano* **2012**, *6*, 7254-7262.
74. Fisar, Z.; Krulík, R.; Beitlová, D., Liposomes--model membranes to study the binding of tricyclic antidepressants. *Drug Metabol. Drug. Interact.* **1991**, *9*, 269.
75. Ringsdorf, H.; Sackmann, E.; Simon, J.; Winnik, F. M., Interactions of liposomes and hydrophobically-modified poly-(N-isopropylacrylamides): an attempt to model the cytoskeleton. *BBA-Biomembranes* **1993**, *1153*, 335-344.
76. Bagatolli, L.; Gratton, E., Two photon fluorescence microscopy of coexisting lipid domains in giant unilamellar vesicles of binary phospholipid mixtures. *Biophys. J.* **2000**, *78*, 290-305.
77. Veatch, S.; Polozov, I.; Gawrisch, K.; Keller, S., Liquid domains in vesicles investigated by NMR and fluorescence microscopy. *Biophys. J.* **2004**, *86*, 2910-2922.
78. Korlach, J.; Schwille, P.; Webb, W. W.; Feigenson, G. W., Characterization of lipid bilayer phases by confocal microscopy and fluorescence correlation spectroscopy. *Proc. Natl. Acad. Sci.* **1999**, *96*, 8461.
79. Kahya, N.; Scherfeld, D.; Bacia, K.; Poolman, B.; Schwille, P., Probing lipid mobility of raft-exhibiting model membranes by fluorescence correlation spectroscopy. *J. Biol. Chem.* **2003**, *278*, 28109-28115.
80. Chemin, M.; Brun, P. M.; Lecommandoux, S.; Sandre, O.; Le Meins, J. F., Hybrid polymer/lipid vesicles: fine control of the lipid and polymer distribution in the binary membrane. *Soft Matter* **2012**, *8*, 2867-2874.
81. Sharma, A.; Sharma, U. S., Liposomes in drug delivery: progress and limitations. *Int. J. Pharm.* **1997**, *154*, 123-140.
82. Schulz, M.; Olubummo, A.; Binder, W. H., Beyond the lipid-bilayer: interaction of polymers and nanoparticles with membranes. *Soft Matter* **2012**, *8*, 4849-4864.
83. Batzri, S.; Korn, E. D., Single bilayer liposomes prepared without sonication. *BBA-Biomembranes* **1973**, *298*, 1015-1019.
84. Knoll, W.; Köper, I.; Naumann, R.; Sinner, E. K., Tethered bimolecular lipid membranes—a novel model membrane platform. *Electrochim. Acta* **2008**, *53*, 6680-6689.
85. Le Meins, J. F.; Sandre, O.; Lecommandoux, S., Recent trends in the tuning of polymersomes' membrane properties. *Eur. Phys. J. E Soft Matter* **2011**, *34*, 1-17.

86. Bermudez, H.; Brannan, A. K.; Hammer, D. A.; Bates, F. S.; Discher, D. E., Molecular weight dependence of polymersome membrane structure, elasticity, and stability. *Macromolecules* **2002**, *35*, 8203-8208.
87. Blok, M.; Van der Neut-Kok, E.; Van Deenen, L.; De Gier, J., The effect of chain length and lipid phase transitions on the selective permeability properties of liposomes. *BBA-Biomembranes* **1975**, *406*, 187-196.
88. Chen, R.; Pearce, D. J. G.; Fortuna, S.; Cheung, D. L.; Bon, S. A. F., Polymer Vesicles with a Colloidal Armor of Nanoparticles. *J. Am. Chem. Soc.* **2011**, *133*, 2151-2153.
89. Letchford, K.; Burt, H., A review of the formation and classification of amphiphilic block copolymer nanoparticulate structures: micelles, nanospheres, nanocapsules and polymersomes. *Eur. J. Pharm. Biopharm.* **2007**, *65*, 259-269.
90. LoPresti, C.; Lomas, H.; Massignani, M.; Smart, T.; Battaglia, G., Polymersomes: nature inspired nanometer sized compartments. *J. Mater. Chem.* **2009**, *19*, 3576-3590.
91. Tamm, L. K.; McConnell, H. M., Supported phospholipid bilayers. *Biophys. J.* **1985**, *47*, 105-113.
92. Cremer, P. S.; Boxer, S. G., Formation and spreading of lipid bilayers on planar glass supports. *J. Phys. Chem. B* **1999**, *103*, 2554-2559.
93. Brian, A. A.; McConnell, H. M., Allogeneic stimulation of cytotoxic T cells by supported planar membranes. *Proc. Natl. Acad. Sci.* **1984**, *81*, 6159.
94. McConnell, H.; Watts, T.; Weis, R.; Brian, A., Supported planar membranes in studies of cell-cell recognition in the immune system. *Biochim Biophys Acta* **1986**, *864*, 95-106.
95. Merkel, R.; Sackmann, E.; Evans, E., Molecular friction and epitactic coupling between monolayers in supported bilayers. *J. Phys.* **1989**, *50*, 1535-1555.
96. Naumann, C. A.; Prucker, O.; Lehmann, T.; Rühle, J.; Knoll, W.; Frank, C. W., The polymer-supported phospholipid bilayer: tethering as a new approach to substrate-membrane stabilization. *Biomacromolecules* **2002**, *3*, 27-35.
97. Salafsky, J.; Groves, J. T.; Boxer, S. G., Architecture and function of membrane proteins in planar supported bilayers: a study with photosynthetic reaction centers. *Biochemistry* **1996**, *35*, 14773-14781.
98. Elender, G.; Kühner, M.; Sackmann, E., Functionalisation of Si/SiO<sub>2</sub> and glass surfaces with ultrathin dextran films and deposition of lipid bilayers. *Biosens. Bioelectron.* **1996**, *11*, 565-577.
99. Morigaki, K.; Baumgart, T.; Jonas, U.; Offenhäusser, A.; Knoll, W., Photopolymerization of diacetylene lipid bilayers and its application to the construction of micropatterned biomimetic membranes. *Langmuir* **2002**, *18*, 4082-4089.
100. Spinke, J.; Yang, J.; Wolf, H.; Liley, M.; Ringsdorf, H.; Knoll, W., Polymer-supported bilayer on a solid substrate. *Biophys. J.* **1992**, *63*, 1667.
101. Wong, J. Y.; Majewski, J.; Seitz, M.; Park, C. K.; Israelachvili, J. N.; Smith, G. S., Polymer-cushioned bilayers. I. A structural study of various preparation methods using neutron reflectometry. *Biophys. J.* **1999**, *77*, 1445-1457.
102. Campbell, N. A.; Reece, J. B., *Biology*. Benjamin Cummings; 7th edition: New York, **2004**.
103. Conner, S. D.; Schmid, S. L., Regulated portals of entry into the cell. *Nature* **2003**, *422*, 37-44.
104. Yang, J.; Chen, H.; Vlahov, I. R.; Cheng, J. X.; Low, P. S., Evaluation of disulfide reduction during receptor-mediated endocytosis by using FRET imaging. *Proc. Natl. Acad. Sci.* **2006**, *103*, 13872-13877.

105. Dausend, J.; Musyanovych, A.; Dass, M.; Walther, P.; Schrezenmeier, H.; Landfester, K.; Mailänder, V., Uptake mechanism of oppositely charged fluorescent nanoparticles in HeLa cells. *Macromol. Biosci.* **2008**, *8*, 1135-1143.
106. Mailänder, V.; Landfester, K., Interaction of nanoparticles with cells. *Biomacromolecules* **2009**, *10*, 2379-2400.
107. Lehninger, A. L.; Nelson, D. L.; Cox, M. M., *Principles of biochemistry*. WH Freeman & Co: **2005**; Vol. 1.
108. Mayor, S.; Pagano, R. E., Pathways of clathrin-independent endocytosis. *Nat. Rev. Mol. Cell Biol.* **2007**, *8*, 603-612.
109. Takei, K.; Haucke, V., Clathrin-mediated endocytosis: membrane factors pull the trigger. *Trends Cell Biol.* **2001**, *11*, 385-391.
110. Mousavi, S. A.; Malerød, L.; Berg, T.; Kjekken, R., Clathrin-dependent endocytosis. *Biochem. J* **2004**, *377*, 1.
111. Anderson, R. G. W., The caveolae membrane system. *Annu. Rev. Biochem* **1998**, *67*, 199-225.
112. Parton, R. G.; Simons, K., The multiple faces of caveolae. *Nat. Rev. Mol. Cell Biol.* **2007**, *8*, 185-194.
113. Deserno, M.; Gelbart, W. M., Adhesion and wrapping in colloid-vesicle complexes. *J. Phys. Chem. B* **2002**, *106*, 5543-5552.
114. Deserno, M.; Bickel, T., Wrapping of a spherical colloid by a fluid membrane. *Europhys. Lett.* **2003**, *62*, 767.
115. Jiang, W.; Kim, B. Y. S.; Rutka, J. T.; Chan, W. C. W., Nanoparticle-mediated cellular response is size-dependent. *Nature Nanotech.* **2008**, *3*, 145-150.
116. Chithrani, B. D.; Chan, W. C. W., Elucidating the mechanism of cellular uptake and removal of protein-coated gold nanoparticles of different sizes and shapes. *Nano Lett.* **2007**, *7*, 1542-1550.
117. Chithrani, B. D.; Ghazani, A. A.; Chan, W. C. W., Determining the size and shape dependence of gold nanoparticle uptake into mammalian cells. *Nano Lett.* **2006**, *6*, 662-668.
118. Lipowsky, R.; Döbereiner, H. G., Vesicles in contact with nanoparticles and colloids. *Europhys. Lett.* **1998**, *43*, 219.
119. Smith, K. A.; Jasnow, D.; Balazs, A. C., Designing synthetic vesicles that engulf nanoscopic particles. *J. Chem. Phys.* **2007**, *127*, 084703.
120. Yue, T.; Zhang, X., Cooperative Effect in Receptor-Mediated Endocytosis of Multiple Nanoparticles. *ACS nano* **2012**, *6*, 3196-3205.
121. Jin, H.; Heller, D. A.; Sharma, R.; Strano, M. S., Size-dependent cellular uptake and expulsion of single-walled carbon nanotubes: single particle tracking and a generic uptake model for nanoparticles. *ACS nano* **2009**, *3*, 149-158.
122. Andersson, P. O.; Lejon, C.; Ekstrand-Hammarström, B.; Akfur, C.; Ahlinder, L.; Bucht, A.; Österlund, L., Polymorph- and Size-Dependent Uptake and Toxicity of TiO<sub>2</sub> Nanoparticles in Living Lung Epithelial Cells. *Small* **2011**, *7*, 514-523.
123. Zhang, S.; Li, J.; Lykotrafitis, G.; Bao, G.; Suresh, S., Size-Dependent Endocytosis of Nanoparticles. *Adv. Mater.* **2009**, *21*, 419-424.
124. Fošnarič, M.; Iglič, A.; Kroll, D. M.; May, S., Monte Carlo simulations of complex formation between a mixed fluid vesicle and a charged colloid. *J. Chem. Phys.* **2009**, *131*, 105103.
125. Noguchi, H.; Takasu, M., Adhesion of nanoparticles to vesicles: a Brownian dynamics simulation. *Biophys. J.* **2002**, *83*, 299-308.

126. Teraoka, I., *Polymer solutions. An Introduction to Physical properties*. Wiley Online Library: **2002**.
127. Brown, W., *Dynamic light scattering: the method and some applications*. Oxford University Press, USA: **1993**.
128. Berne, B. J.; Pecora, R., *Dynamic light scattering: with applications to chemistry, biology, and physics*. Courier Dover Publications: **2000**.
129. Williams, G.; Watts, D. C., Non-symmetrical dielectric relaxation behaviour arising from a simple empirical decay function. *Trans. Faraday Soc.* **1970**, *66*, 80-85.
130. Esquenet, C.; Buhler, E., Aggregation behavior in semidilute rigid and semirigid polysaccharide solutions. *Macromolecules* **2002**, *35*, 3708-3716.
131. Provencher, S. W., CONTIN: a general purpose constrained regularization program for inverting noisy linear algebraic and integral equations. *Comput. Phys. Commun.* **2006**, *27*, 229-242.
132. Koppel, D. E., Analysis of macromolecular polydispersity in intensity correlation spectroscopy: the method of cumulants. *J. Chem. Phys.* **1972**, *57*, 4814.
133. Hallett, F.; Watton, J.; Krygsman, P., Vesicle sizing:: Number distributions by dynamic light scattering. *Biophys. J.* **1991**, *59*, 357-362.
134. Aragon, S.; Pecora, R., Theory of dynamic light scattering from polydisperse systems. *J. Chem. Phys.* **1976**, *64*, 2395.
135. Brown, J. C.; Pusey, P.; Dietz, R., Photon correlation study of polydisperse samples of polystyrene in cyclohexane. *J. Chem. Phys.* **1975**, *62*, 1136.
136. Berland, K. M. *Fluorescence Correlation Spectroscopy*, 2004.
137. Schwille, P.; Haustein, E., Fluorescence correlation spectroscopy An introduction to its concepts and applications. *Spectroscopy* **2009**, *94*, 1-33.
138. Rigler, R.; Elson, E., *Fluorescence correlation spectroscopy: theory and applications*. Springer Verlag: **2001**; Vol. 65.
139. Butt, H. J.; Kappl, M., *Surface and interfacial forces*. Wiley-VCH Verlag GmbH & Co. : **2010**.
140. Geisse, N. A., AFM and combined optical techniques. *Mater. Today* **2009**, *12*, 40-45.
141. Hinterdorfer, P.; Dufrêne, Y. F., Detection and localization of single molecular recognition events using atomic force microscopy. *Nat. Methods* **2006**, *3*, 347-355.
142. Williams, D. B.; Carter, C. B., *Transmission electron microscopy: a textbook for materials science*. Nova Iorque: Springer Science **2009**.
143. Hamley, I. W., *Block copolymers in solution: fundamentals and applications*. John Wiley & Sons Ltd, **2005**.
144. Won, Y. Y., Imaging nanostructured fluids using cryo-TEM. *Korean J. Chem. Eng.* **2004**, *21*, 296-302.
145. Bellare, J. R.; Davis, H.; Scriven, L.; Talmon, Y., Controlled environment vitrification system: an improved sample preparation technique. *Journal of electron microscopy technique* **1988**, *10*, 87-111.

## Chapter 4. Experimental Section

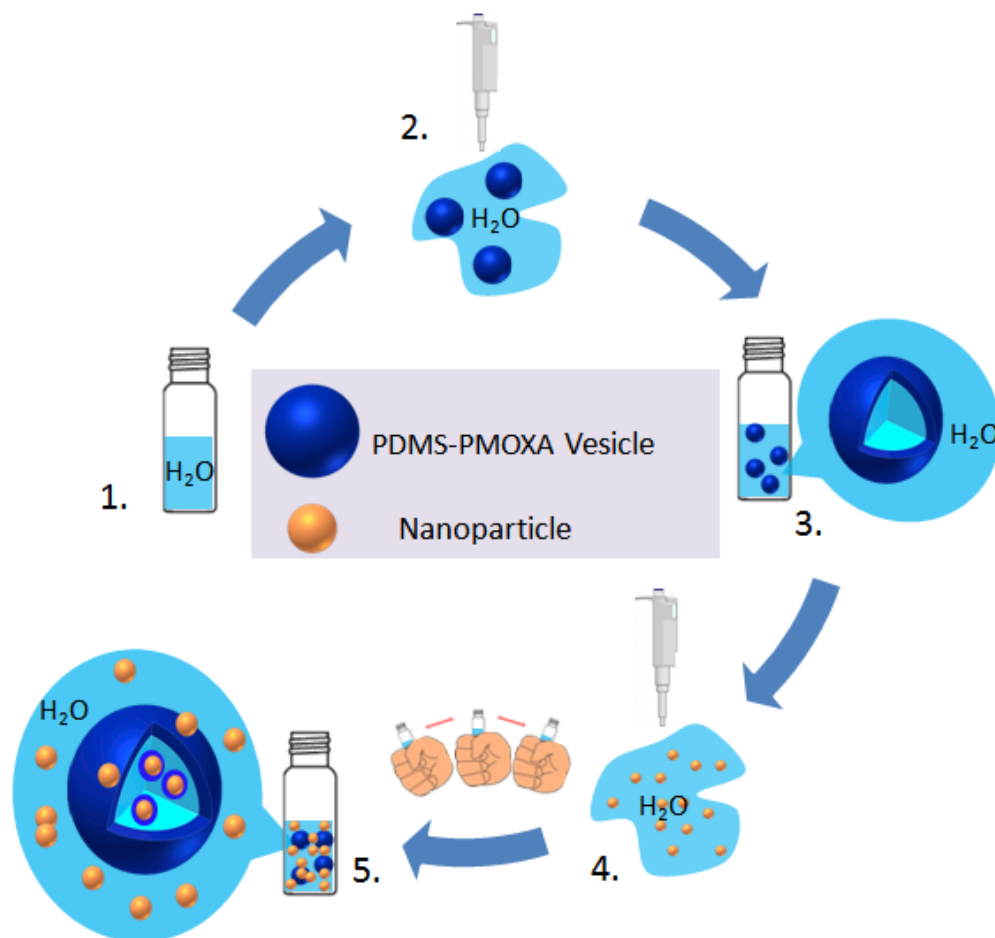


**Figure 4.1** Schematic picture representing preparation of polymersomes/nanoparticles mixture. **1.** desired amount of water is placed in a small glass vial; **2.** desired amount of polymersomes stock solution is added to the vial containing water; **3.** sample is let to equilibrate; **4.** desired amount of the stock solution of nanoparticles is added to the vial containing polymersomes; **5.** sample is gently shaken and let in order to equilibrate.

## 4.1 Materials

### 4.1.1 Block Copolymer Synthesis

#### 4.1.1.1 Poly(dimethylsiloxane)-*block*-poly(2-methyloxazoline) Synthesis

The poly(dimethylsiloxane)-*b*-poly(2-methyloxazoline) diblock copolymer (PDMS-*b*-PMOXA) was synthesized by Dr. Stefan Egli under the supervision of Prof. Dr. Wolfgang Meier at the University of Basel, Switzerland. The details of the synthesis and the characterization procedures are given in the literature.<sup>1</sup>

Poly(dimethylsiloxane)-*b*-poly(2-methyloxazoline) copolymer PDMS<sub>68</sub>-*b*-PMOXA<sub>11</sub>, where the numbers refer to the number-average degree of polymerization (see *Figure 4.2*), was synthesized by sequential ring-opening polymerization and has a polydispersity index PDI of 1.66, as determined by size exclusion chromatography (SEC) using polystyrene standards.<sup>1</sup> The molar mass was determined to be 6185 g mol<sup>-1</sup>. The polymer used for the purpose of this project has piperazyl functionality. The glass transition temperature determined by differential scanning calorimetry (DSC) is  $T_g = -124$  °C.

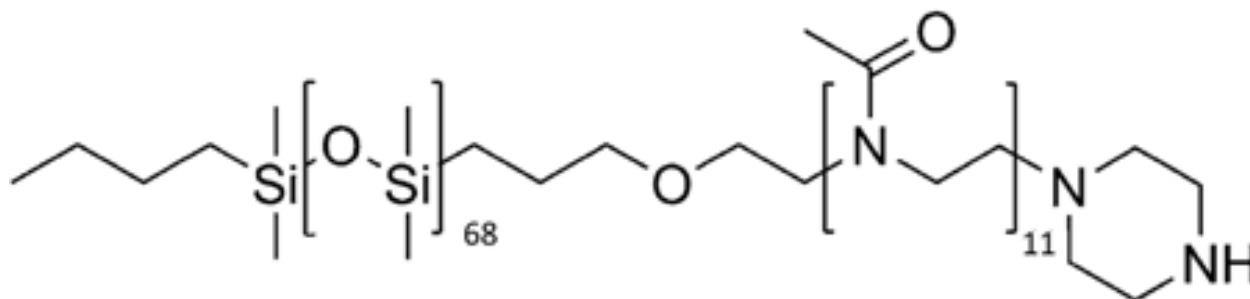


**Figure 4.2** Structure of piperazyl functionalized poly(dimethylsiloxane)-*b*-poly(2-methyloxazoline) copolymer.

### 4.1.1.2 Polystyrene-*b*-poly-(acrylic acid) Synthesis

The polystyrene-*b*-poly-(acrylic acid) diblock copolymer (PS-*b*-PAA) copolymer was synthesized by Dr. Tony Azzam from the group of Prof. Adi Eisenberg at McGill University Montreal, Canada. The details of the synthesis and the characterization procedures were given in the literature.<sup>2</sup>

Polystyrene-*b*-poly-(acrylic acid) copolymers PS<sub>307</sub>-*b*-PAA<sub>34</sub>, where the numbers refer to the number-average degree of polymerization (see *Figure 4.3*), was synthesized by sequential anionic polymerization.<sup>2</sup> This method allows the formation of a PS block of a fixed length with varying PAA blocks. Block copolymers prepared by anionic polymerization are well defined and have a low polydispersity index of PDI = 1.1 or even less.<sup>3</sup>

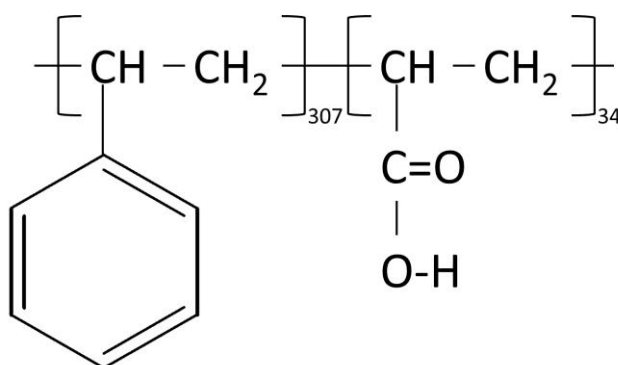


**Figure 4.3** Structure of polystyrene-*b*-poly-(acrylic acid) copolymer.

## 4.1.2 Polymersomes Preparation

### 4.1.2.1 PS-*b*-PAA Polymersomes Preparation

All polymersomes based on the PS-*b*-PAA copolymer were prepared using the solvent injection method.<sup>4</sup> Briefly, an appropriate amount of the copolymer solution in dioxane (p. a.  $\geq$  99.5%, Sigma Aldrich) was placed in a small vial. Under stirring condition (500 rpm) 30 wt% of

ultra-pure water (Millipore, Milli-Q water with a conductivity  $< 18.2 \text{ M}\Omega\cdot\text{cm}$ ) was added dropwise. This sample was stirred overnight and then diluted with Milli-Q water up to desired concentration. For light scattering experiments all samples were filtered with a  $5.0 \text{ }\mu\text{m}$  pore size syringe filter (Millipore LS).

#### 4.1.2.2 PDMS-*b*-PMOXA Polymersome Preparation

Polymersomes of PDMS-*b*-PMOXA, as schematically illustrated in *Figure 4.4*, were prepared using the film rehydration method followed by an extrusion process as described in the literature.<sup>5</sup> The diblock copolymer was placed in a small (10 ml) round bottom flask and dissolved in ethanol (p.a.  $\geq 99.5\%$ , Sigma Aldrich). Ethanol was evaporated using a rotary evaporator under reduced pressure at a temperature of  $T = 40 \text{ }^\circ\text{C}$ . The final thin polymer film formed on the wall of the flask was dried under vacuum for 1 h at room temperature. Ultrapure water (Millipore, Milli-Q water with a conductivity  $< 18.2 \text{ M}\Omega\cdot\text{cm}$ ) was added and the sample was stirred overnight using a magnetic stirrer (350 rpm). Subsequently, the resulting polymersome suspension was extruded (LiposoFast™ Basic Extruder, Avestin, Ottawa, Canada) 11 times through a polycarbonate membrane of  $0.8 \text{ }\mu\text{m}$  pore size, 11 times through a polycarbonate membrane of  $0.4 \text{ }\mu\text{m}$  pore size and 11 times through a polycarbonate membrane of  $0.2 \text{ }\mu\text{m}$  (Avestin), to homogenize the final vesicle size.

The Nile Blue (Acros Organics) labeling of polymersomes was achieved by the addition of the dye solution in ethanol ( $60 \text{ }\mu\text{M}$ ) to the initial copolymer/ethanol solution.

For the light scattering measurements four concentrations of polymersomes dispersions were prepared via dilution of the stock solution ( $c_1$ ), resulting in  $c_2 = 0.5 c_1$ ,  $c_3 = 0.1 c_1$ ,  $c_4 = 0.05 c_1$  and  $c_5 = 0.01 c_1$ . The concentration of the stock solution is estimated to be  $0.7 \text{ gL}^{-1}$ . The refractive index increment for the PDMS-*b*-PMOXA vesicles in water was estimated to be in the

range of the value measured for PMOXA-*b*-PDMS-*b*-PMOXA triblock copolymer of 0.188 mL/g.<sup>6</sup>

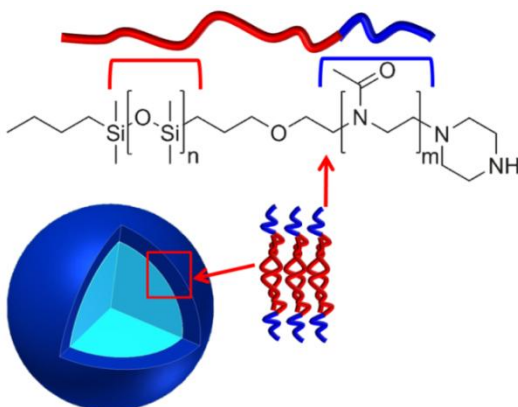


**Figure 4.4** Schematic representation of a PDMS-*b*-PMOXA polymersome with the shell built from hydrophobic PDMS (red) and hydrophilic PMOXA (blue).

### 4.1.3 Fluorescent Polystyrene Nanoparticles

#### 4.1.3.1 Fluorescent Polystyrene Nanoparticles Synthesis

The polystyrene nanoparticle (PS NP) synthesis (with  $R_{h\ NP} = 16\text{ nm}$ ) was performed by Dr. Umaporn Paiphansiri at the Max Planck Institute for Polymer Research, Mainz, Germany (MPIP).

**Chemicals:** Styrene (Merck) was purified by passing the monomer through a  $\text{Al}_2\text{O}_3$  column and stored below  $0\text{ }^\circ\text{C}$ . Hexadecane (Merck), sodium dodecyl sulfonate (SDS; Fluka), potassium persulfate (KPS; Acrös), a fluorescent marker N-(2,6-diisopropylphenyl)-perylene-3,4-dicarbonacidimide (PMI; BASF) were applied without further purification.

**Synthesis:** The organic dispersed phase including 6 g of the styrene monomer, 250 mg of hexadecane and 4 mg of PMI was firstly prepared. The oil-in-water macroemulsion was then

obtained by mixing the organic phase into an aqueous phase (24 g of water and 2 g of SDS) under 1 hour of vigorous stirring. To prepare the miniemulsion, the macroemulsion was subjected to ultrasonication at 90% amplitude using a Branson sonifier W-450 D (1/2'' tip) under ice cooling for 2 min. The miniemulsion polymerization was conducted by adding the dissolved initiator solution (100 mg of KPS) and the reaction proceeded overnight at 72 °C.

#### 4.1.3.2 Fluorescent Polystyrene Nanoparticles Preparation

After synthesis nanoparticles were dialyzed against water for a period of 2 weeks to ensure complete removal of the surfactant. The concentration of the stock solution was determined to be 50 gL<sup>-1</sup>. Nanoparticles were then diluted with water containing nonionic surfactant Lutensol AT-50 (surfactant concentration: 6 gL<sup>-1</sup>) down to 25 gL<sup>-1</sup>. Lutensol AT-50 has the following formula: RO(CH<sub>2</sub>CH<sub>2</sub>O)<sub>50</sub>H, where R states for linear, saturated C<sub>16</sub>C<sub>18</sub> fatty alcohol.

#### 4.1.4 SiO<sub>2</sub> Nanoparticles

Silica nanoparticles (SiO<sub>2</sub> NPs) with  $R_{h,NP} = 14$  nm, 25 nm, 36 nm and 57 nm respectively were ordered from Kisker Biotech GmbH & Co, Germany and used as received or eventually filtered with syringe filters (Millipore LCR 0.45 μm pore size) in order to eliminate possible agglomerates.

#### 4.1.5 Polymersome/Nanoparticle Mixture Preparation

All mixtures of polymersomes and nanoparticles (polymersomes/NPs) were prepared according to the same procedure schematically shown in *Figure 4.1*: mainly, the dispersion of the desired polymersome concentration ( $c_p$ ) was placed in a small glass vial and a chosen amount of nanoparticles (NPs) was added afterwards. Samples were gently shaken or stirred and stored at least 1 hour prior the measurement.

Samples for size dependent NPs incorporation experiments were prepared one day prior the measurement by the addition of SiO<sub>2</sub> NPs of the desired size to the dilute aqueous vesicle suspensions ( $c_P = 4.5 \cdot 10^{-2} \text{ gL}^{-1}$ ). Samples with different nanoparticle concentrations ( $c_{\text{NP}} = 0.05, 0.1, 0.15$  and  $0.2 \text{ gL}^{-1}$ ) were prepared according to the same procedure by varying the final  $c_{\text{NP}}$  in the mixture.

For kinetic measurements, a dispersion of the desired  $c_P$  was placed directly in a LS (for PCS measurements, Hellma) or FCS (an eight-well polystyrene chambered coverglass, Laboratory-Tek, Nalge Nunc International) cuvette. Nanoparticles of desired concentrations were injected using a micropipette and the sample was gently shaken. Measurements were performed directly and time dependent.

## 4.2 Instrumentation

### 4.2.1 Photon Correlation Spectroscopy (PCS) Measurements

Static (SLS) and dynamic (DLS) light scattering experiments were performed on a commercially available instrument from ALV GmbH consisting of a goniometer and an ALV-5000 or ALV-5004 multiple-tau full-digital correlator (320 channels), which allows measurements over a time range of  $10^{-7} \leq t \leq 10^3$  s and an angular range from  $20^\circ$  to  $150^\circ$  corresponding to a scattering vector  $q = 4.8 \times 10^{-3} - 2.6 \times 10^{-2} \text{ nm}^{-1}$ . A He-Ne laser (Uniphase with a single mode intensity of 25 mW operating at a laser wavelength of  $\lambda_0 = 632.8 \text{ nm}$ ) or a Nd:Yag-laser (Coherent Compass215M-75, 75mW,  $\lambda_0 = 532 \text{ nm}$ ) was used as light source. An avalanche photodiode was used as detector. All measurements were carried out at a temperature  $T = 20^\circ \text{C}$ . Dust-free dispersions for the experiments were obtained by filtration through PTFE membrane filters with a pore size of  $5 \mu\text{m}$  (Millipore LS syringe filters) directly into cylindrical silica glass cuvettes (Hellma, inner diameter  $\varnothing = 10$  or  $20 \text{ mm}$ ), which had been cleaned before with acetone in a Thurmont-apparatus.

Data evaluation for the DLS experiments (see 3.6.1.1.1) were performed by using both, the stretched exponential Kohlrausch-Williams-Watts (KWW) function (for polymersomes/SiO<sub>2</sub> NPs with different diameters) or CONTIN (for polymersomes/PS  $R_{\text{h NPs}} = 16\text{nm}$  and polymersomes/SiO<sub>2</sub>  $R_{\text{h NPs}} = 14\text{nm}$ ). The CUMULANT method was used only for comparison of the influence of different fitting methods (characterization of empty polymersomes).

### 4.2.2 Fluorescence Correlation Spectroscopy (FCS) Measurements

**Polymersomes/Fluorescent Polystyrene Nanoparticles:** FCS experiments were performed using a commercial setup (Zeiss, Germany) consisting of the module ConfoCor2 and an inverted microscope model Axiovert 200 with a Zeiss C-Apochromat 40x/1.2 W water immersion

objective. The fluorophores were excited by an argon laser ( $\lambda_0 = 488$  nm) and the emission was collected after filtering with a LP505 long pass filter. For detection, an avalanche photodiode that enables single-photon counting was used. An eight-well polystyrene chambered coverglass (Laboratory-Tek, Nalge Nunc International) was used as sample cell. The kinetic measurements were performed for a period of 120 min starting immediately after adding the PS NPs to the vesicle solution in the FCS chamber. The size of the observation volume  $V$  depends strongly on the specific characteristics of the optical setup, a calibration was performed using a reference standard with known diffusion coefficient, *i.e.* Alexa Fluor 488. In the cases where only one type of diffusing species were observed ( $\gamma = 1$ ) their average fluorescent brightness<sup>7</sup> was evaluated by dividing the average fluorescent intensity to the average number of diffusing species ( $N$ ) in the observation volume.

**Polymersomes/Fluorescent Silica Nanoparticles:** the experiments were performed on a semi commercial setup based on an inverted microscope IX70 (Olympus, Japan) combined with the FluoView300 confocal laser scanning unit (Olympus, Japan) and an FCS upgrade kit (PicoQuant, Germany). The latter is fiber coupled to the FluoView300 and has two detection channels separated by a dichroic mirror and possessing separate emission filters and single photon avalanche diode ( $\tau$ -SPAD) detectors (PicoQuant, Germany). A TimeHarp 200 time-correlated single-photon counting card in combination with the software package SymPhoTime (both PicoQuant, Germany) is used for data acquisition and analysis. An Olympus UPLSAPO 60XW, 60 $\times$  / NA 1.2 water immersion objective was used in all studies. The fluorescently labeled silica nanoparticles were excited by an argon-ion laser at  $\lambda_0 = 488$  nm and their emission was detected after filtering with a BP525/50 band pass filter. The Nile Blue labeled polymersomes were excited by a helium-neon laser at  $\lambda_0 = 633$  nm and the emission was detected after filtering through a LP635R long-pass filter. An eight-well, polystyrene-chambered cover glass

(Laboratory-Tek, Nalge Nunc International) was used as sample cell. For each sample a series of 10 measurements with a total duration 5 min were performed. The fluctuations of the fluorescence intensity  $F(t)$  caused by the diffusion of the silica nanoparticles or the polymersomes through the confocal detection volume were separately monitored in the respective detection channels and evaluated in terms of an autocorrelation function  $G(t) = \langle F(t')F(t+t') \rangle / \langle F(t') \rangle^2$ .

The size of the observation volume  $V$  depends strongly on the specific characteristics of the optical setup and the refractive index of the studied samples a suitable calibration, relying on the measurement of the characteristic diffusion time of a fluorescent tracer with known diffusion coefficient, is needed. Here Alexa Fluor 488 and Alexa Fluor 647 (Invitrogen) were used for calibration of the two detection channels, respectively.

### 4.2.3 Atomic Force Microscopy (AFM) Measurements

A Veeco Multimode AFM with a Nanoscope III controller (Bruker AXS, Santa Barbara, CA) equipped with standard tapping mode liquid cell was used to perform the topographic imaging of vesicles adsorbed on silicon wafers and mechanical testing of vesicles (pictures of the AFM setup and the liquid cell can be seen in *Figure 4.5*). Characterization of vesicles adsorbed on mica was carried out with a Nanowizard 3 AFM with QI mode and liquid cell (JPK Instruments, Berlin). NP type A cantilevers (Bruker AXS AFM Probes) with a resonance frequency of  $8 \pm 2$  kHz (in aqueous solution) and an average spring constant of  $k_c = 0.33 \pm 0.03$  N/m (as determined by the thermal tune method)<sup>8</sup> were used. Small pieces ( $10 \times 10$  mm) of silicon wafers or freshly cleaved muscovite mica were used as substrate.

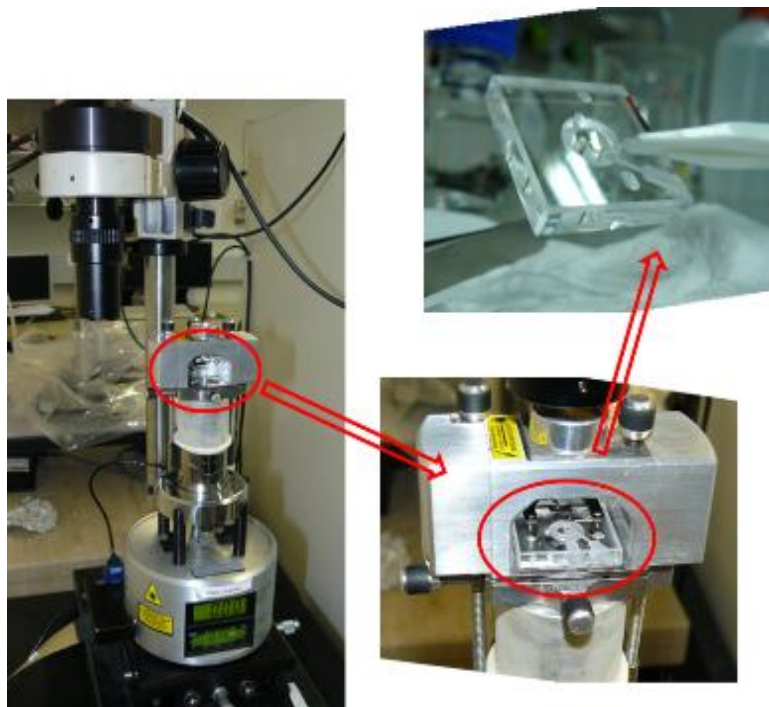


**Figure 4.5** Atomic force microscopy setup with specially designed “liquid cell” to perform measurement in aqueous solution.

Silicon wafers were cleaned by sonication in acetone, ethanol, and MilliQ water, followed by plasma treatment for 1 min. A stock polymersome solution ( $c_p = 0.7 \text{ gL}^{-1}$ ) was diluted with Milli-Q water down to  $0.1 \text{ gL}^{-1}$  in order to avoid vesicle aggregation at the surface. The total amount of  $30 \text{ }\mu\text{L}$  of the dilute solution was injected using a micropipette into the liquid cell. The solution was placed in the liquid cell two hours prior the measurement. This practice allows polymersomes to adsorb on the surface and to minimize drift of the instrument. Vesicles in solution were imaged using tapping mode which minimizes shear forces acting on the sample and thus avoids dislocation of the vesicles by the tip.<sup>9</sup>

Once a polymersome was identified, the AFM tip was located above the crest of the vesicle and at least 10 - 30 cantilever deflection *vs.* piezo position curves were recorded to probe the mechanical properties of the vesicles using defined loads in the range of 1 - 20 nN. To

calibrate the deflection sensitivity of the AFM, i.e. the conversion factor between detector signal in volts and cantilever deflection in nanometers, cantilever deflection vs. piezo position curves were recorded on the hard silicon substrate as a reference. After subtracting the voltage offset obtained from fitting the zero force baseline, the deflection voltage signal of each curve is converted to force by dividing it by the deflection sensitivity and by multiplying it with the spring constant of the cantilever. The distance is obtained by subtracting the cantilever deflection from the piezo position.<sup>10</sup> This conversion procedure was automatized using self-written software. After the force measurements, each vesicle was imaged again in tapping mode to verify its intactness.

#### **4.2.4 Transmission Electron Microscopy (TEM) Measurements**

A Tecnai F20 transmission electron microscope from FEI Co. operated at a 200 kV acceleration voltage was used for recording of the cryo-TEM images of the specimens. For cryofixation of the samples, the aqueous solution was dropped onto a quantifoil (R) holey carbon coated grid. The excess amount of liquid was blotted off with filter paper. Subsequently, the sample was frozen in liquid ethane at  $T = -178$  °C and transferred to the TEM instrument. Statistical analyses of TEM micrographs to characterize the size and the membrane thickness of the polymersomes were performed by using the software program ImageJ 1.37a. The number of objects counted was in the range of 80 – 200.

#### **4.2.5 Zeta - Potential Measurements**

The Zeta-potentials of nanoparticles as well as polymersomes in aqueous solutions were determined by MALVERN Zetasizer Nano Z.

## 4.3 References

1. Egli, S.; Nussbaumer, M. G.; Balasubramanian, V.; Chami, M.; Bruns, N.; Palivan, C.; Meier, W., Biocompatible Functionalization of Polymersome Surfaces: A New Approach to Surface Immobilization and Cell Targeting Using Polymersomes. *J. Am. Chem. Soc.* **2011**, *133*, 4476–4483.
2. Zhong, X. F.; Varshney, S. K.; Eisenberg, A., Critical micelle lengths for ionic blocks in solutions of polystyrene-*b*-poly (sodium acrylate) ionomers. *Macromolecules* **1992**, *25*, 7160-7167.
3. Azzam, T.; Eisenberg, A., Control of vesicular morphologies through hydrophobic block length. *Angew. Chem. Int. Ed.* **2006**, *45*, 7443-7447.
4. Yu, K.; Eisenberg, A., Bilayer morphologies of self-assembled crew-cut aggregates of amphiphilic PS-*b*-PEO diblock copolymers in solution. *Macromolecules* **1998**, *31*, 3509-3518.
5. Olson, F.; Hunt, C.; Szoka, F.; Vail, W.; Papahadjopoulos, D., Preparation of liposomes of defined size distribution by extrusion through polycarbonate membranes. *BBA-Biomembranes* **1979**, *557*, 9-23.
6. Nardin, C.; Hirt, T.; Leukel, J.; Meier, W., Polymerized ABA triblock copolymer vesicles. *Langmuir* **2000**, *16*, 1035-1041.
7. Rigler, R.; Elson, E., *Fluorescence correlation spectroscopy: theory and applications*. Springer Verlag: **2001**; Vol. 65.
8. Hutter, J. L.; Bechhoefer, J., Calibration of atomic-force microscope tips. *Rev. Sci. Instrum.* **1993**, *64*, 1868-1873.
9. Legleiter, J.; Kowalewski, T., Tapping, pulling, probing: atomic force microscopy in drug discovery. *Drug Discovery Today* **2004**, *1*, 163-169.
10. Butt, H. J.; Cappella, B.; Kappl, M., Force measurements with the atomic force microscope: Technique, interpretation and applications. *Surf. Sci. Rep.* **2005**, *59*, 1-152.

## Chapter 5. Results and Discussion

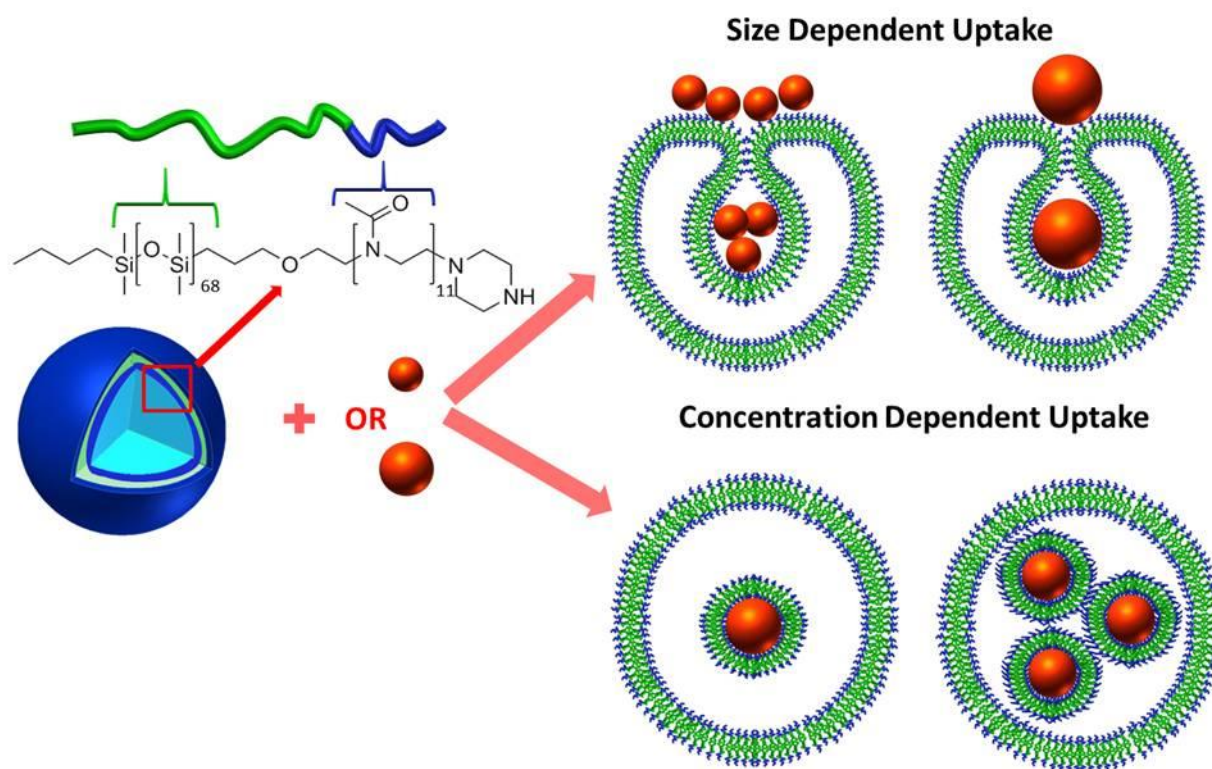


**Figure 5.1** Schematic representation of size and concentration dependent uptake of SiO<sub>2</sub> nanoparticles by PDMS-*b*-PMOXA polymersomes.

## Outline

To achieve the goal of this thesis four major steps were taken. First the proper system was selected and in the second step fully characterized. In the third step the characterization methods were optimized in order to utilize them for depiction of the chosen model system. Finally the parameters of the system were varied and response to these changes described.

**Design of The Model System:** The first step included on the one hand the selection of the proper material to produce artificial membranes and on the other hand the selection of colloidal nanoparticles. Requirements for the model membrane were long-term stability along with the suitable fluidity and flexibility. The assumption that the membrane forming material needs to possess a low glass transition temperature leads to the proper block copolymer selection. The requirements for the nanoparticles are the variety of sizes available while keeping all other properties constant. Furthermore, nanoparticle with different surface chemistry should be selected to vary the potential adhesion to the membrane. Experimental methodology leading to complex system description is presented.

**Characterization of Polymersomes and Colloidal Nanoparticles:** To ensure membrane flexibility, detailed atomic force microscopy (AFM) and force spectroscopy measurements were conducted. The characterization of nanoparticles ensuring their stability and lack of agglomeration tendency is performed.

**Probing Incorporation of Nanoparticles into Polymersomes:** In this section the model system based on polymersomes and colloidal nanoparticles of fixed size and concentration is established. The nanoparticles incorporation by polymersomes via endocytic-like mechanisms is reported. Detailed characterization methods based on the combination of photon correlation spectroscopy (PCS) and fluorescence correlation spectroscopy (FCS) are described.

**Incorporation of Silica Nanoparticles into Polymersomes: Size and Concentration Effects:**

In this part utilizing the above mentioned model and techniques both size and concentration of nanoparticles were varied. Size and concentration dependent uptake, characteristic for living cells, is also reported for synthetic polymersomes. Conditions which need to be met in order to ensure nanoparticle uptake and controlled filling of polymersomes are presented.

## 5.1 Designing of the Model System

The strategy for the development of an uptake model system for nanoparticles is presented in this part. The motivation for the decision for the utilization of a block-copolymer over a lipid to design a novel artificial model membrane system is described; the choice of a specific block copolymer is explained with respect to its mechanical properties. Furthermore, a brief description of colloidal particles as constituents of the developed model system is made. Finally the development of proper characterization methods and the combination of different techniques with emphasis of their application to probe nanoparticles uptake is discussed.

### 5.1.1 Selection of Vesicle Forming Block Copolymers

Amphiphilic block copolymers are able to self-assemble in water into bilayers which enclose a portion of the aqueous phase in their interior (see 3.1).<sup>1</sup> Such structures, known as polymersomes or polymeric vesicles, are analogous to liposomes which are formed spontaneously when certain phospholipids are dispersed in water. From a biophysical point of view such thermodynamically driven self-organized supramolecular structures can be considered as promising model systems to mimic bio-membranes.<sup>2</sup> The closed bilayer of these objects is a fundamental architectural requirement towards compartmentalization. Nevertheless, most of the functional requirements of bio-membranes, for instance membrane fusion and fission, vesicle budding and transmembrane transport, are related to mechanical properties<sup>3, 4</sup> such as stability and rigidity as well as elasticity and deformability. On one hand, the low molecular weight of lipid components ensures the needed fluidity and other “soft” mechanical properties, which are required for such processes. On the other hand, the stability of liposomes has been a concern owing to the high mobility of their constructional units. Therefore, many efforts have been made to stabilize these structures by cross-linking or by adding of polymeric additives.<sup>5-8</sup>

The major advantage of block copolymer vesicles over liposomes is their increased stability and the rigidity of their membranes, which contribute to their increased lifetime. Polymersomes can be either thermodynamic equilibrium structures with a moderate exchange rate of polymer chains between aggregates or, more interesting for model systems, “frozen” structures, which means the chains are kinetically trapped and the exchange is very slow compared to experimental time scales.<sup>9</sup> Furthermore, the limited chemical stability of liposomes caused by oxidation processes of unsaturated fatty acids and the hydrolysis of ester bonds<sup>10</sup> can be significantly improved by using block copolymers. In addition, polymersomes are tunable in a wide range. The large number of available monomers and the ability to vary the molecular mass and the ratio of

the constitutive blocks makes it possible to tune the properties of the resulting nanostructures, for example, dimension, shape, solubility, and membrane thickness.<sup>11-17</sup>

The requirements for the designed model system are long-term stability along with suitable fluidity and flexibility of the artificial membrane and a low polydispersity of the used components. The assumption that the membrane forming material needs to possess on one hand a low glass transition temperature to achieve the needed fluidity and on the other hand a low mobility of the constructional units to implement the necessary stability, leads to a proper diblock copolymer. Diblock copolymers self-assemble into bilayer structures which are similar to lipid bilayers and thus, the architecture is comparable.

For the purpose of this project, numbers of different amphiphilic diblock copolymers were investigated; just to name a few of them: polystyrene-*b*-poly(acrylic acid) (PS-*b*-PAA), polystyrene-*b*-poly(ethylene oxide) (PS-*b*-PEO), polybutadiene-*b*-poly(ethylene oxide) (PB-*b*-PEO), poly( $\gamma$ -methyl- $\epsilon$ -caprolactone)-*b*-poly(acrylic acid) (PMCL-*b*-PAA) and poly(dimethylsiloxane)-*b*-poly(2-methyloxazoline) (PDMS-*b*-PMOXA). In this chapter two block copolymers with an extreme different  $T_g$ , mainly PS-*b*-PAA ( $T_g \sim 100$  °C) and PDMS-*b*-PMOXA ( $T_g = -124$  °C) are described with focus on their potential application as a model membrane.

#### 5.1.1.1. Polystyrene-*b*-poly(acrylic acid) (PS-*b*-PAA) Copolymer

Most often characterized in the literature are polystyrene-*b*-poly(acrylic acid) (PS-*b*-PAA) polymersomes.<sup>1, 9, 18</sup> Despite of their excellent mechanical stability they cannot be utilized as a model membrane system. Here the potential application as a negative model was considered. Due to the glassy core consisting of polystyrene ( $T_g \sim 100$  °C) their membrane is relatively rigid<sup>18</sup> in contrast to the fluidic character of biological membranes. Despite of this fact PS-*b*-PAA

polymersomes were still considered to study the influence of the membrane rigidity on the nanoparticle absorption (negative model). Furthermore, PS-*b*-PAA polymersomes could be ideal candidates to study the curvature-mediated adhesion of nanoparticles at the outer surfaces of the polymersomes.

Polymersomes composed of PS-*b*-PAA were prepared by the solvent - injection method.<sup>19</sup> The size of the resulting polymersomes prepared by this technique depends on the initial polymer concentration,<sup>20</sup> the stirring conditions and the dropping speed. *Figure 5.2* shows the increase of the final aggregate size while increasing the initial copolymer concentration in dioxane solutions. Due to this behavior a well-directed production of polymersomes with defined hydrodynamic radii  $R_h$  are possible, which is of importance in terms of requirements on a model system.

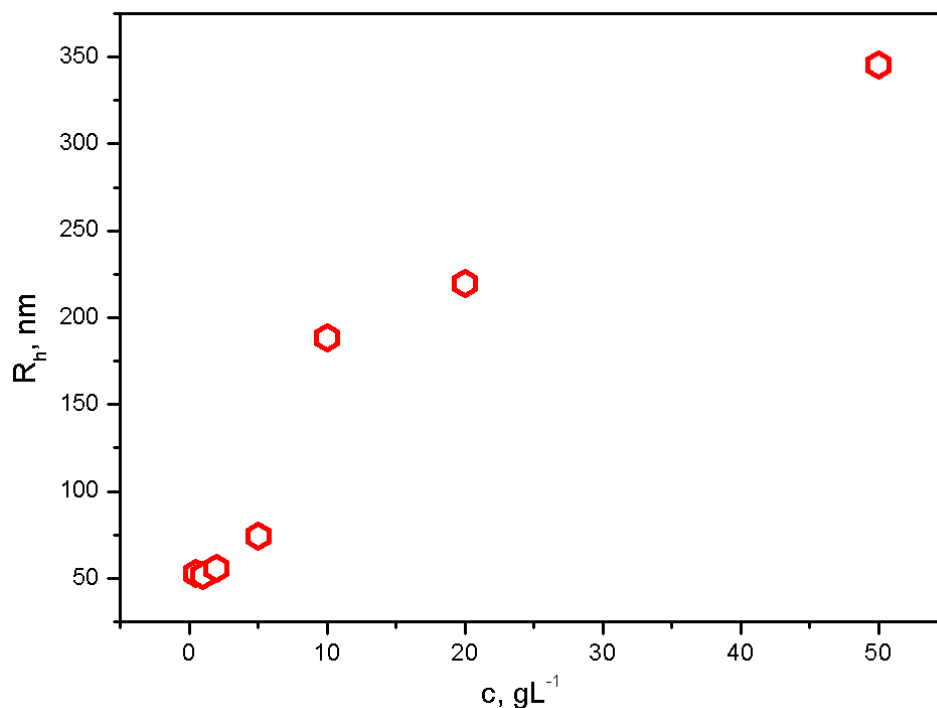


**Figure 5.2** Size of PS<sub>307</sub>-*b*-PAA<sub>34</sub> polymersomes as a function of initial copolymer concentration in dioxane.

However, due to technical conditions the stirring parameters and dropping speed, which influence the polydispersity of the formed aggregates, are not well-defined. Furthermore, the final polydispersity and size of the aggregates cannot be tuned once polymersomes are formed which is another limiting factor. Therefore, the resulting system polydispersity failed the requirements. As already mentioned, spectroscopic techniques which can provide many detailed information about the nanoparticle uptake mechanisms, require a relatively low polydispersity of both polymersomes as well as nanoparticles (*vide supra*).

As can be seen on *Figure 5.3* the polydispersity of PS<sub>307</sub>-*b*-PAA<sub>34</sub> polymersomes is quite high. Moreover, structures other than regular polymersomes are present. Furthermore, several pictures, both scanning and transmission electron microscopy (SEM and TEM, respectively) revealed the presence of perforated structures (see *Figure 5.4*).

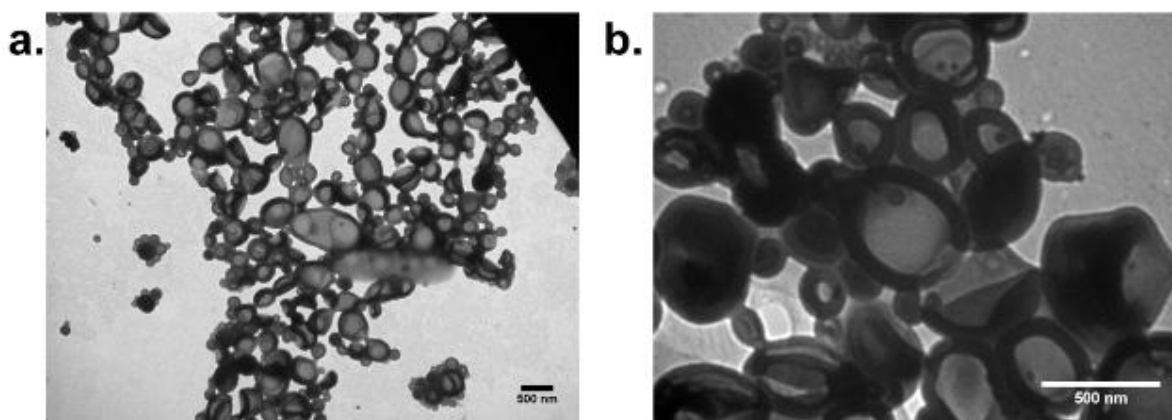


**Figure 5.3** Transmission Electron Microscopy (TEM) pictures of PS<sub>307</sub>-*b*-PAA<sub>34</sub> polymersomes a. in absence and b. presence of gold nanoparticles.

Preliminary studies of gold nanoparticles ( $R_h = 20$  nm) interactions with PS<sub>307</sub>-*b*-PAA<sub>34</sub> polymersomes revealed very weak interactions of these nanoparticles with polymersomes. As can

be seen in *Figure 5.4d* gold nanoparticles remain on the surface of vesicles but probably only because of the drying process during which they get into contact with vesicles.

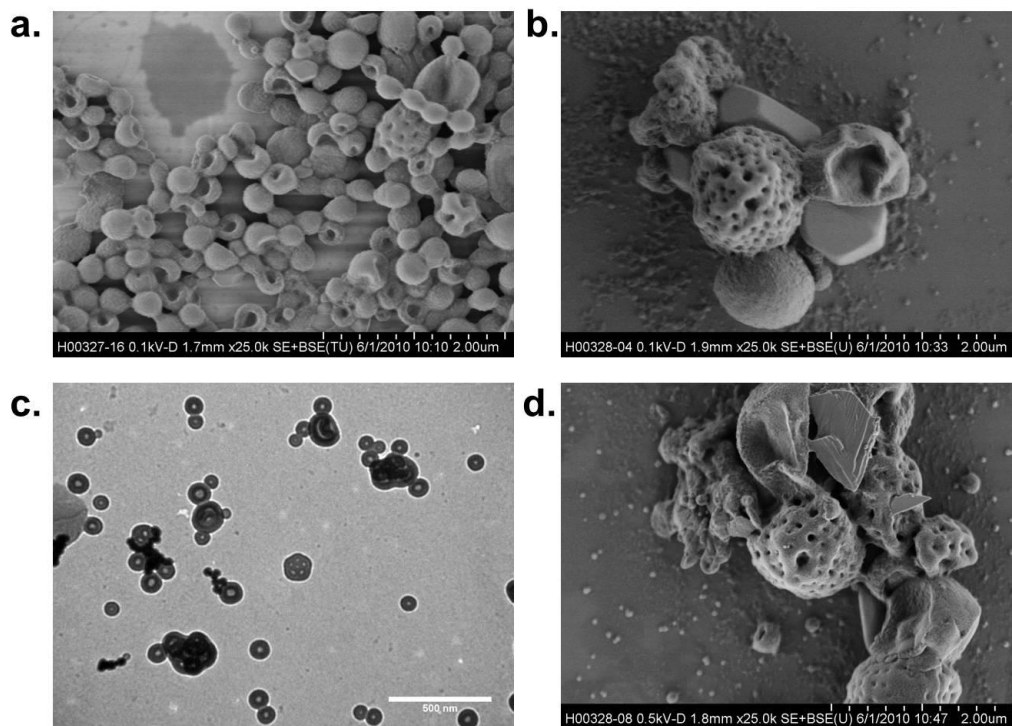


**Figure 5.4** Micrographs of PS<sub>307</sub>-*b*-PAA<sub>34</sub> polymersomes; **a,b.** SEM images; **c.** TEM image with perforated structure marked with arrow; **d.** SEM in presence of colloidal gold nanoparticles (gold nanoparticles on the top of the vesicle marked with arrow).

Weak adhesive interaction between negatively charged gold nanoparticles and negatively charged polymersomes do not favor nanoparticles adhesion to the polymersomes surface. The energy barrier facilitated by the weak adhesive interactions on the one hand and high bending modulus on the other hand cannot be overcome in this case.

The PS-*b*-PAA vesicles even though already well-established could not be applied up to now as proper model system. High polydispersity assisted by the structure inhomogeneity exclude even a potential application as a negative model.

### 5.1.1.2. Poly(dimethylsiloxane)-*block*-poly(2-methyloxazoline) Copolymer

Poly(dimethylsiloxane)-*b*-poly(2-methyloxazoline) (PMDS-*b*-PMOXA) polymersomes are promising candidates for serving as a model system of biomembranes. Due to the much lower glass transition temperature of PMDS-*b*-PMOXA ( $T_{g \text{ PDMS}} = -124 \text{ }^{\circ}\text{C}$ ), these polymersomes can be expected to be much more flexible and thus closer mimic the dynamic mechanical response of biological membranes.<sup>21</sup>

PDMS-*b*-PMOXA polymersomes exhibit an about 5 - 7 times higher value of the bending modulus compared to gel-like lipids (see Chapter 5.2.1).<sup>22</sup> This higher bending modulus stems from the higher thickness of the bilayer of PMDS-*b*-PMOXA polymersomes (~16 nm) compared to natural lipids (~5 nm), while the Young's modulus is even lower than for the gel-like lipids. In comparison to other polymersomes like those based on (PS-*b*-PAA),<sup>18</sup> the PDMS-*b*-PMOXA polymersomes are by one order of magnitude more flexible (in terms of the value of the bending modulus). This matches the expectation that by using a block copolymer with low  $T_g$  it should be able to prepare polymersomes with an optimal balance between mechanical stability on one hand and a bending rigidity that is more close to that of natural membrane on the other hand. This delicate balance of properties is also reflected in the different adsorption behavior on silica and mica. While the PDMS-*b*-PMOXA polymersomes appeared completely stable when adsorbed onto silica and could withstand load forces of up to 20 nN, they had a clear tendency to rupture and fuse on the mica surface. The combination of sufficient mechanical stability on one hand and sensitivity to external stimuli on the other hand makes PDMS-*b*-PMOXA polymersomes promising candidates for biomedical applications. Furthermore, in spite of the structural differences to lipid bilayers, which are often used as model membranes, PDMS-*b*-PMOXA polymersomes have been proven to exhibit functional properties of natural membranes as transmembrane transport and functional integration of membrane proteins. Furthermore, these

kind of polymersomes can be used as model membranes, *e.g.* as a bridging platform to study physical and physico-chemical aspects of transmembrane transport mechanisms of nanoparticles.<sup>21, 23</sup>

Complex characterization of PDMS-*b*-PMOXA polymersomes is described in Chapter 5.2.1.

### 5.1.1 Nanoparticles Selection

Requirements for the nanoparticles used in the designed model system are long term stability, low polydispersity, and possibility of fluorescent labeling. Nanoparticles should be available in different sizes by keeping the same surface chemistry. Based on the surface chemistry of the selected PDMS-*b*-PMOXA polymersomes with piperazyl groups at the outer surface (Zeta-potential  $\sim +30$  mV, see 5.2) it is desired that the surface charge of particles is opposite and the surface compatible in order to promote adhesive interaction between these two species (see *Figure 5.5*).

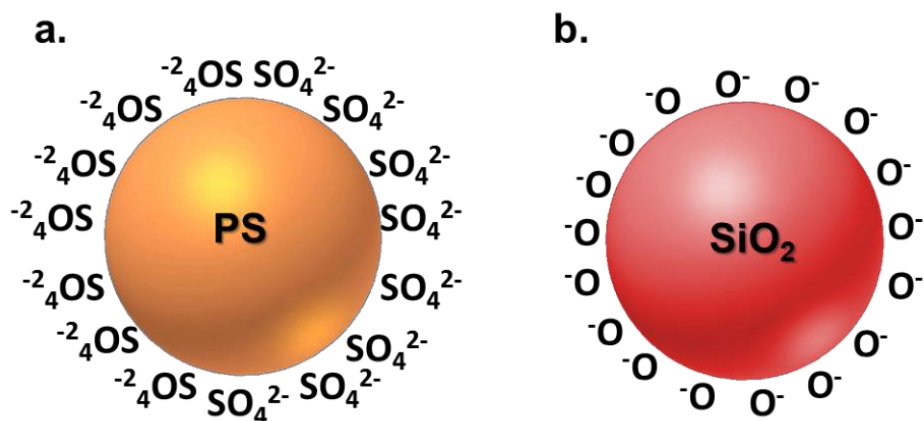


**Figure 5.5** Schematic representation of the surface chemistry of two selected nanoparticles; **a.** Polystyrene nanoparticle, **b.** SiO<sub>2</sub> nanoparticle.

Fluorescently labeled polystyrene nanoparticles (PS NPs) which could be prepared with different sizes by keeping the surface chemistry as well as with different surface chemistries were selected. Long term stability and low polydispersity make them perfect candidates for this purpose. For details of the PS NP characterization see 5.2.2.

Stable, fluorescently labeled SiO<sub>2</sub> nanoparticles (SiO<sub>2</sub> NPs) available in many sizes and with a different surface chemistry in comparison to PS NPs were selected as second type of particles. The refractive index of the used particles was an important parameter and for this reason particles with a refractive index significant higher than that of water and the bilayer forming block copolymer were chosen. The refractive index was found to be  $n_{\text{PS}} = 1.59$  and  $n_{\text{SiO}_2} = 1.46$ , whereas the refractive index of water is  $n_{\text{H}_2\text{O}} = 1.333$  and for the PDMS-*b*-PMOXA copolymer a value of  $n_{\text{P}} = 1.4$  was determined.

### 5.1.2 Justification of the Materials Selection

By using the selected components a minimal model system was developed. Such a minimal model system allows the decoupling of all mutual interactions and one can focus on the physical aspects of transmembrane transport of nanoparticles while biochemical processes are missing. Moreover, all experiments were performed in aqueous solution without any additives, allowing the vesicle – particle interactions to be exclusively studied.

By using an extrusion technique PDMS-*b*-PMOXA polymersomes with a hydrodynamic radius,  $R_{\text{h}}$ , of around 100 nm were deliberately prepared to optimally use the characterization techniques, which are described in the following section 5.1.4. This vesicle size leads to a very low polydispersity, resulting in a better control of the system. These polymersomes combined with PS NPs or SiO<sub>2</sub> NPs constituted the minimal model system for the investigation of adsorption and transmembrane transport.

### 5.1.3 Characterization Methods with the Focus on the Application to the Presented Model

#### 5.1.3.1 Photon Correlation Spectroscopy (PCS)

Photon correlation spectroscopy (PCS) is a noninvasive light scattering technique with broad spatiotemporal range<sup>24, 25</sup>. In contrast to TEM, PCS measurements integrate over a large number of scattering centers. The application of PCS to the present system is optimal due to the mesoscopic lengths of the involved species and the large optical contrast between them and the solvent. Polymeric vesicles suspended in water have an inner and outer refractive index ( $n_{IN} = n_0$ ) equal to that of the solvent, in this case water ( $n_{H2O} = 1.333$ ). As illustrated in *Figure 5.6* however, the incorporation of particles ( $n_{PS} = 1.59$  and  $n_{SiO2} = 1.45$ ) will significantly change the refractive index of the polymersome interior  $n_{IN} = n_2$  (which will depend now on the fraction of particles  $\Phi_{NPs}$  and water  $\Phi_2$  inside the vesicle), and hence the total light scattering intensity. Further, the combination of large optical contrast and core-shell architecture of the polymersomes will render both the form factor  $P(q)$  (*Equation 3.43*) and the translational diffusion  $D(q)$  (*Equation 3.47*) sensitive indices of the uptake process.

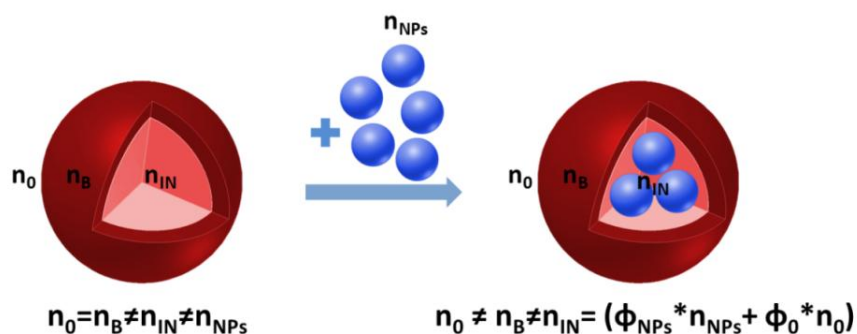


**Figure 5.6** Polymersomes (red) in the absence (left) and the presence of nanoparticles symbolized by blue spheres (right). Refractive indices of the solvent (water,  $n_0$ ), diblock copolymer bilayer ( $n_B$ ), and polymersome interior ( $n_{IN}$ ).

### 5.1.3.2 Fluorescence Correlation Spectroscopy (FCS)

In a FCS experiment, the fluorescent intensity fluctuations caused by the diffusion of fluorescent species through a very small observation volume (the focus of a confocal microscope) are monitored. Correlation analysis of these fluctuations yields information on the species' hydrodynamic radius, their concentration and fluorescent brightness. FCS allows probing selectively species of interest. In contrast to PCS, in a FCS experiment only fluorescent objects are “visible”. For the pair: polymersome/nanoparticle we have three measurement options possible. Selective probing of: (1) fluorescent nanoparticles while non-fluorescent polymersomes are not visible; (2) fluorescently labeled polymersomes while nanoparticles are not labeled or both of them. (3) In case of double labeling (both polymersomes and nanoparticles are labeled) separation of signal coming from both can be achieved by using dyes with different excitation wavelength.

### 5.1.3.3 Atomic Force Microscopy (AFM)

AFM is not only useful for the visualization of the objects. Besides this, force spectroscopy method can be used to determine nanomechanical properties of the materials (like the Young's modulus and bending modulus), as described in section 3.6.3. Material parameters like Young's modulus and bending modulus can be obtained by converting force vs. deformation data from AFM force spectroscopy and utilizing the bilayer thickness calculated from cryo-TEM micrographs (see the following 5.2.1.2).

Probing mechanical properties of both lipid and polymeric vesicles with the sizes in the range of micrometers has been carried out successfully in several studies before based on the micropipette aspiration method.<sup>11, 26, 27</sup> This method has one important limitation, mainly cannot be applied for nanometer size vesicles. This limitation has its source in the diffraction limited optical detection as well as the inner diameter of the micropipette. To obtain quantitative

information about Young's modulus on a sub-micrometer scale for soft materials it is important to apply a local probe using small deformation. The atomic force microscope provides an ideal tool which allows not only imaging surfaces with nanometer resolution but also locally probing interactions like adhesion and friction. Different forces applied with an AFM probe results in certain deformation. From such force *vs.* deformation characteristics, material properties including Young's and bending moduli can be extracted. This has been demonstrated for single cells,<sup>28</sup> polyelectrolyte multilayer capsules,<sup>29</sup> unilamellar liposomes<sup>30, 31</sup> and block copolymer vesicles.<sup>18</sup> In order to probe mechanical properties of polymersomes preserving their natural aqueous environment is crucial. Drying of polymersomes would lead to a collapse and to a significant change of mechanical properties. To define precisely their mechanical features AFM measurements have to be carried out in aqueous media.

#### **5.1.3.4 Transmission Electron Microscopy (TEM)**

In case of polymersomes composed of polymers with low  $T_g$  any investigation in dry state are meaningless. Drying of the sample would lead to a removal of the natural environment of the polymersomes: water. Polymersomes in dry state are not able to keep their shape and structure and as a result collapsed or destroyed vesicles are observed. To overcome this limitation cryo-TEM imaging is favored. Rapid cooling result in trapping of structures and preserved their form as present in solution. Cryo-TEM imaging provides a direct static picture of the system. However, as the sample is investigated in a frozen state, information on the dynamics of the process is lost. Furthermore, in the TEM studies shown above, only a relatively small number of individual structures can be evaluated statistically. Due to above mentioned drawbacks cryo-TEM imaging can be utilized only as a technique supplementary to other techniques like PCS or FCS.

## 5.2 Characterization of Polymersomes and Colloidal Nanoparticles

*A* complex characterization of PDMS-*b*-PMOXA polymersomes is presented in this section. Combination of photon correlation spectroscopy (PCS), atomic force microscopy (AFM) and cryo transmission electron microscopy (cryo-TEM) deliver a complete picture of the used polymersomes in the designed model system. Basic characterization of the second component of the model system, the nanoparticles, is also described in this chapter.

Adapted with permission from:

**Jaskiewicz, K.;** Makowski, M. M.; Kappl, M.; Landfester, K.; Kroeger, A., Mechanical Properties of PDMS-*b*-PMOXA Polymersomes Probed by AFM. *Langmuir* **2012**, *28*, 12629–12636

Copyright (2012) American Chemical Society

## 5.2.1 PDMS-*b*-PMOXA Polymersomes Characterization

In this section, the shape and size of PDMS-*b*-PMOXA polymersomes as well as the membrane thickness and their adsorption behavior to two model surfaces were investigated by using dynamic and static light scattering (DLS, SLS), cryogenic transmission electron microscopy (cryo-TEM) and atomic force microscopy imaging and force spectroscopy (AFM). The combination of all these techniques is necessary to obtain a complete picture of the properties of this kind of polymersomes. DLS experiments deliver information about the undisturbed size of polymersomes in solution, which can be compared to cryo-TEM data to exclude artifacts due to freezing of these objects and to the conformation in the adsorbed shape. Adsorption of the PDMS-*b*-PMOXA vesicles to flat substrate is a prerequisite to characterize their mechanical properties by AFM force spectroscopy, so comparison of conformation in the adsorbed state by AFM imaging to that free in solution by DLS adds valuable information about the change in conformation during adsorption.

### 5.2.1.1 Static and Dynamic Light Scattering

#### 5.2.1.1.1 Static Light Scattering (SLS)

PDMS-*b*-PMOXA polymersomes were investigated by SLS to determine the  $M_w$  app, the PD, the  $R_g$  as well as the form factor  $P(q)$ . The absolute Rayleigh intensity  $R_{vv}(q)$  (static light scattering intensities) of all polymersomes in five different concentrations, as described in 4.1.2.2, were measured and plotted vs  $q$ , as shown in Figure 5.7. The scattering patterns were fitted by a form factor represented by Equation 3.39 (Chapter 3.6.1.2). Because no minimum in the scattering pattern was observed at high  $q$ 's, polydispersity  $PDI > 1$  was introduced into the form factor equation, using a Schulz-Zimm distribution (see Equation 3.41).

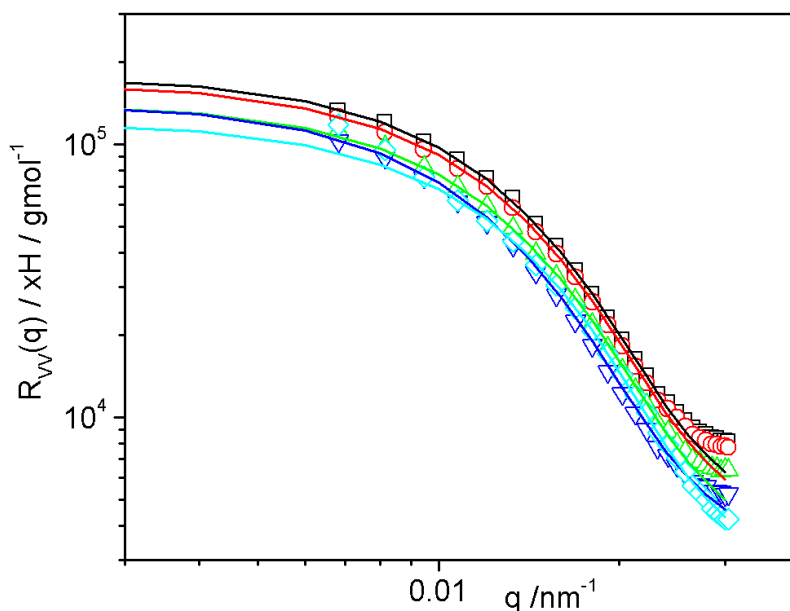


**Figure 5.7** SLS Absolute Rayleigh intensity  $R_{vv}(q)$  vs. scattering wave vector  $q$  for different vesicles concentrations;  $c_1 = 0.7 \text{ gL}^{-1}$  (black),  $c_2 = 0.35 \text{ gL}^{-1}$  (red),  $c_3 = 0.07 \text{ gL}^{-1}$  (green),  $c_4 = 0.035 \text{ gL}^{-1}$  (blue),  $c_5 = 0.007 \text{ gL}^{-1}$  (cyan); solid lines represent the fit using *Equation 3.39 and Equation 3.40* to the experimental data.

The form factor did not change significantly for all concentrations and the intensity was fitted with  $R_n = 95 \text{ nm}$  and  $PD = 1.25$  as shown in *Figure 5.7*. Because of the strong curvature of the inverse intensity it was difficult to obtain  $R_g$  and neither using the Zimm plot nor the Berry plot would lead to reasonable values for  $R_g$ .

#### 5.2.1.1.2 Dynamic Light Scattering (DLS)

Analog to the SLS experiments all samples were investigated *via* DLS. All determined correlation functions show a single relaxation process, as shown for sample  $c_1 = 0.7 \text{ gL}^{-1}$  in *Figure 5.8*.

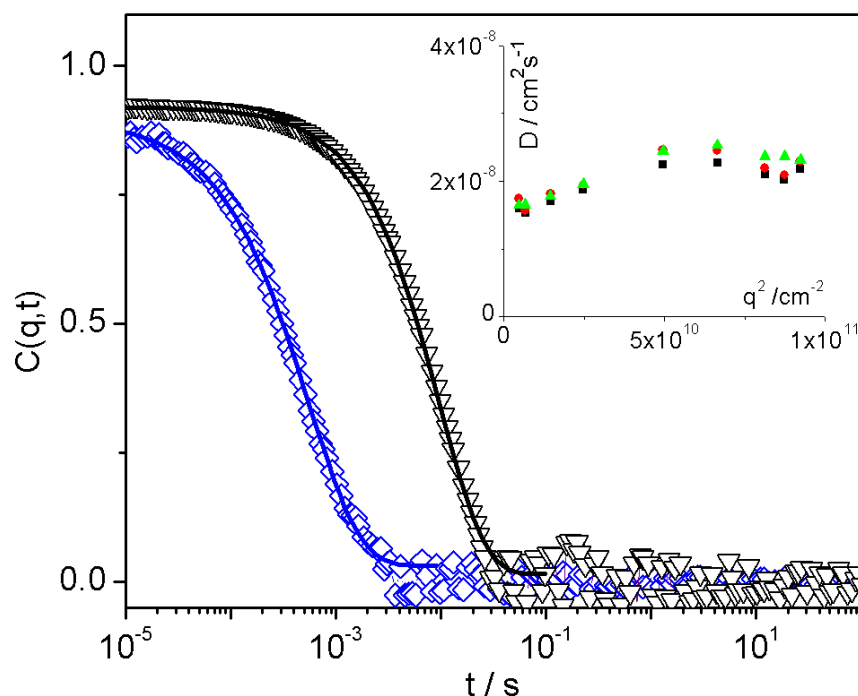


**Figure 5.8** Normalized correlation functions for  $c_1 = 0.7 \text{ gL}^{-1}$  at  $q = 0.02957 \text{ nm}^{-1}$  (blue) and  $q = 0.00814 \text{ nm}^{-1}$  (black) and their corresponding KWW fits. Inset:  $D$  vs.  $q^2$  for CONTIN (black), KWW (red) and cumulant (green) analysis.

Three different algorithms were applied to analyze the DLS data (see 3.6.1.1.1). The CONTIN analysis showed for all  $q$  values reliable fitting and the existence of only one diffusing process (one peak varying in broadness).

As a second type of analysis the stretched exponential fit (KWW, see 3.6.1.1.1) was used. This type of analysis was applied to all concentrations and showed similar behavior at all samples. At high  $q$  values a distribution of the relaxation times of  $\beta_{KWW} \sim 0.9$  was determined, while at the lower  $q$ 's the correlation functions were single exponential with a  $\beta_{KWW}$  very close to 1. These values confirm the existence of only one diffusing process as determined by CONTIN as well.

A third type of analysis, the cumulant analysis (see 3.6.1.1.1), was applied. The fit was satisfactory when the first cumulant was stable and the value of the second cumulant reached minimum and the standard deviation was less than 5%.

As shown in the inset of *Figure 5.8*, at lower  $q$ 's the diffusion coefficients from all three types of analysis superimpose well. At high  $q$  the KWW and CONTIN analysis show similar behavior while the cumulant analysis leads to slightly higher diffusion coefficients and therefore result in slightly smaller values for  $R_h$  (not shown).

As shown in the inset of *Figure 5.8* the diffusion coefficient shows  $q$ -dependence. This could be attributed to the vesicles' polydispersity and their size. To extract the zero angle ( $q \rightarrow 0$ ) diffusion coefficients  $D_0$ , *Equation 3.23* was used. It fits the lower  $q$ -range rather well for all three types of the above mentioned analysis. Fits over all the  $q$ -range, however, were not possible due to the fact that at higher  $q$ 's a small slowing down of the correlation functions was observed (independent of the type of analysis used).

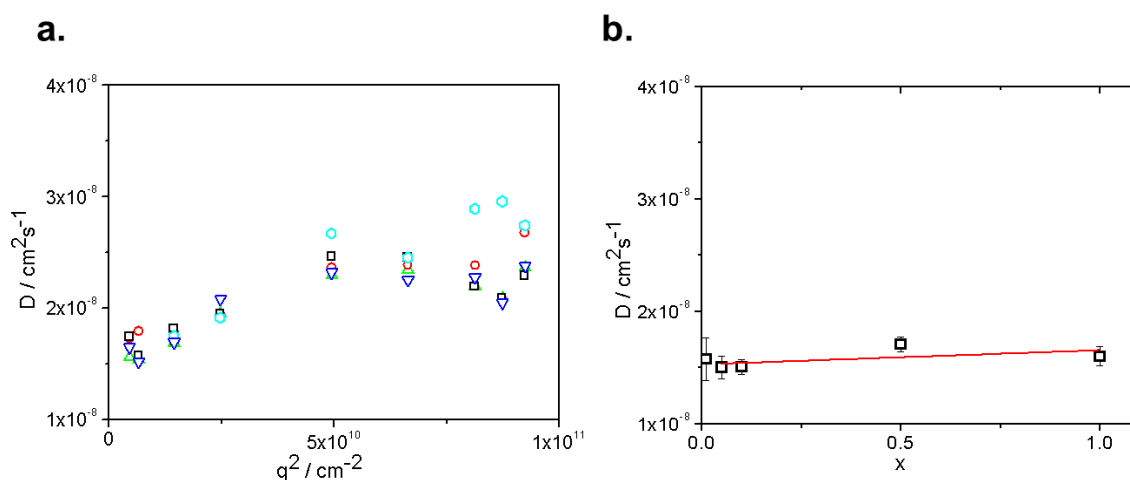


**Figure 5.9** a.  $D_t$  vs.  $q^2$  for all 5 concentrations;  $c_1 = 0.7 \text{ gL}^{-1}$  (black),  $c_2 = 0.35 \text{ gL}^{-1}$  (red),  $c_3 = 0.07 \text{ gL}^{-1}$  (green),  $c_4 = 0.035 \text{ gL}^{-1}$  (blue),  $c_5 = 0.007 \text{ gL}^{-1}$  (cyan) b.  $D_t$  vs.  $c$  ( $c_1$ )

The concentration dependence of the diffusion coefficient is very weak as shown in *Figures 5.9a* and *5.9b*. Except for the smallest concentration  $c_5 = 0.007 \text{ gL}^{-1}$ , the diffusion vs.  $q^2$  shows very similar behavior in all concentrations. At low  $q$ 's the diffusion coefficients superimposes rather well. Also the trend of the slight slowing down of the diffusion at high  $q$ 's is visible for all 4 concentrations ( $c_1$ - $c_4$ ).

The diffusion at zero angle ( $q \rightarrow 0$ ) and zero concentration ( $c \rightarrow 0$ ) was found to be  $D_0 = (1.53 \pm 0.072) \cdot 10^{-8} \text{ cm}^2 \text{ s}^{-1}$  and the coefficient  $c \cdot k_D = 0.08293$ , leading to a hydrodynamic radius of the PDMS-*b*-PMOXA polymersomes (in the absence of any NPs) of  $R_h = 140 \text{ nm}$ .

### 5.2.1.1.3 SLS/DLS Comparison

As shown in *Figure 5.7* the experimental data could be fitted quite precisely with *Equation 3.40* for a bilayer thickness  $d = 16 \text{ nm}$  (see 5.2.1.2) leading to  $R_n = 95 \text{ nm}$  and  $\text{PD} = 1.1$ . Furthermore the change of the normalized intensity over concentration is rather small. The same behavior is observed for the intensities extracted from the DLS data as shown in *Figure 5.10a*. Here the form factor with the same parameters as described above was applied to describe the intensity. The agreement between SLS and DLS data is very good.

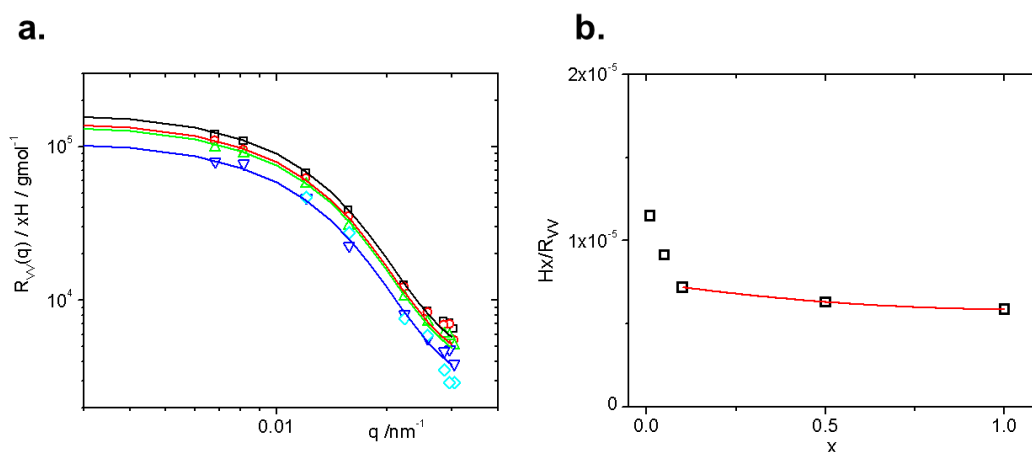


**Figure 5.10 a.** DLS absolute Rayleigh intensity  $R_{VV}(q)$  vs. scattering wave vector  $q$  for different vesicles concentrations;  $c_1 = 0.7 \text{ gL}^{-1}$  (black),  $c_2 = 0.35 \text{ gL}^{-1}$  (red),  $c_3 = 0.07 \text{ gL}^{-1}$  (green),  $c_4 = 0.035 \text{ gL}^{-1}$  (blue),  $c_5 = 0.007 \text{ gL}^{-1}$  (cyan); solid lines represent the fit using *Equation 3.40* to the experimental data **b.** Absolute Rayleigh inverse intensity vs. concentration.

At the lower concentrations  $c_4$  and  $c_5$  the intensity from SLS and DLS differs because of the additional contributions coming from possible aggregates. At  $c_5 = 0.007 \text{ gL}^{-1}$ , it was impossible to obtain reasonable correlation functions for the two lowest  $q$ 's due to the very weak scattering intensity.

As indicated on *Figure 5.7* and *Figure 5.10a* the plateau region at very low  $q$ 's ( $q < 0.005 \text{ nm}^{-1}$ ) was not measurable due the given  $q$ -range of the LS-setup used. That could explain why a strong curvature on the inverse intensity in the Zimm plot ( $1/I(q)$  vs.  $q^2$ ) as well as in the Berry plot ( $\sqrt{(1/I)}$  vs.  $q^2$ ) was observed and why calculation of reasonable value for  $R_g$  was difficult. Assuming that the intensity of vesicles does follow the form factor  $I_p(q)$  all the way to  $q = 0$ , the zero angle intensity for all concentrations with  $\sqrt{(1/I)}$  vs.  $q^2$  can be extracted. As shown in *Figure 5.10b*, plotting the extracted values vs. the concentration allows estimating of the  $M_{w \text{ app}}$  and second virial coefficient  $A_2$  of the vesicles. Using *Equation 3.28* the molecular weight  $cM_w = 134 \text{ kg/mol}$  and  $cA_2 = -1.54 \cdot 10^{-6}$  was found. Assuming the concentration of the stock solution to be  $c_1 = 0.7 \text{ gL}^{-1}$ , it would lead to  $M_{w \text{ app}} = 191 \cdot 10^6 \text{ g mol}^{-1}$  and  $A_2 = -4.4 \cdot 10^{-4} \text{ mol} \cdot \text{dm}^2 \cdot \text{g}^{-2}$ .

### 5.2.1.2 Cryo-TEM analysis

In TEM studies only a relative small number of individual structures can be evaluated statistically, whereas DLS measurements are integrating over a large number of scattering centers. In all the scattering experiments, ensemble averages were determined. Thus, the DLS experiments permit certain statistical analyses of the self-assembled aggregates whose structures can be inferred from direct imaging via TEM. Furthermore, in DLS, structural analyses are carried out in solution. In that environment, the cores of the formed aggregates are swollen, and the corona is expanded. In contrast, conventional TEM measurements are performed on dried samples and do not represent a realistic picture of PDMS-*b*-PMOXA polymersomes, because

such vesicular structures do not preserve spherical shape while aqueous medium is removed from the interior. Nevertheless, TEM studies are necessary and common to determine the membrane or wall thickness  $d$  of vesicles. Here, cryo-TEM was applied to ensure imaging polymersomes as they are in solution and to avoid artifacts.

Typical cryo-TEM micrographs of the PDMS-*b*-PMOXA polymersomes are shown in *Figure 5.11*. The vesicular structure of the objects can be clearly identified due to the electron density contrast between the polymeric membrane and the vesicle interior filled with water. The cryo-TEM images reveal the presence of uniformly shaped polymersomes (see *Figure 5.11a*) with an  $n$ -average geometrical radius of  $r = 131 \pm 18$  nm and a membrane thickness of  $d = 16 \pm 2$  nm, which were obtained from several micrographs and are based on statistics for  $\sim 200$  items (see *Figure 5.11d*).

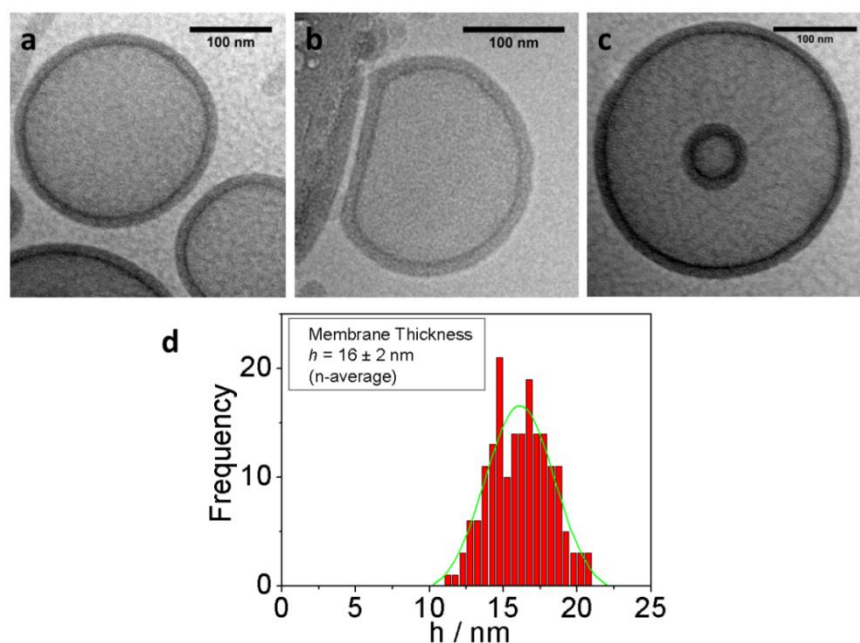


**Figure 5.11** Cryo-TEM micrographs of PDMS-*b*-PMOXA polymersomes in aqueous solution ( $c_p = 0.7$  g/L). **a.** Free spherical vesicles and **b.** deformed vesicle in contact with a surface, **c.** enclosed small vesicle in larger polymersome (“pregnant” vesicle); **d.** Histogram showing the membrane thickness distribution of the polymersomes.

The size of single objects is in good agreement with DLS results as presented above. Isolated polymersomes exhibit a spherical shape. However, polymersomes in contact with an edge of a carbon hole of the TEM grid deformed readily as shown in *Figure 5.11b* even though they are not expected to adsorb strongly to the surface of the carbon edges. This contact flattening clearly indicates that PDMS-*b*-PMOXA polymersomes do not behave as rigid objects but can easily be deformed.

Another feature that became obvious from the cryo-TEM micrographs is that a fraction of ~5% of the polymersomes exists as “pregnant” objects where smaller vesicles are enclosed within larger polymersomes (see *Figure 5.11c*). The formation of such vesicular structures of PDMS-*b*-PMOXA is described in the literature<sup>32</sup> and was first reported for polystyrene-*b*-poly(ethylene oxide) (PS-*b*-PEO) diblock copolymers by Eisenberg and co-workers.<sup>19</sup> Here, the structure formation process can be described by the self-assembly of entrapped polymer chains inside larger vesicles due to different diffusion rates of water and used solvent during polymersome preparation.<sup>33</sup> Such irregular structures are expected for relatively high polymer concentrations ( $c_P > 5 \text{ gL}^{-1}$ ). Polymersomes used in this study are prepared by film hydration followed by extrusion method. Here, due to the entrapment of solved polymer chains within a small fraction of formed polymersomes such irregular structures occur at much lower  $c_P$ .

### 5.2.1.3 Atomic Force Microscopy Imaging and Force Spectroscopy

To study the adsorption behavior of PDMS-*b*-PMOXA polymersomes and characterize their mechanical properties AFM imaging and force spectroscopy is used. Images recorded using tapping mode AFM reveal the presence of polymersomes adsorbed on silicon wafer as shown in *Figure 5.12a*. Here, the vesicular structure is preserved but their shape is changed from spheres to that of spherical caps as can be seen in the cross-section (see *Figure 5.12b*). It is a well-known phenomenon that liposomes as well as polymersomes adsorbed onto solid substrate may adopt a

different shape. The attractive interaction between substrate and vesicle surface (which is a prerequisite for adsorption) leads to deformation, in particular spreading of the polymersomes. Depending on the interfacial energy between the bilayer and the substrate relative to the mechanical energy necessary for deformation, either partial spreading will occur, leading to cap-like shapes as observed here, or complete spreading with vesicle fusion to the substrate and formation of a solid supported bilayer will prevail.

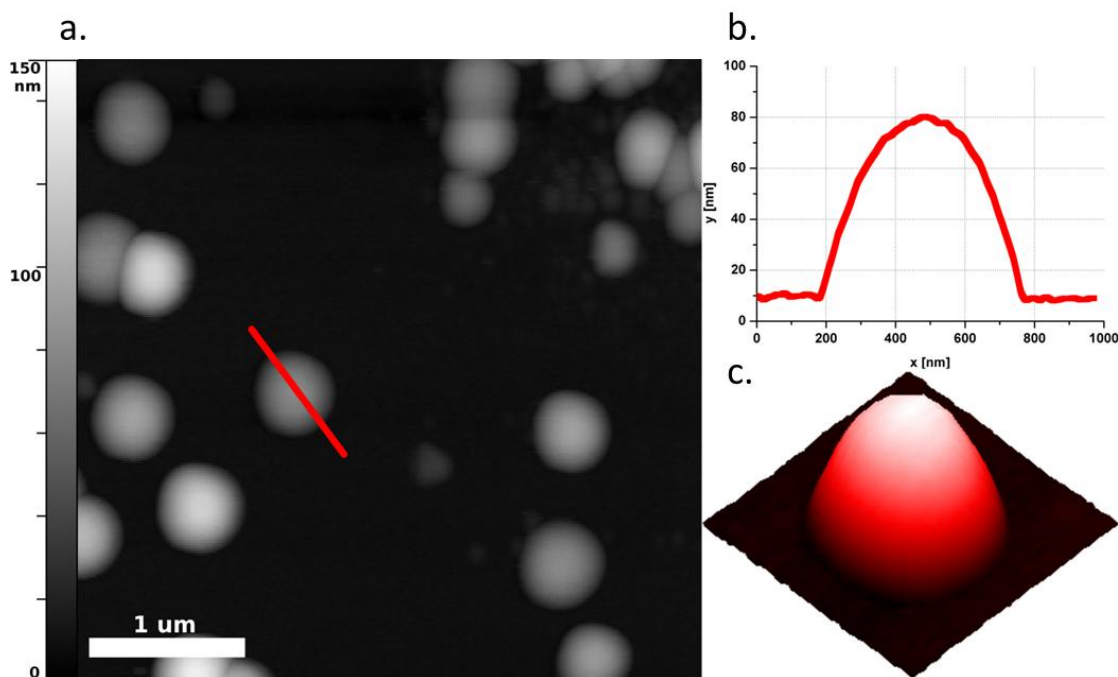


**Figure 5.12** AFM tapping mode image of PDMS-*b*-PMOXA polymersomes adsorbed on a silicon surface in aqueous solution. **a.** Height image of vesicles and **b.** cross section of a single polymersome along the red line shown in **a**, revealing the shape of a spherical cap. **c.** 3D representation of the single polymersome in **b**, lateral image size 1 μm x 1 μm. Note the different scales in x, y and z in **b** and **c**.

Polymersomes studied here in contact with silicon surface adopted shape of spherical caps with an average width of ~500 nm and typical height of 80 nm (based on statistics for 30 items), i.e. a ratio of 6.25:1 between width and height. In the example from the TEM images (*Figure 5.11b*), a width of 230 nm and a height of 160 nm is observed, corresponding to a much smaller

ratio of 1.44:1. Due to the lower surface energy of the TEM carbon grids, less deformation of the polymersomes is induced. While the polymersomes are flexible enough to deform significantly in contact with the silicon surface, they are mechanically stable enough not to rupture and fuse with the silicon wafer surface. The volume of the spherical cap shown in *Figure 5.12b* corresponds to that of a sphere with an  $n$ -average radius of 135 nm. This value is close to the values obtained from DLS and cryo-TEM analysis (shown above), which indicates that there is no significant leakage of liquid from the polymersomes interior during the adsorption process.

To quantify the mechanical characteristics of PDMS-*b*-PMOXA polymersomes, the AFM tip was placed above the crest of a single vesicle and the cantilever deflection while approaching the vesicle was recorded. The data were converted to force vs. distance curves as described above (see *Figure 5.13*).

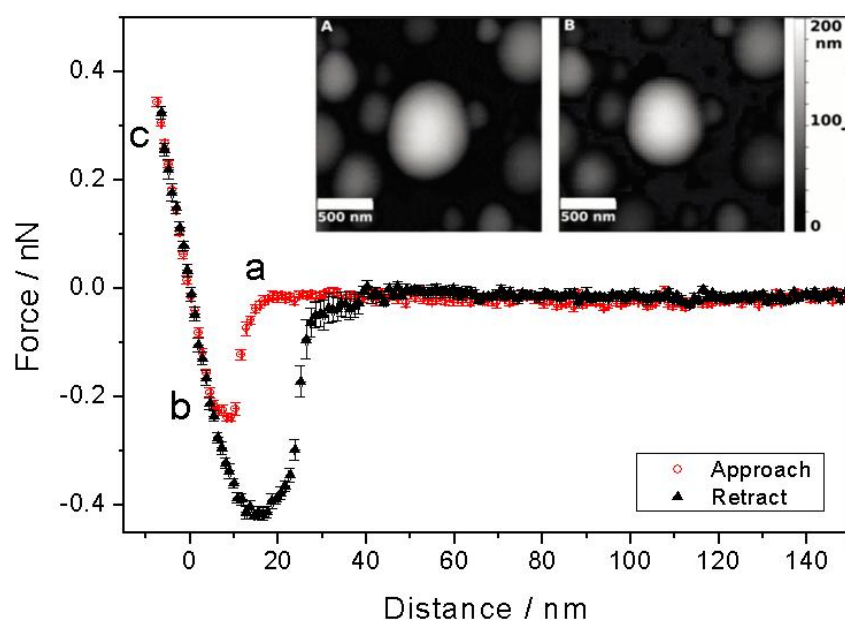


**Figure 5.13** Representative force vs. distance data obtained on a single PDMS-*b*-PMOXA polymersome. Data points are averages of 11 force curves, with error bars giving the standard deviation. At point **a**, contact between tip and vesicle is established. The region between **b**. and **c**. is used to obtain the vesicle stiffness  $\kappa_B$  by a linear fit. The inset shows AFM height images recorded **A** before and **B** after force measurements to verify intactness of vesicles and absence of drift during measurements.

When approaching, the cantilever bends downwards as soon as the tip contacts the vesicle (point **a** in *Figure 5.13*) due to attractive forces between them. Slight wrapping of the polymeric bilayer around the tip apex might occur as well during this process. This attraction arises due to van der Waals forces between tip and polymersome. There might also be a small contribution of electrostatic forces since the polymersomes are slightly positively charged ( $\zeta$ -potential of +30 mV) and the silicon tip has a negative surface charge. Strong electrostatic interactions should be recognizable as longer range attraction before jump-in.

Other possible attractive forces can be ruled out: since both tip and polymersome surface are hydrophilic, hydrophobic force cannot be the cause for attraction. Bridging by adsorption of single polymer chains would only occur between two surfaces that are partly covered by polymers and would lead to single chain detachment events in the retract curves, which we do not observe. Upon further approach a repulsive force that increases linearly with increasing deformation of the vesicle (point **b** to **c** in *Figure 5.13*) is observed. From a linear fit of that region, the stiffness  $\kappa_B$  of the polymersome is determined. When the movement of the tip is reversed, the retract curve perfectly overlaps the approach curve for that linear portion. From this fact two conclusions are deducible: i) there is no viscous response of the polymersome on the timescale of one force curve and ii) there is no change in the volume of the investigated vesicle by squeeze out of liquid, since both effects would lead to a hysteresis between approach and retract curves in that range. The observed hysteresis between approach and retract after the linear part is due to contact adhesion.

When taking force *vs.* distance curves on soft samples, a precise definition of zero distance becomes difficult, since surfaces will deform due to surface forces. We have set zero distance as the intersection point of the extrapolation of the zero force base line with the slope of the force curve in the constant contact part. By this choice, we count all deformations due to an applied

external load as negative distances. Other possible choices for zero distance would be the point of jump-in or the onset of repulsion. However, any other choice of zero distance would only lead to a shift of the curve along the x-axis but not change the slope of the contact region, which is used to extract the mechanical characteristics of the polymersomes.

To ensure that during recording deflection *vs.* distance curves the tip did not change the position or destroy the investigated polymersome and/or no other irreversible deformations occur, imaging was performed before and after mechanical testing (insets A and B of *Figure 5.13*).

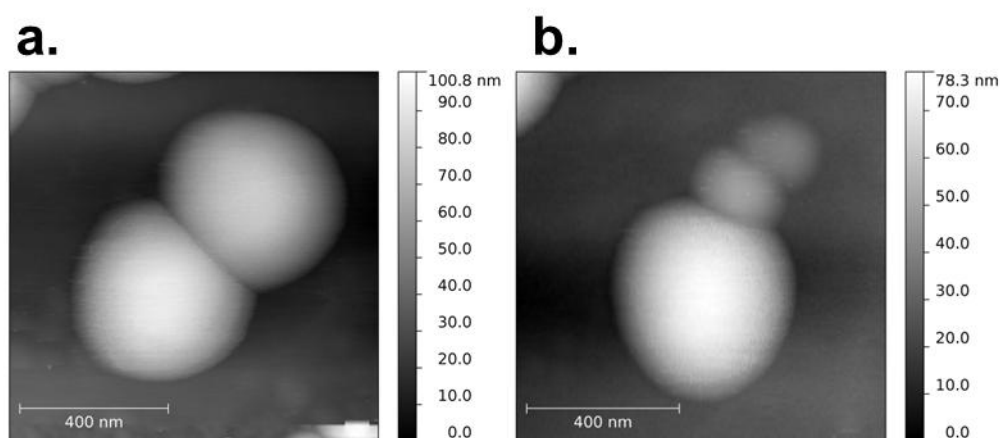


**Figure 5.14** Example of the splitting of a polymersome into two smaller ones during an AFM force spectroscopy experiment when applying a loading force of more than 20 nN. The upper right polymersome in image **a.** is split into two smaller vesicles as visible in image **b.**

For loading forces of up to 20 nN, changes in the shape of the adsorbed polymersomes are not observed, again indicating that no loss of liquid from the inner of the vesicle occurs due to the applied load. When even higher forces were applied, rupture of a PDMS-*b*-PMOXA polymersome can be induced, which results in splitting the object into two smaller vesicles (*Figure 5.14*)

Assuming point load and for deformations that are in the order of the shell or membrane thickness  $d$  and for the condition that  $d \ll R$ , where  $R$  is the radius of curvature of the polymersome, and that the liquid volume inside the polymersome is conserved, one can apply thin shell theory to relate polymersome stiffness  $\kappa_B$  with the Young's modulus  $E$  by:<sup>18, 34</sup>

$$\kappa_B = \frac{4Eh^2}{R\sqrt{3(1-\nu^2)}} \quad \text{Equation 5.1}$$

where  $\nu$  is the Poisson ratio. The radius of curvature  $R_{CV}$  of the vesicle that forms a spherical cap can be determined from its width  $W$  and height  $Y$  as determined from the AFM image by simple geometric considerations:

$$R_{CV} = \frac{0.25W^2 + Y^2}{2Y} \quad \text{Equation 5.2}$$

Note that this radius of curvature  $R$  is different from the radius  $r$  of the originally spherical polymersome. For the example in *Figure 5.12b*, a radius  $r = 136$  nm from the cap volume and  $R = 548$  nm from the cap shape was calculated. The bending modulus for a membrane with thickness  $d$  made of a material with Young's modulus  $E$  and Poisson ratio  $\nu_p$  is given by:<sup>18, 35, 36</sup>

$$\kappa_B = \frac{Ed^3}{12(1-\nu_p^2)} \quad \text{Equation 5.3}$$

For the calculations, the  $n$ -average membrane thickness of 16 nm as derived from the cryo-TEM images (see *Figure 5.11*) was used, since from the AFM images the shell thickness of polymersomes are not determinable. For the Poisson ratio a value of  $\nu_p = 0.5$  was used.<sup>30, 18</sup> Measuring stiffness and shape of 20 different adsorbed polymersomes lead to average values of the Young's and bending moduli  $E = 17 \pm 7$  MPa and  $\kappa_B = 7 \pm 3 \cdot 10^{-18}$  J respectively. Including

the spread of  $h = 16 \pm 2$  nm, one obtains ranges of  $E = 17 \pm 11$  MPa and  $\kappa_B = 7 \pm 5 \cdot 10^{-18}$  J (see *Figure 5.15*).

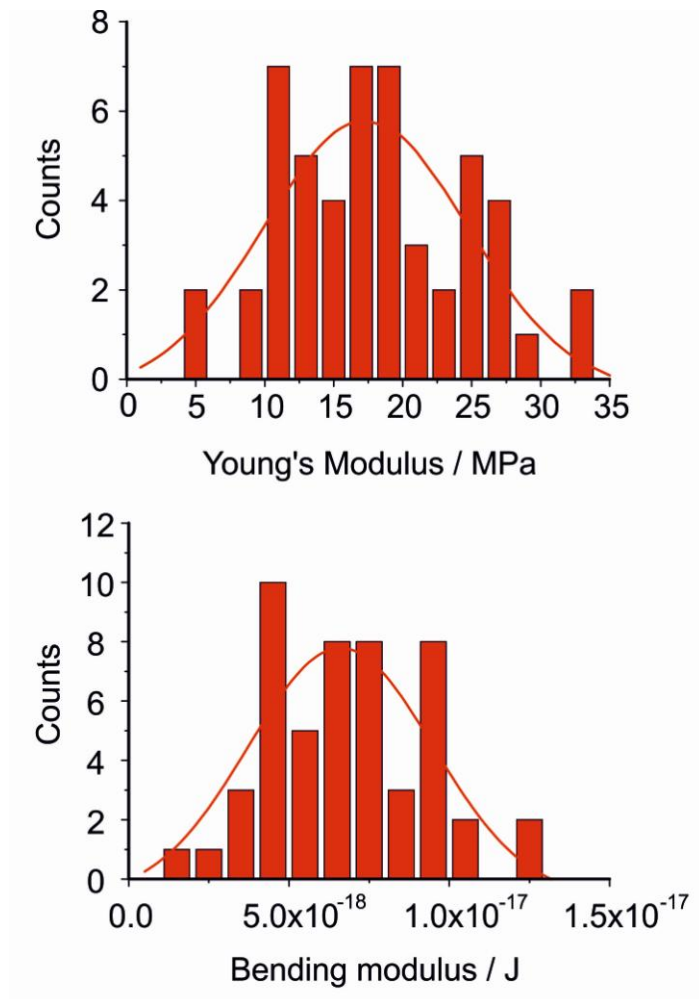


**Figure 5.15** Histograms of the Young's moduli **a.** and bending moduli **b.** of PDMS-*b*-PMOXA polymersome membranes. The solid lines are Gaussian fits with values of Young's modulus  $E = 17 \pm 7$  MPa and bending modulus  $\kappa_B = 7 \pm 3 \times 10^{-18}$  J as determined using *Equations 5.2* and *5.4*.

As an alternative substrate to silicon wafers for polymersomes adsorption, freshly cleaved muscovite mica was used. Also in this substrate, a change of the shape of the adsorbed polymersomes to a spherical cap was observed as shown in *Figure 5.16a*. However, in addition we observed circular patches of stacks of bilayers (*Figure 5.16b*) or of singular bilayers (*Figure*

5.16c), which indicate that the polymersomes tend to spread more strongly on this substrate. This is due to the higher surface energy of the freshly cleaved mica compared to the silicon wafer: While we observe complete spreading for a droplet of polymersome solution on freshly cleaved mica, such a droplet forms a contact angle of  $19^\circ$  on a silicon wafer. Surface energy of freshly cleaved mica in ambient is known to be in the order of  $120 \text{ mJ/m}^2$ .<sup>37</sup> Interfacial energy between polymersomes and mica in aqueous solution will certainly be lower than this value.

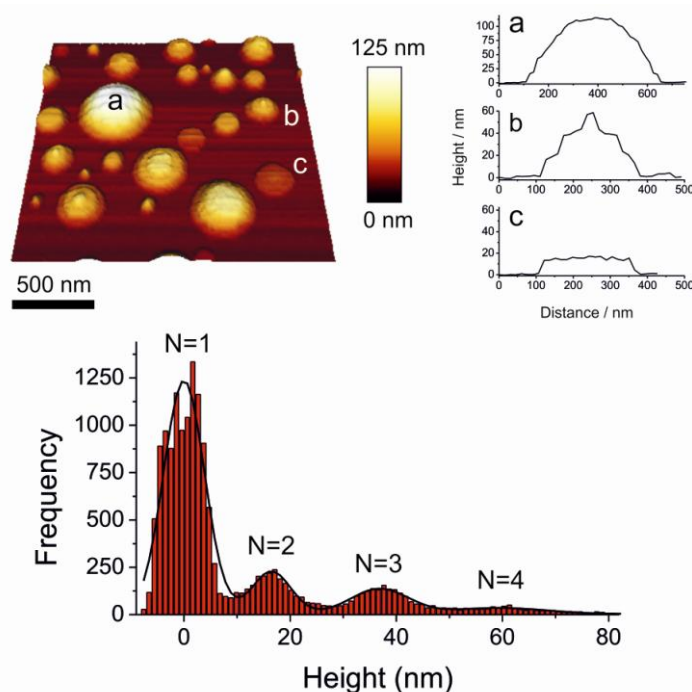


**Figure 5.16** Top left: AFM image of PDMS-*b*-PMOXA polymersomes adsorbed on a mica surface. Top right: Cross-sections of adsorbed polymersomes at positions *a* - *c*. While the polymersome at position *a* displays the same spherical-cap shape as for the case of the silicon wafer, additionally many polymersomes that have collapsed into single bilayers (position *b*) or stacks of several bilayers (position *c*) are seen. Bottom: histogram of all data points with fit curve using 4 Gaussian peaks.

The histogram of the height values of all data points is shown at the bottom part of *Figure 5.16*. The black solid line represents the fit of the histogram using 4 Gaussian peaks ( $N = 1, 2, 3$  and 4) with the parameters shown in *Table 5.1*.

**Table 5.1** Characteristics of the histogram of the height values determined by AFM for PDMS-*b*- PMOXA polymersomes adsorbed at mica substrate.

$N$	Height value / nm	Std. Deviation / nm
1	0.0	3.8
2	16.5	3.6
3	36.8	5.5
4	59.4	8.6

Here, the first peak ( $N = 1$ ) corresponds to the mica surface. The height value of  $N = 2$  precisely matches the value of 16 nm as determined from cryo-TEM for a single shell layer. Within the standard deviation of the measurement,  $N = 3$  corresponds to a double layer of shells and  $N = 4$  corresponds to 4 shell layers.

The formation of multilayers with an overall thickness of  $\sim 60$  nm, which corresponds to roughly 4 shell layers, would not be expected from a simple polymersome fusion for unilamellar vesicles.

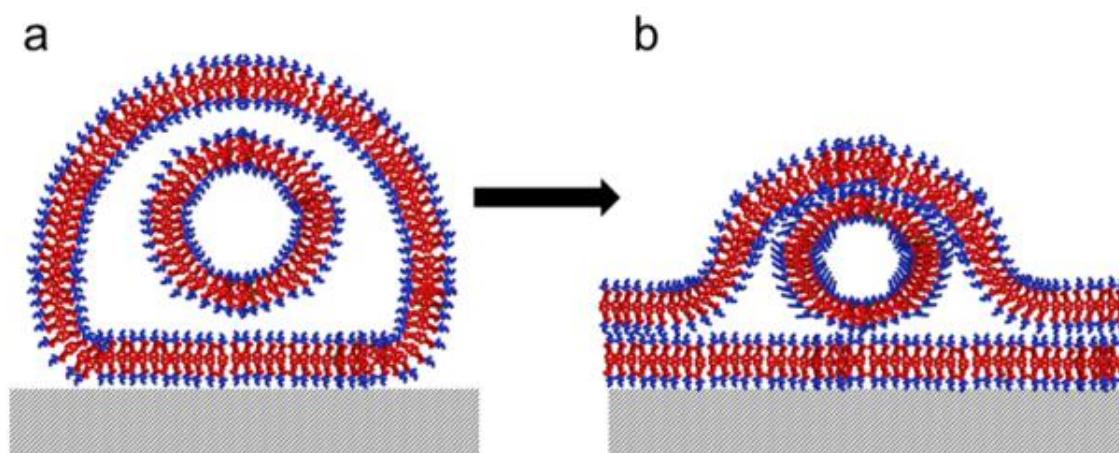


**Figure 5.17** Possible mechanism for formation of the stacked multilayers observed on mica. **a** After adsorption of “pregnant” polymersomes, **b** fusion with the solid support may lead to structures with 4 stacked bilayers.

However, from the cryo-TEM, it is known that a fraction of ~5% of the polymersomes exists as irregular structures. The collapse of these “pregnant” polymersomes adsorbed at the wafer surface might lead to the observed stacked structures as illustrated in *Figure 5.17*.

**Table 5.2** Comparison of membrane properties of liposomes and polymersomes determined by AFM.

Material	Reference	$h$ / nm	$E$ / MPa	$\kappa_B$ / $10^{-19}$ J
<b>EggPC</b>	<sup>38, 39</sup>	$6 \pm 0.6$	$2 \pm 0.8$	$0.3 \pm 0.1$
<b>DPPC</b>	<sup>31</sup>	~5	81	11.3
<b>DPPC</b>	<sup>30</sup>	~ 5	$110 \pm 15$	$14 \pm 2$
<b>PDMS<sub>68</sub>-<i>b</i>-PMOXA<sub>11</sub></b>	this work	$16 \pm 2$	$17 \pm 11$	$70 \pm 50$
<b>PS<sub>115</sub>-<i>b</i>-PAA<sub>15</sub></b>	<sup>18</sup>	$22 \pm 1$	$61 \pm 6$	$716 \pm 103$

**EggPC:** egg yolk phosphatidylcholine, **DPPC:** dipalmitoylphosphatidylcholine, **PS-*b*-PAA:** polystyrene-*block*-poly(acrylic acid)

*Table 5.2* lists the Young’s modulus and bending modulus of different vesicular systems as determined by AFM force spectroscopy. For fluid-phase lipids such as egg yolk phosphatidylcholine (EggPC), a value of the bending modulus of  $0.3 \cdot 10^{-19}$  J was found, which is in good agreement with values obtained by alternative methods.<sup>40</sup> For lipids in the gel-phase such as dipalmitoylphosphatidylcholine (DPPC), values in the order of  $10 - 15 \cdot 10^{-19}$  J are typical as also confirmed by optical techniques.<sup>41</sup>

## 5.2.2 Polystyrene and Silica Nanoparticles Characterization

### 5.2.2.1 Polystyrene Nanoparticles Characterization

Fluorescent polystyrene nanoparticles with  $\zeta$ -potential of - 23 mV were characterized with dynamic light scattering (DLS) at the concentrations ranging from  $0.2375 \text{ gL}^{-1}$  to  $19 \text{ gL}^{-1}$ . The computed autocorrelation functions showed single relaxation processes for all samples. The DLS data were evaluated using stretched exponential KWW fit (see Equation 3.17). The stretching parameter  $\beta_{KWW}$  varied from 0.86 at higher concentrations to 1 at middle and lower concentration (see Figure 5.18). The broader distribution of relaxation times for the sample with a higher concentration of  $c = 19 \text{ gL}^{-1}$  is attributed to a very slight particle agglomeration. Therefore, for further work NPs concentrations  $c < 1 \text{ g/L}$  are used.

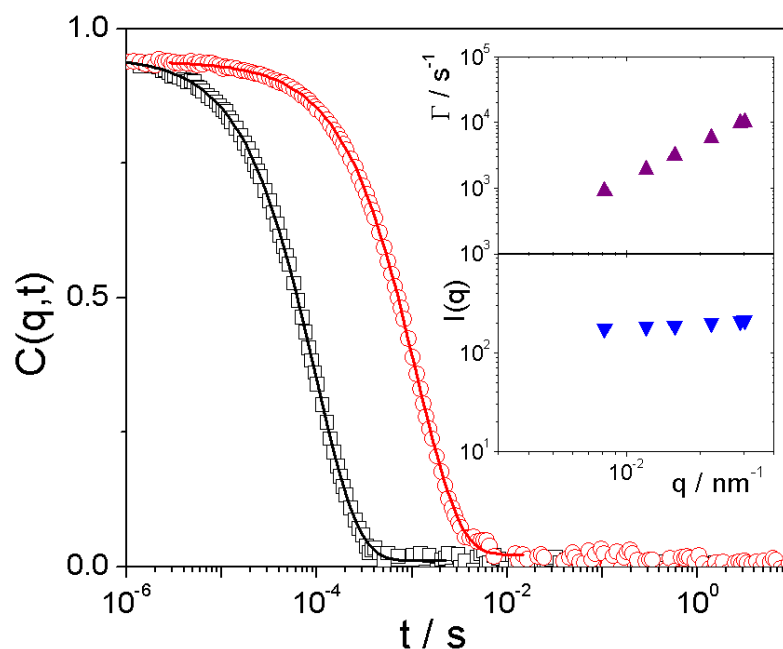


**Figure 5.18** Autocorrelation functions  $C(q,t)$  of polystyrene nanoparticles at  $c = 0.475 \text{ gL}^{-1}$  for two different  $q$  values (black:  $0.0304 \text{ nm}^{-1}$  and red:  $0.0081 \text{ nm}^{-1}$ ) along with their representation by KWW (Equation 3.17). Upper inset: Relaxation rate  $\Gamma$  vs. scattering wave vector  $q$ . Lower inset: Intensity vs. scattering wave vector  $q$ .

Diffusion was found to be almost concentration independent; the value of  $D_0 = 1.37 \cdot 10^{-7} \text{ cm}^2/\text{s}$  was calculated (see *Figure 5.19*), which corresponds to a hydrodynamic radius of  $R_h = 16 \text{ nm}$ . The same characterization procedure was used for all NPs samples.

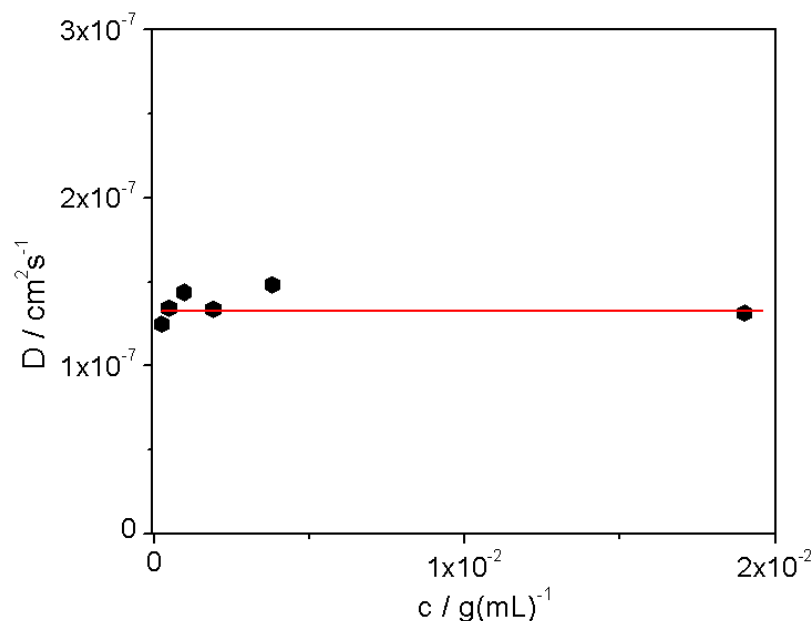


**Figure 5.19** Diffusion coefficients vs. concentration for PS nanoparticles in water.

### 5.2.2.2 SiO<sub>2</sub> Nanoparticles Characterization

Four SiO<sub>2</sub> nanoparticles are characterized by the same procedure as described before with both static (SLS) and dynamic light scattering (DLS) at the concentrations ranging from  $0.05 \text{ gL}^{-1}$  to  $2 \text{ gL}^{-1}$ . DLS data were evaluated using stretched exponential KWW fit (see 3.6.1.1.1, *Equation 3.17*).

Diffusion was found to be concentration independent. The hydrodynamic radius  $R_h$  of the nanoparticles determined using the Einstein-Stokes equation (*Equation 3.25*) was found to be 14 nm, 25 nm, 36 nm and 57 nm respectively.

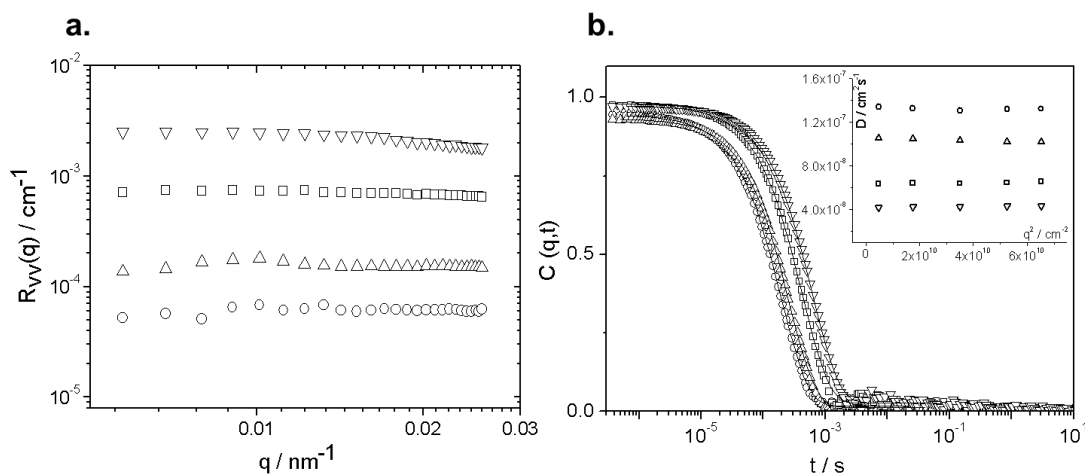


**Figure 5.20** a. Absolute Rayleigh intensity  $R_{VV}(q)$  as a function of  $q$  at  $T = 20$  °C; b. Autocorrelation functions  $C(q,t)$  at  $q = 0.0187 \text{ nm}^{-1}$  and their corresponding KWW ; inset: Diffusion vs.  $q^2$ ; for  $\text{SiO}_2$  nanoparticles with  $R_h = 14 \text{ nm}$  (empty circles),  $25 \text{ nm}$  (empty triangles),  $36 \text{ nm}$  (empty squares) and  $57 \text{ nm}$  (empty inverse triangles) at the concentration of particles;  $c_{\text{NP}} = 0.2 \text{ gL}^{-1}$ .

The  $\zeta$ -potential of the fluorescent silica nanoparticles of different sizes is presented in the

Table 5.3:

**Table 5.3** Zeta-potential of  $\text{SiO}_2$  nanoparticles used for the uptake studies.

Sample	$\zeta$ -Potential in mV
$R_h \text{ SiO}_2 \text{ NP} = 14 \text{ nm}$	-14
$R_h \text{ SiO}_2 \text{ NP} = 25 \text{ nm}$	-22
$R_h \text{ SiO}_2 \text{ NP} = 36 \text{ nm}$	-29
$R_h \text{ SiO}_2 \text{ NP} = 57 \text{ nm}$	-38

## 5.3 Probing Incorporation of Nanoparticles into Polymersomes

In this section a minimal model system, which allows the uncoupling of all interactions and processes inside the membrane, is presented. The model system is based on a vesicle-forming copolymer, and the experimental observation of nanoparticles transport into polymersomes is reported. A combination of photon and fluorescence correlation spectroscopies is used to study the internalization in detail. The resulting picture is supported by cryo-TEM imaging.

Adapted with permission from:

**Jaskiewicz, K.**; Larsen, A.; Lieberwirth, I.; Koynov, K.; Meier, W.; Fytas, G.; Kroeger, A.; Landfester, K., Probing bioinspired transport of nanoparticles into polymersomes. *Angew. Chem. Int. Ed.* 2012, *124*, 4691-4695

Copyright (2012) John Wiley and Sons

Polymeric vesicles composed of poly(dimethylsiloxane)-*b*-poly(2-methyloxazoline) (PDMS-*b*-PMOXA)<sup>32</sup> were chosen as a model system of an unspecified cell membrane (Figure 5.21). These polymersomes are an ideal model system, as the physical properties of their building blocks (polymer chains) are similar to phospholipids. Based on the values of Young modulus ( $\sim 17\text{MPa}$ ) and bending energy ( $\sim 7 \cdot 10^{-8}\text{ J}$ ),<sup>22</sup> (see 5.2.1) they provide the necessary fluidity of a membrane and concurrently ensure excellent mechanical stability. The latter is due to the slow exchange of polymer chains between aggregates compared to experimental time scale (kinetically trapped or “frozen” structures). In addition, polymersomes can be easily modified in both biological and chemical respects for further investigations.

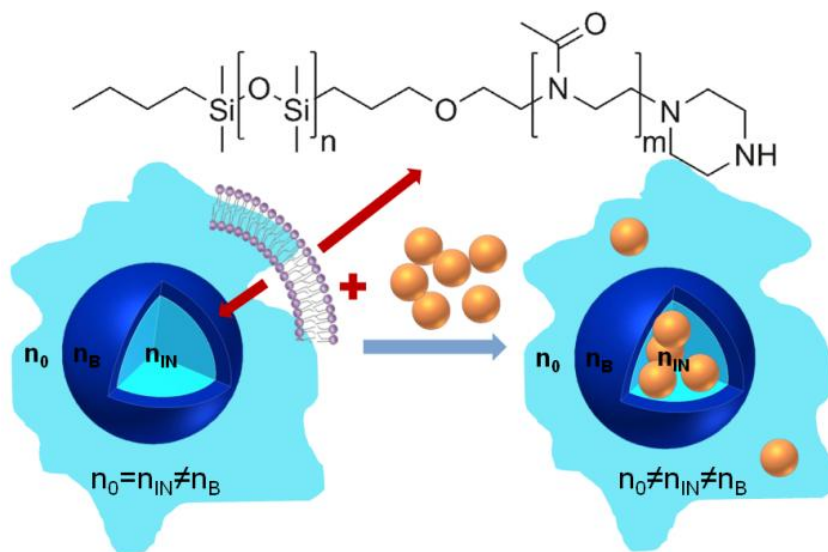


**Figure 5.21** The chemical primary structure of poly(dimethylsiloxane)-*b*-poly(2-methyloxazoline) (PDMS-*b*-PMOXA) forming the secondary structure, polymersomes (large blue spheres) in aqueous solution. Polymersomes in the absence (left) and the presence of nanoparticles symbolized by orange spheres (right).  $n_0$  – refractive index of the solvent (water),  $n_B$  – refractive index of the diblock copolymer bilayer,  $n_{IN}$  – refractive index of the polymersome interior.

These polymersomes combined with PS nanoparticles of  $R_h = (16 \pm 1)$  nm or SiO<sub>2</sub> nanoparticles with  $R_h = (14 \pm 1)$  nm constituted the minimal model system for the investigation of adsorption and transmembrane transport. Experiments were performed in aqueous solution without any additives, allowing the vesicle-particle interactions to be exclusively studied.

### 5.3.1 Cryo-TEM

In order to visualize adsorption and internalization of nanoparticles by polymeric vesicles, cryogenic transmission electron microscopy (cryo-TEM) images of the polymersome solutions containing either PS or SiO<sub>2</sub> nanoparticles were acquired (*Figure 5.22*). As shown in *Figure 5.22*, PDMS-*b*-PMOXA polymersomes incorporate both types of nanoparticles via an invagination process due to membrane deformation and subsequent fission of the bilayer membrane.

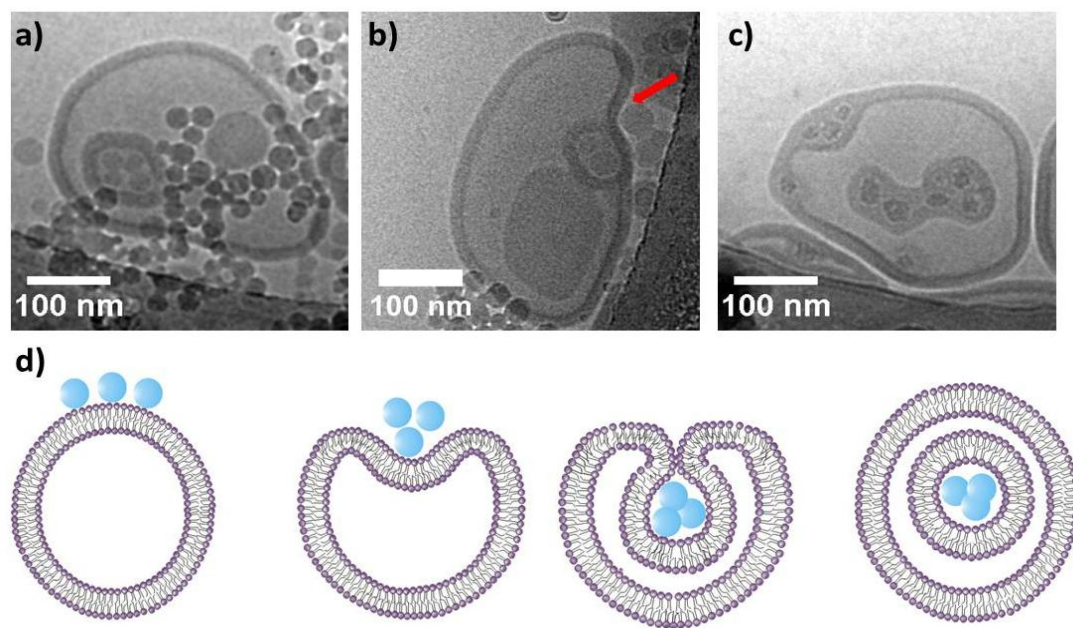


**Figure 5.22** Cryo-TEM micrographs of nanoparticles inside PDMS-*b*-PMOXA polymersomes. **a**, **b** and **c** Internalization of PS nanoparticles  $R_h = 16$  nm **a**, **b** and SiO<sub>2</sub> nanoparticles  $R_h = 14$  nm **c**. **d** Schematic illustration of nanoparticle internalization into polymersome, nanoparticles first absorbed, then wrapped by the polymeric membrane (red arrow) and finally completely incorporated (see text).

This process can be described in four steps: (i) nanoparticle adsorption at vesicle surface (*Figure 5.22a*), (ii) engulfing of single nanoparticles or groups of particles (*Figure 5.22b* and *5.22c*) by wrapping and formation of necks, (iii) entire coverage of nanoparticles by bilayer membrane (*Figure 5.22b*) and (iv) complete internalization (*Figure 5.22a* and *c*) driven by the antagonistic effects of bending and adhesion energy; additional contribution might arise from the entropy gain through the release of water from the nanoparticles surface<sup>42</sup>. *Figure 5.22d* is a schematic description of this process.

### 5.3.2 Photon Correlation Spectroscopy (PCS)

The variation of the excess absolute time-average scattered intensity, known as the Rayleigh ratio  $R_{vv}(q)$  ( $\sim P(q)$ ) and  $D(q)$  with the probing wave vector  $q$  fully characterizes the polymersome dilute solution with z-average radius  $R_h = (112 \pm 3)$  nm, size polydispersity  $PD = 1.1$  and a bilayer thickness  $d$  of 14 nm.

For the particle internalization experiments, a dilute aqueous polymersome solution (polymer concentration  $c_P = 4.5 \cdot 10^{-2}$  g/L) was mixed with a nanoparticle dispersion (nanoparticle concentration  $c_{NP} = 0.1$  g/L) at a number ratio 1:50 and then immediately probed by PCS (*Figure 5.24*). The initially low light scattering intensity (at  $q = 0.024$  nm<sup>-1</sup>) jumped to a much higher level, displaying strong fluctuations with elapsed time, and finally reached a plateau, as seen in *Figure 5.24a* for the PS ( $R_h = 16$  nm) and *Figure 5.24d* for SiO<sub>2</sub> ( $R_h = 14$  nm) nanoparticles. For both mixtures, the final scattering intensity is much higher than the sum of the scattering intensity contributions from the individual components and was significantly higher in the case of the PS/polymersomes system ( $\sim 10$  times higher) compared to SiO<sub>2</sub>/polymersomes ( $\sim 2$  times higher) as seen in *Figure 5.24*. The equilibration time was much shorter in the case of SiO<sub>2</sub> nanoparticles ( $\sim 8$  min), suggesting much faster internalization kinetics than in the case of PS nanoparticles ( $\sim 15$  min) with similar size (*Figure 5.24a* and *5.24d*). We assume the same uptake mechanism

(Figure 5.22) for both particles possessing, however, distinct surface chemistry. Therefore, the disparity in the internalization kinetics can relate to the different strength of the particle-membrane adhesive interactions.

The experimental  $R_{VV}(q)$  and  $D(q)$  were obtained from the concentration relaxation functions  $C(q, t)$  which were represented by a unimodal distribution function  $L(\ln\tau)$  as seen in Figure 5.24b and 5.24e. Freely diffusing nanoparticles were observed (weak peak in  $L(\ln\tau)$  of Figure 5.24b) only in the PS/polymersomes system due to the much larger optical contrast of PS compared to the  $\text{SiO}_2$  nanoparticles.

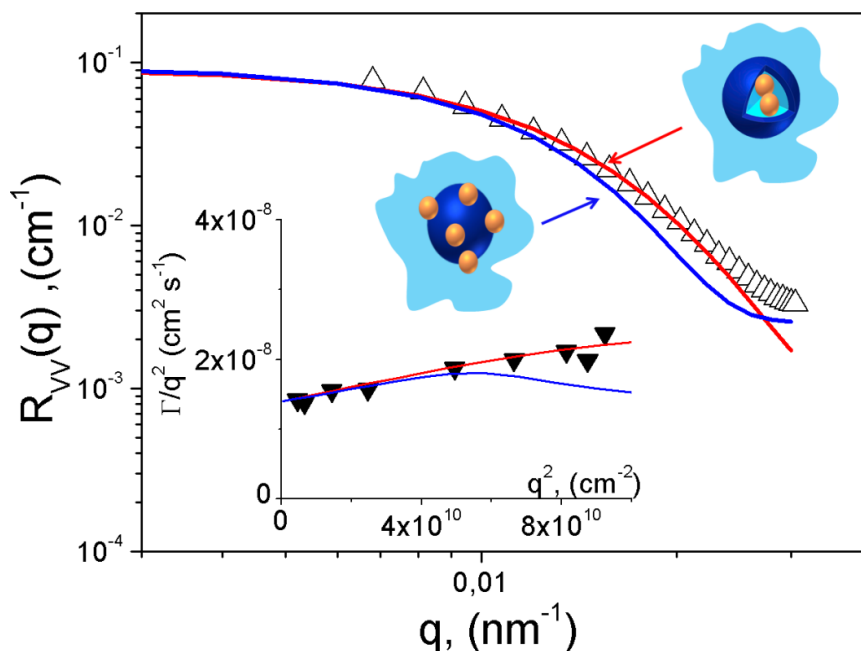


**Figure 5.23** Absolute Rayleigh intensity vs. wave vector  $q$  of polymersomes/PS mixture  $c_p = 4.5 \cdot 10^{-2}$  g/L and  $c_{NP} = 0.1$  g/L (empty triangles) with corresponding fits (solid line red: particles incorporated into polymersomes; solid line blue: vesicles with particles attached to the bilayer from outside) and translational diffusion coefficient  $D$  vs  $q^2$  (filled triangles) with corresponding fits (solid line red: particles incorporated into polymersomes; solid line blue: vesicles with particles attached to the bilayer from outside).

The single diffusional decay rate,  $\Gamma(q) = D(q)q^2$ , corresponding to the main peak of  $L(\ln t)$ , was used to compute the effective  $D(q)$  shown in the insets of *Figure 5.24c* and *f* for the two different systems. Assuming polymersomes are filled with nanoparticles (schematically shown in *Figure 5.21*), both experimental quantities,  $R_{\text{vv}}(q)$  and  $D(q)$ , were well represented by an form factor termed filled vesicle model (see *Equation 3.40*). An alternative model of a decorated vesicle (particles attached to the outer surface of polymersomes) fails to describe the experimental intensity pattern as displayed on *Figure 5.23*.

Therefore, it appears that after an equilibration time most of the polymersomes internalized nanoparticles. The moderate representation of the experimental  $R_{\text{vv}}(q)$  for PS/polymersomes system at the highest  $q$  values (*Figure 5.24c*) by the filled vesicle model is ascribed to moieties inhomogeneity which comprises different filled vesicles (number of internalized particles) and freely diffusing PS nanoparticles; in the case of  $\text{SiO}_2$  nanoparticles (with lower optical contrast) this contribution of system polydispersity and free nanoparticles is suppressed (*Figure 5.24f*).

The simultaneous description of both  $R_{\text{vv}}(q)$  and  $D(q)$  depends sensitively on the refractive index  $n_{\text{IN}}$  in the interior of the polymersomes, in addition to their average radius and size polydispersity. Since the latter two do not change significantly compared to the empty polymersomes, it is mainly the increase of  $n_{\text{IN}}$  above the pure water value that boosts the intensity  $R_{\text{vv}}(0)$  witnessed in *Figure 5.24* as described before.

From the data representation by the filled vesicle model, the values  $n_{\text{IN}} = 1.38 \pm 0.01$ , for polymersomes filled with  $\text{SiO}_2$  ( $R_{\text{h}} = 14$  nm) and  $n_{\text{IN}} = 1.41 \pm 0.01$ , for polymersomes filled with PS ( $R_{\text{h}} = 16$  nm) nanoparticles, correspond to about 40% and 30% particle loading of the vesicles interior, respectively. The average size of loaded polymersomes was found to be about 10% smaller than the unloaded species corresponding to ~20% volume shrinkage. This is in accord to

the average number of internalized particles and the associate membrane consumption (Figure 5.22).

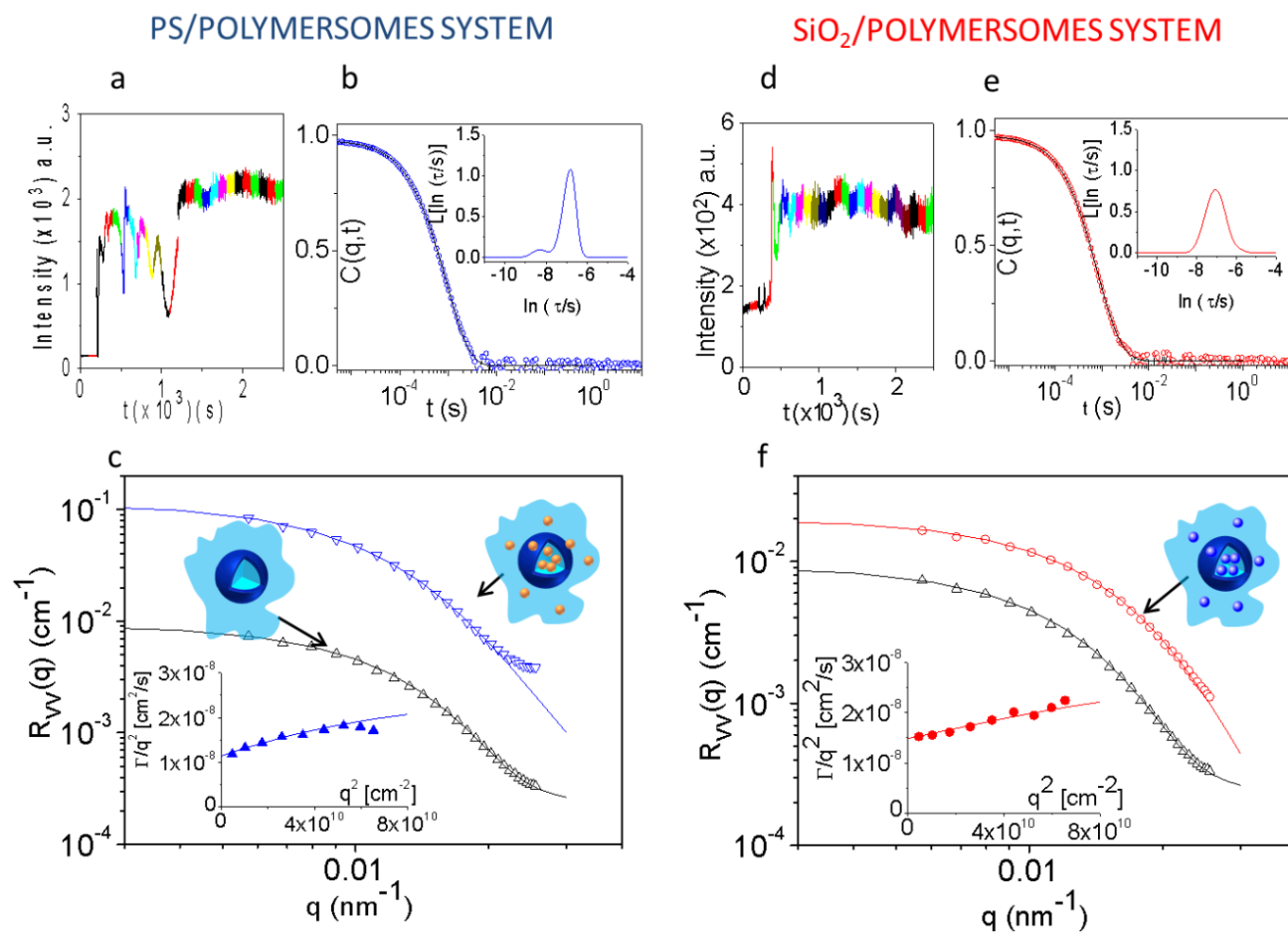


**Figure 5.24** Nanoparticles incorporation into PDMS-*b*-PMOXA polymersomes measured by PCS. **a** Total light scattering intensity at a scattering wave vector  $q = 0.024 \text{ nm}^{-1}$  as a function of time after the addition of PS nanoparticle suspension to the polymersome aqueous solution. Within the colored sections the dynamic state of the mixture was probed. **b** Normalized field autocorrelation functions  $C(q, t)$  of the PS/polymersomes system at a scattering wave vector  $q = 0.024 \text{ nm}^{-1}$  (diffusion length  $\sim 260 \text{ nm}$ ) along with the corresponding distribution of relaxation times  $L(\ln\tau)$  recorded after 2 h. **c** Absolute light scattering intensity (black triangles: empty polymersomes, blue inverse triangles: PS/polymersomes) and the  $D(q)$  (filled symbols) with corresponding form factor fit (solid lines) **d**, **e** and **f** The equivalent plots for the SiO<sub>2</sub>/polymersomes system (empty and filled red circles, black triangles: empty polymersomes). The state of the examined solution is schematically indicated in the insets of **c** and **f**.

A comparison with the extent of the internalization observed by cryo-TEM (*Figure 5.22*) is not straightforward due to the strong concentration dependence of the internalization process; the very low concentrations in PCS experiments are not sufficient for cryo-TEM imaging which required a much higher nanoparticles/polymersomes concentration. Instead, we employed fluorescence correlation spectroscopy (FCS) under the PCS experimental conditions, but using labeled nanoparticles.

### 5.3.3 Fluorescence Correlation Spectroscopy (FCS)

*Figure 5.25* presents typical fluorescence intensity autocorrelation functions  $G(t)$  recorded at different times after the injection of fluorescent PS nanoparticle suspension into the polymersome solution. Clearly, the autocorrelation curves progressively shift to longer diffusion times, indicating larger species with increased exposure time. We note that FCS monitors only the fluorescently labeled PS beads, either freely diffusing or incorporated in the larger polymer vesicles. The early and late stage curves (*Figure 5.25*, black and green symbols) are well represented by a single diffusing moiety (see theoretical introduction 3.6.2) with  $R_h = 16$  nm and 95 nm, respectively. These radii correspond to the free PS nanoparticles in the initial stage (2 min) and polymer vesicles loaded with PS nanoparticles at the late stage (~ 2 h) of the loading process. From the average fluorescent brightness of the PS beads and the loaded polymersomes we estimated a loading of about 16 incorporated particles per polymeric vesicle, is in agreement with the PCS value. The experimental  $G(t)$  recorded after 10 and 30 min (*Figure 5.25*, red and blue symbols) can be represented by two diffusive decays, corresponding to freely diffusing PS beads with  $R_h = 16$  nm and loaded polymer vesicles with  $R_h = 95$  nm.

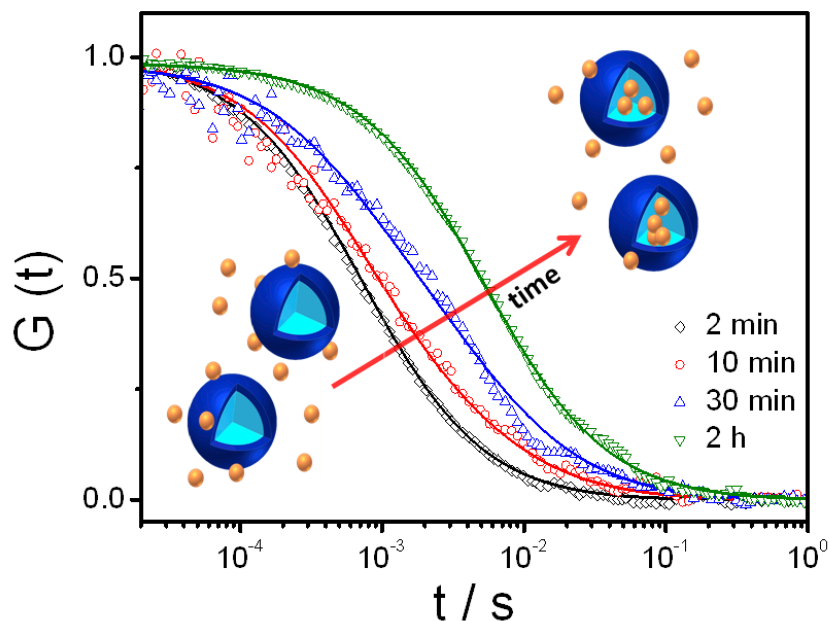


**Figure 5.25** Kinetics of the loading of PS nanoparticles into PDMS-*b*-PMOXA polymersomes probed by FCS. The experimental intensity autocorrelation functions (symbols) recorded by fluorescence correlation spectroscopy (FCS) at different times (2 min – 2 h) after mixing the PS ( $R_h = 16$  nm) nanoparticles and polymersomes solutions are represented (solid lines) by Equation 3.48, using either one diffusing component model (black and green curves) or two components model (red and blue).

Note that the latter is comparable to the radius obtained using PCS. From the relative contributions of the two decays to  $G(t)$ , the number ratio of these two species is estimated as 4 and 0.8 after 10 and 30 min loading, respectively. At the latest state the contribution from individual particles is hardly resolved mainly due to the much higher fluorescent brightness of the loaded vesicles in comparison to the free nanoparticles. Thus FCS is a suitable complementary technique to follow the kinetics of particle loading into polymersomes smaller than the probing area, and possibly to follow particle motion inside the polymeric vesicles for larger polymersome sizes.

## 5.4 Incorporation of Silica Nanoparticles into Polymersomes: Size and Concentration Effects

In this part a complex photon- and fluorescence-correlation spectroscopic studies of the uptake of nanosized SiO<sub>2</sub> nanoparticles by poly(dimethylsiloxane)-*b*-poly(2-methyloxazoline) vesicles allowing species selectivity are presented. It is revealed that the incorporation process can be controlled to a significant extent by changing nanoparticles size and concentration. Conditions for nanoparticle uptake and controlled filling are presented.

Adapted with permission from:

**Jaskiewicz, K.;** Larsen, A.; Schaeffel, D.; Koynov, K.; Lieberwirth, I.; Fytas, G.; Landfester, K.; Kroeger, A., Incorporation of Nanoparticles into Polymersomes: Size and Concentration Effects. *ACS nano* **2012**, *6*, 7254–7262

Copyright (2012) American Chemical Society

To investigate the size and concentration dependent incorporation of SiO<sub>2</sub> NPs performed by poly(dimethylsiloxane)-*block*-poly(2-methyloxazoline) (PDMS-*b*-PMOXA) polymersomes (with a *z*-average hydrodynamic radius  $R_{hP} = 110 \pm 3$  nm), a dilute aqueous vesicle solution with a polymer concentration of  $c_P = 4.5 \cdot 10^{-2}$  gL<sup>-1</sup> was mixed with four different sizes of SiO<sub>2</sub> NPs ( $R_{hNP} = (14 \pm 1)$  nm,  $(25 \pm 2)$  nm,  $(36 \pm 2)$  nm and  $(57 \pm 2)$  nm) at four different nanoparticle concentrations ( $c_{NP} = 0.05, 0.1, 0.15$  and  $0.2$  gL<sup>-1</sup>). Hence, the molar ratio of SiO<sub>2</sub> NPs to polymersomes is ranged between 1300:1 and 4:1. These systems were characterized using PCS, FCS, and cryo-TEM allowing species selectivity.

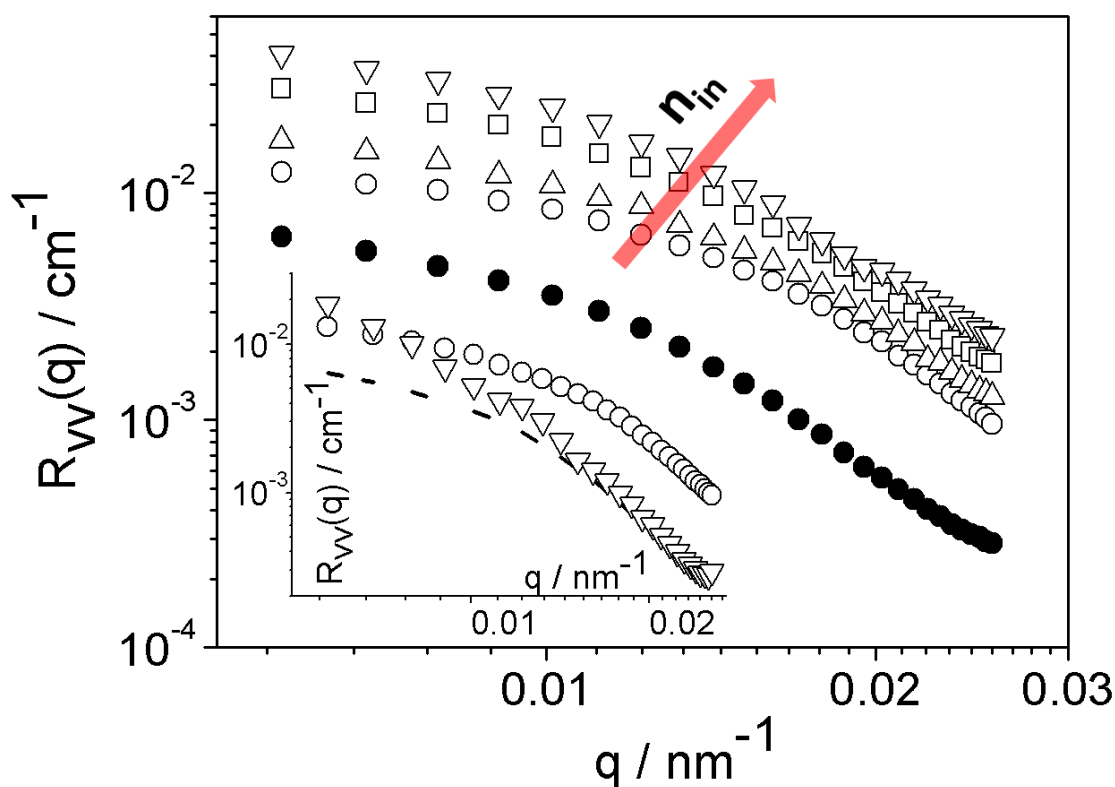


**Figure 5.26** Absolute Rayleigh intensity  $R_{vv}(q)$  as a function of the scattering wave vector  $q$  at  $T = 20$  °C for polymersomes in the absence (solid circles) and in the presence of SiO<sub>2</sub> nanoparticles with different sizes;  $R_{hNP} = 14$  nm (circles), 25 nm (triangles), 36 nm (squares) and 57 nm (inverse triangles) at  $c_{NP} = 0.2$  gL<sup>-1</sup> and  $c_P = 4.5 \cdot 10^{-2}$  gL<sup>-1</sup>. Inset:  $R_{vv}(q)$  as a function  $q$  at  $T = 20$  °C for the SiO<sub>2</sub>/polymersomes systems with  $R_{hNP} = 14$  nm (circles) and  $R_{hNP} = 57$  nm (inverse triangles) at  $c_P = 4.5 \cdot 10^{-2}$  gL<sup>-1</sup> and  $c_{NP} = 0.1$  gL<sup>-1</sup>; the dashed line represents polymersomes in the absence of NPs.

Due to the large optical contrast between water, polymersomes, and SiO<sub>2</sub> NPs the application of PCS to study the influences of different NP sizes and concentrations on the internalization process is optimal. The inner and outer refractive index of polymersomes formed in aqueous media ( $n_{\text{IN}} = n_0$ ) are equal to that of water ( $n_{\text{H}_2\text{O}} = 1.333$ ). Refractive index changes in the interior of the polymersomes ( $n_{\text{IN}}$ ) caused by an internalization of SiO<sub>2</sub> NPs with  $n_{\text{SiO}_2} = 1.45$ , which is different from that of pure water, result in strongly altered total light scattering intensity  $R_{\text{vv}}(q)$  of the investigated samples. Further, the combination of large optical contrast and a core-shell architecture of the polymersomes will render both the form factor  $P(q)$  and the scattering wave vector  $q$  dependence of the translational diffusion coefficient  $D(q)$ .<sup>21</sup>

#### 5.4.1 Threshold Concentration

The influence of the NP size on the experimental  $R_{\text{vv}}(q)$  as a function of  $q$  at a constant nanoparticle concentration of  $c_{\text{NP}} = 0.2 \text{ gL}^{-1}$  is depicted in *Figure 5.26*; the molar ratio of SiO<sub>2</sub> NPs to polymersomes in these experiments ranges from 1260:1 for the smallest ( $R_{\text{h NP}} = 14 \text{ nm}$ ) to 16:1 for the largest NPs ( $R_{\text{h NP}} = 57 \text{ nm}$ ). The light scattering intensity for all NP containing samples is much higher than the sum of the individual component contributions (see *Figure 5.26*), indicating strong interactions of NPs with polymersomes. In comparison to the scattering intensity of solutions containing polymeric vesicles in the absence of NPs i.e., empty vesicles,  $R_{\text{vv}}(q)$  of SiO<sub>2</sub>/polymersome samples increase with increasing NPs sizes. The overall sizes of the resulting objects remain almost constant as indicated by the similar shape of the  $R_{\text{vv}}(q)$  patterns. Since the contribution of the silica NPs to the total scattering intensity at low  $q$  values is negligible (see 5.2.2.2), the observed increase of the forward scattering  $R_{\text{vv}}(q \rightarrow 0)$  is associated to increasing values of  $n_{\text{IN}}$  due to NP internalization into the interior of the polymersomes as illustrated by the red arrow in *Figure 5.26*. This is a fortuitous because the  $z$ -average hydrodynamic radius  $R_{\text{h P}}$  and the size polydispersity of the SiO<sub>2</sub>/polymersome systems reveal

only moderate changes.<sup>43</sup> In fact the pattern of  $D(q)$  (see *Figure 5.27* and *Figure 5.31* below) obtained from the experimental concentration relaxation functions  $C(q, t)$  in PCS experiments indicates no significant change in the value of  $R_{h, P}$  and polydispersity (PD) compared to the solutions containing empty vesicles. Therefore, mainly the increase of  $n_{IN}$ , relative to that of pure water, boosts the intensity  $R_{vv}(q \rightarrow 0)$  as confirmed by fit model calculations of  $P(q)$  with increasing  $n_{IN}$  (described below).

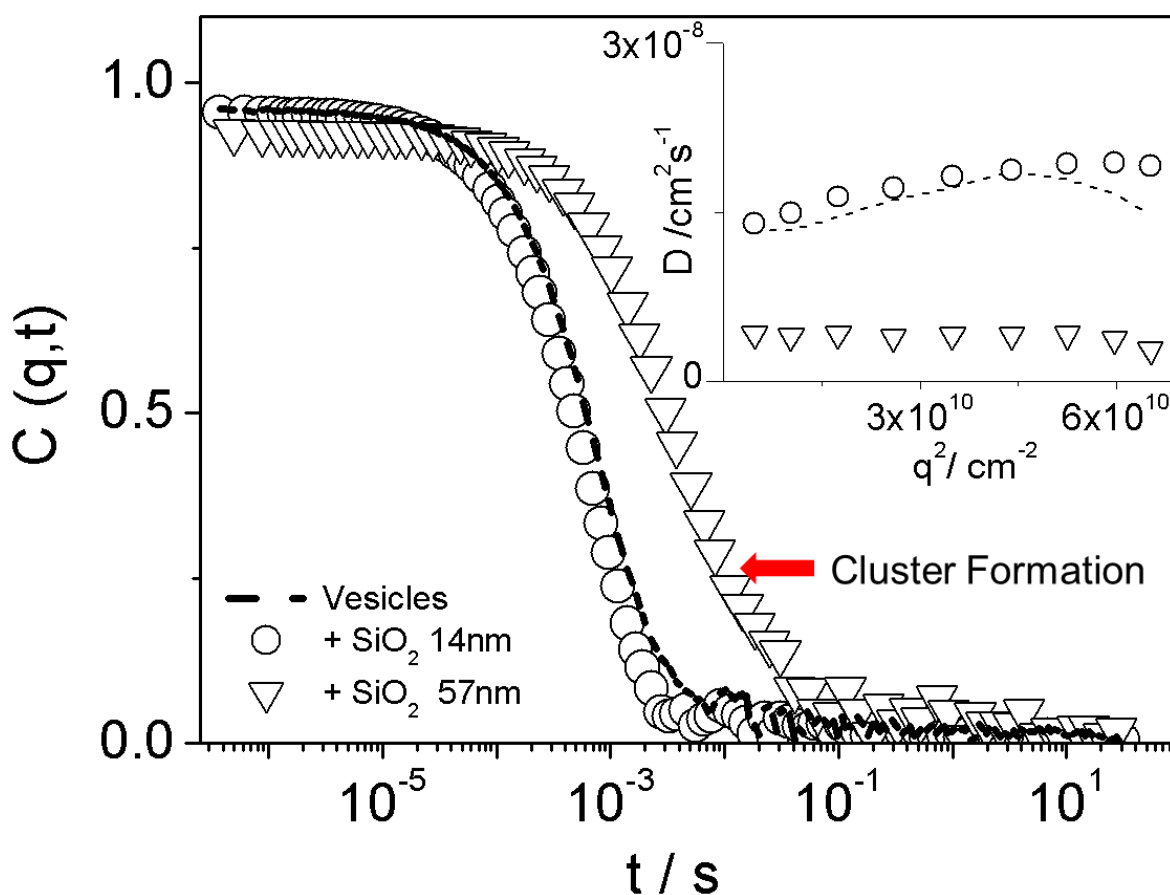


**Figure 5.27** Relaxation functions  $C(q, t)$  for the concentration fluctuations in SiO<sub>2</sub>/polymersomes systems with  $R_{h, NP} = 14$  nm (circles) and 57 nm (inverse triangles) at  $c_{NP} = 0.1$  gL<sup>-1</sup> and  $c_p = 4.5 \cdot 10^{-2}$  gL<sup>-1</sup> for  $q = 2.4 \cdot 10^{-2}$  nm<sup>-1</sup> at  $T = 20$  °C along with the translational diffusion  $D(q)$  vs  $q^2$  shown in the inset. The dashed lines represent polymersomes in the absence of NPs and the arrow points at the  $C(q, t)$  yielding the slow translational diffusion (inverse triangles) of big clusters.

The inset of *Figure 5.26* presents the increase of  $R_{vv}(q)$  for the  $\text{SiO}_2$  ( $R_{h\text{ NP}} = 14$  nm)/polymersomes system at  $c_{\text{NP}} = 0.1 \text{ gL}^{-1}$  while the intensity pattern of the polymersome solution with large  $\text{SiO}_2$  NPs ( $R_{h\text{ NP}} = 57$  nm) at the same  $c_{\text{NP}}$  reveals a different shape, which implies scattering from larger moieties. This notion is corroborated by the relaxation function  $C(q, t)$  of *Figure 5.27* displaying a single translational diffusion  $D(q)$  (inverse triangles) which is significantly slower than both empty polymersomes and vesicles occupied by the small silica particles. The experimental  $C(q, t)$  were represented by a stretched exponential function with a shape parameter (see chapter 3.6.1)  $\beta_{\text{KWW}} = 0.95$  and  $D(q) = \Gamma(q)/q^2$  (see inset in *Figure 5.27*) obtained from the relaxation rate  $\Gamma(q)$ . Hence the size of the diffusing objects increases significantly in case of  $\text{SiO}_2$  ( $R_{h\text{ NP}} = 57$  nm)/polymersomes with  $c_{\text{NP}} = 0.1 \text{ gL}^{-1}$  due to cluster formation. A decrease of  $c_{\text{NP}}$  down to  $0.05 \text{ gL}^{-1}$  causes agglomeration in the  $\text{SiO}_2$ /polymersome mixture not only with  $R_{h\text{ NP}} = 57$  nm but also with  $R_{h\text{ NP}} = 36$  nm (not shown) at  $\text{SiO}_2$ /polymersomes ratio 4:1 and 16:1 respectively.

This pertinent observation suggests the existence of a threshold particle concentration above which particle incorporation can occur. Such a threshold concentration is probably related to the surface area ratio between polymersomes and NPs<sup>44</sup> necessary for a successful particle adhesion to the outer vesicle membrane and further internalization. Changing  $c_{\text{NP}}$  results in the variation of the overall nanoparticles surface area (single nanoparticle surface area is constant). Estimation of the surface area ratio between polymersomes and NPs suggests to the conclusion that the overall surface area of the latter should be at least two times higher (see *Table 5.4*). For the two smallest NP sizes ( $R_{h\text{ NP}} = 14$  nm and 25 nm), the calculated threshold particle concentration should be less than the lowest investigated concentration of  $c_{\text{NP}} = 0.05 \text{ gL}^{-1}$ ; rough estimates amount to  $0.025 \text{ gL}^{-1}$  and  $0.04 \text{ gL}^{-1}$  respectively.

**Table 5.4** Polymersomes to nanoparticles surface area ratio calculations at four nanoparticles concentrations. Precipitation was observed for the samples marked in red.

Particle	Concentration	Number of	Polymersomes/Particles	Estimated
<b>SiO<sub>2</sub></b> <b>R<sub>h</sub> = 14nm</b>	0.05	280	1:4	C ≤ 0.025
	0.1	560	1:8	
	0.15	840	1:12	
	0.2	1260	1:16	
<b>SiO<sub>2</sub></b> <b>R<sub>h</sub> = 25 nm</b>	0.05	50	1:2.5	C ≤ 0.04
	0.1	100	1:5	
	0.15	150	1:7.5	
	0.2	200	1:10	
<b>SiO<sub>2</sub></b> <b>R<sub>h</sub> = 36 nm</b>	0.05	16	1:1.65	C ≤ 0.07
	0.1	32	1:3.3	
	0.15	48	1:4.95	
	0.2	64	1:6.6	
<b>SiO<sub>2</sub></b> <b>R<sub>h</sub> = 57 nm</b>	0.05	4	1:1	C ≤ 0.1
	0.1	8	1:2	
	0.15	12	1:3	
	0.2	16	1:4	

### 5.4.2 Concentration Dependence

Figure 5.28 shows the experimental total light scattering intensity  $R_{vv}(q)$  as a function of the scattering wave vector  $q$  for a SiO<sub>2</sub> ( $R_{h\text{ NP}} = 14\text{ nm}$ ) /polymersome system at three different NP concentrations at a constant polymer concentration. The forward scattering intensity  $R_{vv}(q \rightarrow 0)$  increases with  $c_{\text{NP}}$  while the scattering  $R_{vv}(q)$  patterns are similar and distinct from the empty polymersomes (at high  $q$ -values). The increase of the refractive index in the interior of polymersomes  $n_{\text{IN}}$  (above the value of water) as a result of particle incorporation is the main parameter accounting for the forward scattering provided that the polymersome size remains

insensitive to  $c_{\text{NP}}$ . A concurrent representation of the  $R_{\text{VV}}(q)$  pattern intensity and the translational diffusion  $D(q)$  is obtained by the corresponding theoretical expressions<sup>21</sup> (see Equation 3.39) and calculated values of the polymersome radius,  $R_n$ , apparent weight-average molar mass,  $M_{\text{w app}}$ , of the objects, system polydispersity, and  $n_{\text{IN}}$  are listed in Table 5.5. Assuming a linear dependence of  $n_{\text{IN}}(\phi)$  on particle volume fraction (in the interior of a polymersome)  $\phi$ , the number  $x$  of incorporated nanoparticles increases from about 7 at  $c_{\text{NP}} = 0.1 \text{ gL}^{-1}$  to 11 for  $c_{\text{NP}} = 0.2 \text{ gL}^{-1}$  in the initial solution.

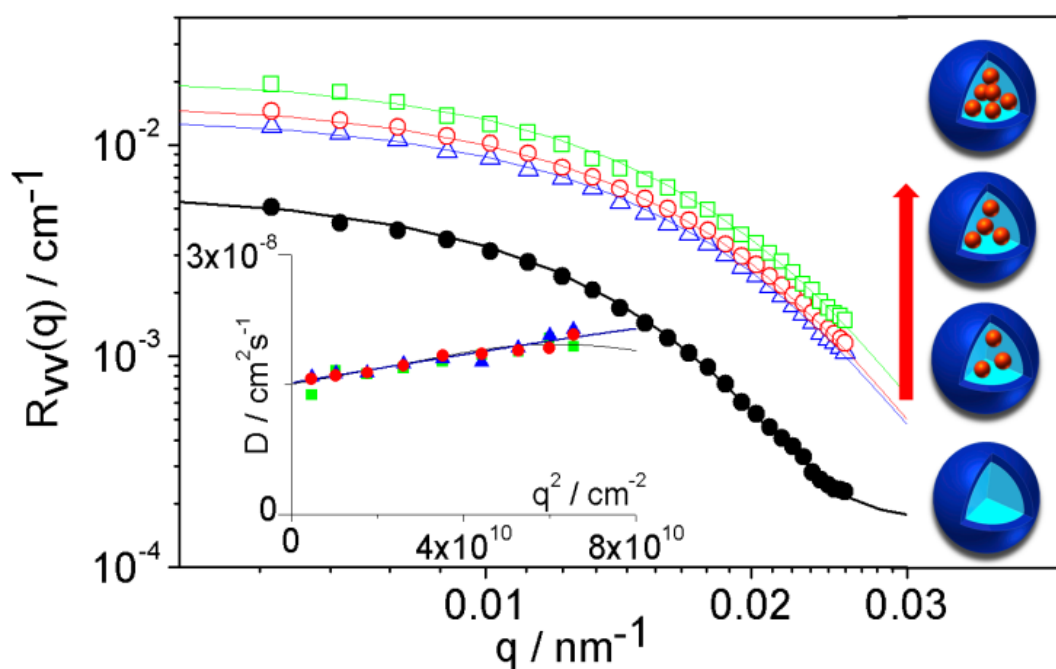


**Figure 5.28** Absolute Rayleigh intensity  $R_{\text{VV}}(q)$  pattern at  $T = 20 \text{ }^\circ\text{C}$  for polymersomes in the absence of NPs (solid black circles) and the  $\text{SiO}_2$  ( $R_{\text{h NP}} = 14 \text{ nm}$ )/polymersome system at three different NP concentrations;  $c_{\text{NP}} = 0.1 \text{ gL}^{-1}$  (empty blue triangles),  $0.15 \text{ gL}^{-1}$  (empty red circles),  $0.2 \text{ gL}^{-1}$  (empty green squares) represented by the corresponding theoretical expressions (solid lines), (see Equation 3.39). The increasing nanoparticle population inside the polymersomes with  $c_{\text{NP}}$  is schematically shown for the four systems. The inset depicts the corresponding translational diffusion coefficients  $D(q)$  vs  $q^2$  for the three different  $\text{SiO}_2$ /polymersome systems (solid symbols) and polymersomes in the absence of NPs (black line).

Note that maximum filling of the particular polymersomes with  $\text{SiO}_2$  ( $R_{\text{h NP}} = 14$  nm) would correspond to  $x = 43$  incorporated particles assuming individual incorporation of particles; calculation based on group incorporation would lead to higher number of incorporated particles (see *Figure 5.32* below). In fact, cryo-TEM imaging<sup>21</sup> (*Figure 5.32*) and recent simulations<sup>45</sup> suggest incorporation of clusters of individual particles in some cases; PCS cannot distinguish between the two cases. *Figure 5.30 and Table 5.6* shows analog data for a  $\text{SiO}_2$  ( $R_{\text{h NP}} = 25$  nm) /polymersome system at three different NP concentrations at a constant polymer concentration.

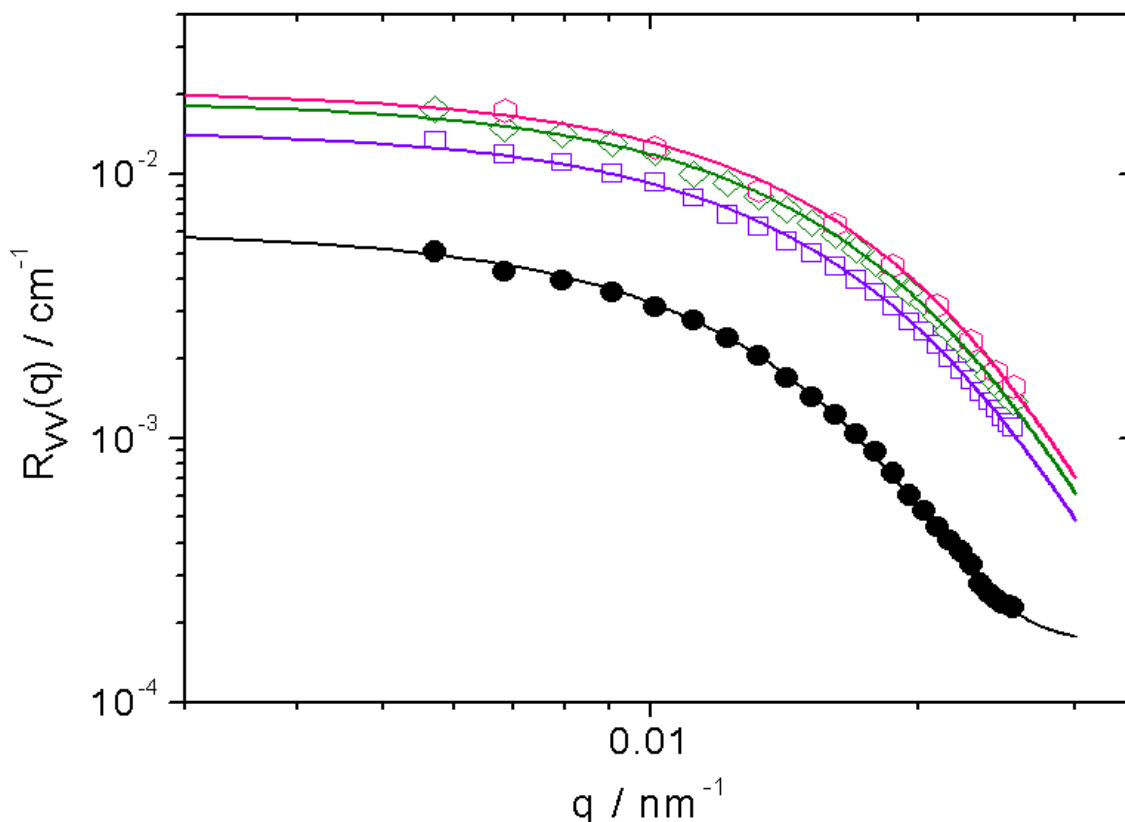


**Figure 5.29** Absolute Rayleigh intensity  $R_{\text{vV}}(q)$  as a function of  $q$  at  $T = 20$  °C for empty polymersomes (empty black squares) and  $\text{SiO}_2$ /polymersome systems with  $R_{\text{h NP}} = 25$  nm at three different concentration of particles;  $c_{\text{NP}} = 0.1$  gL<sup>-1</sup> (red empty circles), 0.15 gL<sup>-1</sup> (green empty triangles), 0.2 gL<sup>-1</sup> (blue empty inverse triangles) represented by the corresponding theoretical expressions (solid lines).

The incorporation of the particles is associated with shrinking of the polymersomes as indicated by the value of their radii listed in *Table 5.5*. In order to engulf and encapsulate nanoparticles membrane material is consumed.<sup>24</sup> The observed shrinking of about 18% is less than the estimated value of 24%, based on the average number of the incorporated nanoparticles. This deviation can be partially attributed to the polydispersity (PDI in *Table 5.5*), not uniform filling and probably bilayer stretching/vesicle swelling.<sup>46</sup> Internalization of the small SiO<sub>2</sub> beads occurs above 0.05 gL<sup>-1</sup> and their incorporation by the present polymersomes depends on the nanoparticle concentration in the bulk solution. Particles with  $R_{h\ NP} = 25$  nm retain this internalization behavior.

**Table 5.5** Characteristics of polymersomes in the absence and presence of SiO<sub>2</sub> NPs with  $R_{h\ NP} = 15$  nm

	Polymer-somes	SiO <sub>2</sub> /polymersome		
$c_{NP} / \text{gL}^{-1}$	0	0.1	0.15	0.2
$R_{vv}(q \rightarrow 0) \cdot 10^3 / \text{cm}^{-1}$	6.35	14.24	11.64	21.6
$M_{w\ app} \cdot 10^{-9} / \text{gmol}^{-1}$	3.3	1.7	1.8	1.8
$R_n / \text{nm}$	110	87	89	89
<b>PDI</b>	1.07	1.13	1.13	1.13
$n_{IN}$	1.333	1.367	1.373	1.382
$x$	0	7	9	11

**Table 5.6** Characteristics of polymersomes in the absence and presence of SiO<sub>2</sub> NPs with  $R_{h\ NP} = 25$  nm

	SiO <sub>2</sub> /polymersome		
$c_{NP} / \text{gL}^{-1}$	0.1	0.15	0.2
$R_{vv}(q \rightarrow 0) \cdot 10^3 / \text{cm}^{-1}$	16.96	24	28.1
$M_{w\ app} \cdot 10^{-9} / \text{gmol}^{-1}$	1.6	1.8	1.9
$R_n / \text{nm}$	87	89	91
<b>PDI</b>	1.125	1.125	1.125
$n_{IN}$	1.367	1.386	1.393
$x$	3	5	6

### 5.4.3 Size Dependence

For the SiO<sub>2</sub>/polymersome systems, samples with nanoparticle sizes of  $R_{h\text{ NP}} = 36$  nm and 57 nm were prepared; interactions are observed above the threshold particle concentrations  $c_{\text{NP}} > 0.05$  gL<sup>-1</sup> and 0.1 gL<sup>-1</sup>, respectively. Above these critical concentrations, the mixtures exhibit  $R_{\text{v}}(q)$  beyond the sum of the individual components contributions (as described above).

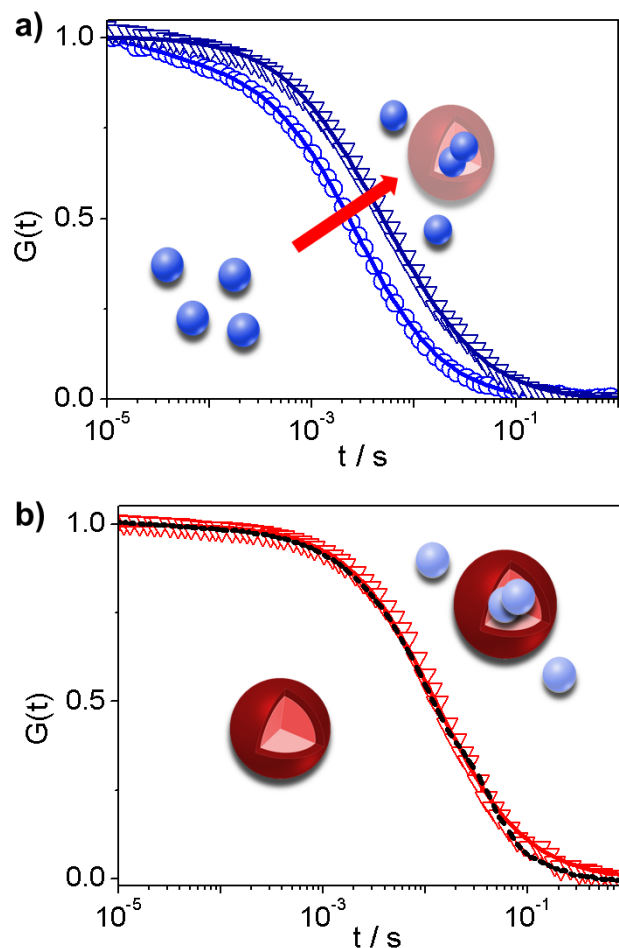


**Figure 5.30** Normalized fluorescence intensity autocorrelation functions  $G(t)$  for **a** distinctly labeled SiO<sub>2</sub> nanoparticles with  $R_{h\text{ NP}} = 57$  nm (blue symbols) and **b** polymersomes (red symbols) recorded before (circles in **a** and dotted black line in **b**) and after their mixing (inverse triangles). Solid lines in **a** represent fits of Equation 3.48 to the experimental  $G(t)$  assuming either a single diffusion ( $i = 1$ ) before mixing (circles) or a double diffusion ( $i = 2$ ) after mixing whereas the solid red line in **b** denotes a single diffusion ( $i = 1$ ) fit to the  $G(t)$  (inverse triangles) for the SiO<sub>2</sub>/labeled polymersome solution whereas the dotted black line represent  $G(t)$  of empty vesicles.

A peculiarity of these larger particles, however, is the strong contribution to  $R_{vv}(q)$  at high  $q$  values and consequently to the relaxation function  $C(q, t)$ . For the investigation of the particle incorporation of these systems, both contributions should be properly accounted in order to enable an unambiguous discrimination between filled (NPs incorporated) versus decorated vesicles (NPs attached to outer polymersome surface).<sup>21</sup> An independent information on nanoparticles internalization would therefore facilitate the analysis of  $R_{vv}(q)$  and  $D(q)$  of the PCS experiment.

Fluorescence correlation spectroscopy is utilized by fluorescent labeling both interacting species, SiO<sub>2</sub> NPs ( $R_{h\ NP} = 57$  nm) and polymersomes. In a FCS experiment, the intensity fluctuations caused by the tracer diffusion of the fluorescent species through the focus of a confocal microscope are monitored and recorded. The correlation analysis of these fluctuations can yield information on both the size ( $R_h$ ) and the concentration of the labeled species from the decay of the autocorrelation curve (diffusion time) and its plateau value at short lag times, respectively. Yet, labeling polymersomes and SiO<sub>2</sub> NPs with different fluorescent dyes and using two excitation lasers and appropriate emission filters (see Chapter 4) permits selective probing through the utilization of the two FCS detection channels. The “blue” channel monitors only the fluorescent signal originating from the labeled SiO<sub>2</sub> NPs while the “red” channel detects the signal from the labeled polymersomes. *Figure 5.30* presents fluorescence intensity autocorrelation curves  $G(t)$  recorded in both channels before (circles) and after (inverse triangles) mixing polymersomes with SiO<sub>2</sub> beads at  $c_P = 4.5 \cdot 10^{-2}$  gL<sup>-1</sup> and  $c_{NP} = 0.2$  gL<sup>-1</sup>. As can be seen in *Figure 5.30b*, the correlation function for the polymersomes diffusion practically does not change upon mixing indicating either the absence of interactions or particle incorporation into the polymersomes.

Indeed, if the nanoparticles were attached to the surface or trapped in the hydrophobic bilayer their relatively large size would cause a change in the overall diffusion coefficient of the polymersomes and therefore shift the decay of  $G(t)$  to longer times. In the absence of such shift, the  $G(t)$  recorded in the “red” channel for labeled polymersomes both with (inverse triangles) and without (solid red line in *Figure 5.30b*) nanoparticles can be fitted with *Equation 3.48* yielding  $R_{hP} = 145 \pm 15$  nm for the polymersome hydrodynamic radius. At a first sight, the insensitivity of  $G(t)$  to the presence of  $\text{SiO}_2$  suggests robust polymersomes average size.

Complementary information on the polymersome/NPs interactions is obtained from the fluorescence correlation function  $G(t)$  of the labeled  $\text{SiO}_2$  NPs seen in the “blue” FCS channel. Prior to their mixing with the polymersomes,  $G(t)$  is well represented by a single diffusive decay in eq. 2 (with  $i = 1$ ) yielding  $R_{hNP} = 55 \pm 5$  nm for the  $\text{SiO}_2$  NPs in agreement with the PCS experiment. After mixing with the polymersomes, the experimental  $G(t)$  shifts significantly towards longer lag times (blue inverse triangles) and deviates from a single diffusion in *Equation 3.48*, instead,  $G(t)$  is well represented *Equation 3.48* assuming two diffusive decays ( $i = 2$ ). The first fast decay represents the freely diffusing, non-interacting  $\text{SiO}_2$  beads, whereas the slow decay corresponds to the diffusion of much slower species with  $R_h = 155 \pm 25$  nm being very close to the value for the polymersomes. Since only labeled  $\text{SiO}_2$  NPs are probed, the slow process in  $G(t)$  demonstrates internalization of the large  $\text{SiO}_2$  particles ( $R_{hNP} = 57$  nm). Yet the relative contribution of the slow decay, normalized to the inherent fluorescence intensities of the pure labeled solutions confirms this particle incorporation amounting to about two  $\text{SiO}_2$  NPs per polymersome.

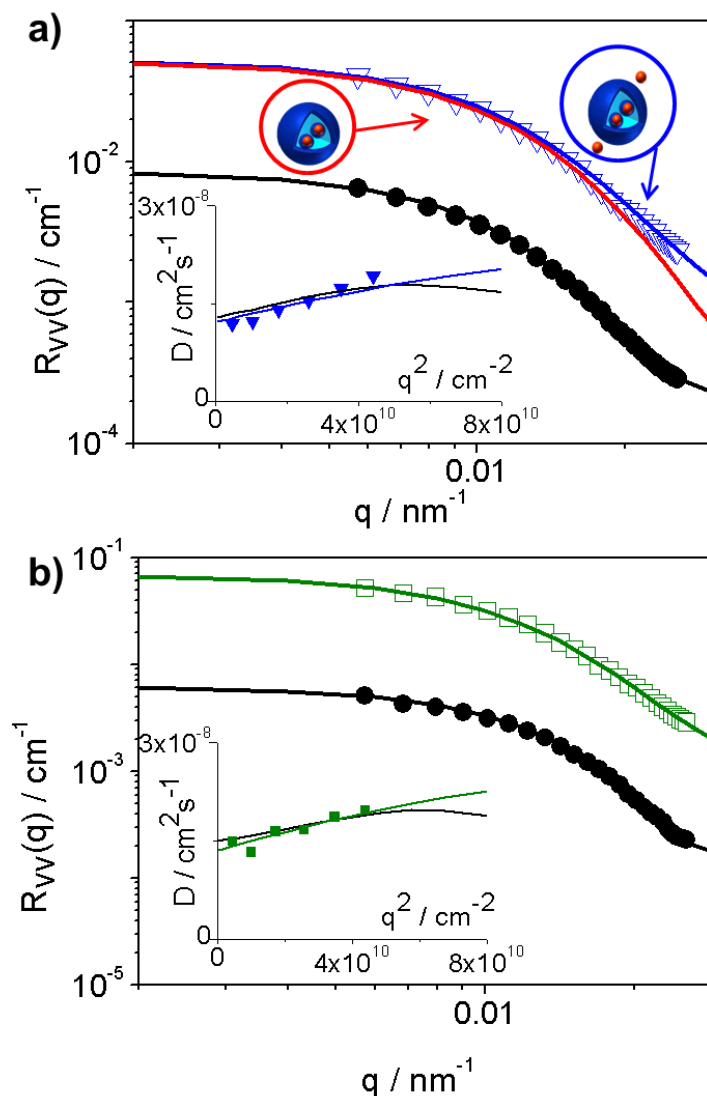


**Figure 5.31** Absolute Rayleigh intensity  $R_{VV}(q)$  at  $T = 20 \text{ }^\circ\text{C}$  of polymersomes in the absence of NPs (solid black circles) and the  $\text{SiO}_2$ /polymersome systems with **a.**  $R_{h, \text{NP}} = 57 \text{ nm}$  (inverse triangles) and **b.**  $R_{h, \text{NP}} = 36 \text{ nm}$  (squares) at  $c_{\text{NP}} = 0.2 \text{ gL}^{-1}$  represented by the corresponding theoretical expressions (solid lines) along with the corresponding translational diffusion coefficient  $D(q)$  vs  $q^2$  (insets). The red line in **a** denotes the contribution of the filled polymersomes only whereas the total  $R_{VV}(q)$  includes also the scattering from the free NPs as schematically shown in the left panel of the Figure.

We turn now to the PCS information on large particle internalization addressed in *Figure 5.31*. Both  $R_{VV}(q)$  and  $D(q)$  patterns for  $\text{SiO}_2$  ( $R_{h, \text{NP}} = 57 \text{ nm}$ )/polymersomes are well represented for an incorporation ratio 2:1 (red solid line) including the contribution of free particles in

solution (blue solid lines) as schematically shown in Figure 5.31a. The necessity of a two component fit to  $R_{\text{vv}}(q)$  and  $D(q)$  is also implied by the fast diffusion at the highest  $q$  values (not included in the inset to Figure 5.31a) due the contribution of the free SiO<sub>2</sub> NPs to the scattering event. For comparison, Figure 5.31b shows the experimental  $R_{\text{vv}}(q)$  and  $D(q)$  for the same SiO<sub>2</sub>/polymersomes system with  $R_{\text{h NP}} = 36$  nm at  $c_{\text{NP}} = 0.2$  gL<sup>-1</sup>. Here, the contribution of the free SiO<sub>2</sub> beads to the experimental  $R_{\text{vv}}(q)$  and  $D(q)$  is smaller but still significant. The characteristics of the internalization process for these two nanoparticles are summarized in Table 5.7.

The NP loading incorporation rate decreases compared to the smallest nanoparticle (see Table 5.5). For comparison, complete filling of the interior of the polymersome would correspond to  $x = 7$  for  $R_{\text{h NP}} = 36$  nm and  $x = 3$  for  $R_{\text{h NP}} = 57$  nm. In this context it should be mentioned that with further increase of  $c_{\text{NP}}$  above the concentration necessary for the maximum filling of polymersomes no more changes of the systems are observed (no polymersomes rapture).

**Table 5.7** Characteristics of polymersomes in the absence and presence of SiO<sub>2</sub> NPs with  $R_{\text{h NP}} = 36$  nm and 57 nm.

	SiO <sub>2</sub> /Polymersomes	
	36	57
$R_{\text{h NP}} / \text{nm}$	36	57
$c_{\text{NP}} / \text{gL}^{-1}$	0.2	0.2
$R_{\text{vv}}(q \rightarrow 0) \cdot 10^3 / \text{cm}^{-1}$	44.7	83.2
$M_{\text{w app}} \cdot 10^{-9} / \text{gmol}^{-1}$	2.0	3.1
$R_{\text{n}} / \text{nm}$	93	100
<b>PDI</b>	1.2	1.17
$n_{\text{IN}}$	1.396	1.417
<b>x</b>	3 - 4	2 - 3

The two correlation spectroscopic techniques demonstrate that NPs reside inside the polymersomes but cannot provide information on the internal structure; in an indirect way (through the small size shrinkage) supports NP wrapping with polymeric bilayer. Alternatively, cryo-TEM imaging yields direct snap shots of a relative small number of individual structures. The poor statistics can be, however, compensated by precise imaging with nanometer scale resolution. *Figure 5.32* shows cryo-TEM images of the polymersomes containing SiO<sub>2</sub> NPs with two different sizes.

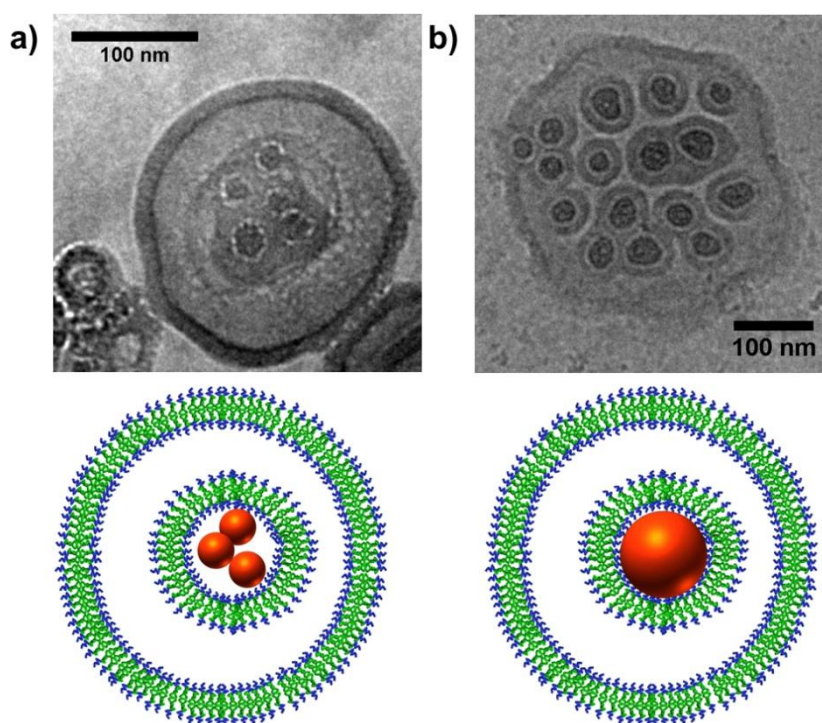


**Figure 5.32** Cryo-TEM micrographs of incorporated SiO<sub>2</sub> nanoparticles into PDMS-*b*-PMOXA polymersomes. **a.** Internalized groups of SiO<sub>2</sub> NPs with  $R_{h\text{ NP}} = 14$  nm and **b.** internalized single SiO<sub>2</sub> NPs with  $R_{h\text{ NP}} = 25$  nm. The two schematic representations illustrate the different internalization mechanisms.

Both types of particles are internalized into PDMS-*b*-PMOXA vesicles. The incorporation mechanism derived from PCS and FCS results (*vide supra*) includes the complete engulfment and

wrapping of NPs (see *Figure 5.32, 5.33*). The number-average diameter of the wall thickness of nanoparticles supported bilayer, as obtained by statistical analysis of several TEM micrographs, confirms the value of the membrane thickness of polymersomes ( $\approx 16$  nm). Albeit these two systems display very similar  $R_{vv}(q)$  and  $D(q)$ , *Figure 5.32a* and *5.32b* reveal size dependent internalization mechanisms.  $\text{SiO}_2$  NPs with  $R_{h \text{ NP}} = 14$  nm were incorporated as clusters of particles rather than single wrapped particles which appears to be the case for the larger  $\text{SiO}_2$  nanoparticles ( $R_{h \text{ NP}} = 25$  nm). For the larger sized particles the cryo-TEM preparations failed despite several repetitions. Only undefined collapsed objects together with the silica nanoparticles were found. This might be attributed to decreased vesicle stability after uptake of those larger silica particles.

Nanoparticle uptake by cells was very recently addressed by dissipative particle dynamics (DPD) simulation. It has been shown that the mechanism of nanoparticle incorporation depends on the size, membrane tension, and nanoparticles concentration.<sup>45</sup> Small neighboring particles might cluster prior to internalization in order to reduce curvature energy of the membrane. An increase of the nanoparticle size would weaken the curvature mediated interactions since large nanoparticle sizes reduce the perturbation of the membrane curvature.

Thus the delicate balance of interactions renders different assemblies for small and large nanoparticles. These simulation results, although designed for cellular uptake of nanoparticles bear strong resemblance with the cryo-TEM images in *Figure 5.32* for the present artificial polymeric model system. The different properties of lipid and polymeric membranes e. g. in the thickness, however, render a direct comparison of nanoparticles ambiguous. Nevertheless, comparison is justified in view of the importance of surface curvature. Moreover, cryo-TEM images for the smaller silica nanoparticles ( $R_{h \text{ NP}} = 14$  nm and 25 nm) were taken at about eight times higher concentration (but same ratio of NPs to polymersomes) than investigated by PCS

and FCS. Due to the different solution compositions the quantitative comparison of the population of the incorporated particles observed in PCS and cryo-TEM is not straightforward.

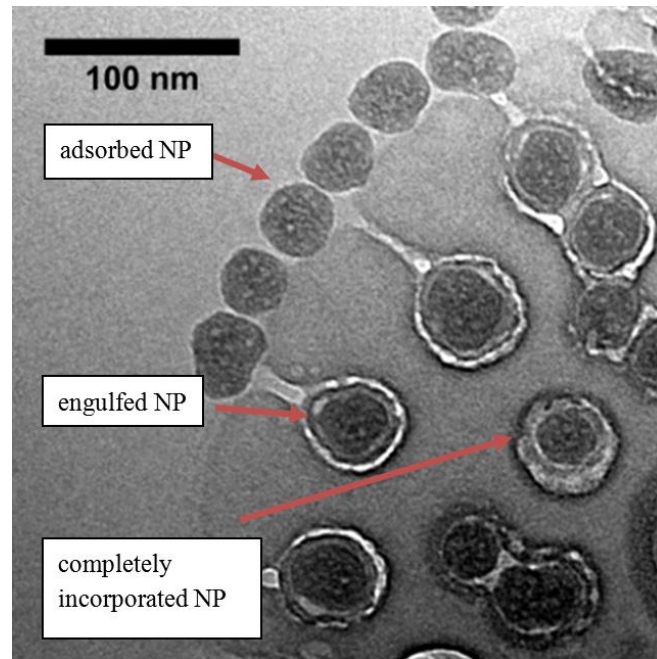


**Figure 5.33** Cryo-TEM micrograph of SiO<sub>2</sub>/polymersome systems with  $R_{h\text{ NP}} = 25$  nm recorded on sample frozen 6 min after addition of NPs to polymersomes suspension, different states of incorporation observable as marked by arrows.

### 5.4.3.1 Size dependent nanoparticles uptake by polymeric membranes: theoretical simulations

Simulations presented in this section were performed by Mingyang Hu under supervision of Prof. Marcus Deserno (**Carnegie Mellon University, Department of Physics**)

Theoretical simulations of size dependent uptake of nanoparticles by polymeric vesicles were performed using solvent-free coarse-grained lipid membrane model (schematically shown of *Figure 5.34*). Due to the purpose of this model, the bending stiffness of the bilayer is set to  $20 k_B T$ . This is about 1 - 2 orders of magnitudes softer than the one of the diblock copolymer vesicle (see Chapter 5.2.1), harder however than lipid bilayer. Thus, instead of matching the absolute energies, the focus was put on the relative ratio between two energy contributions: the bending energy and adhesion energy. Note that since the membrane is soft, the fluctuation of the vesicle is more significant than in real experiments.

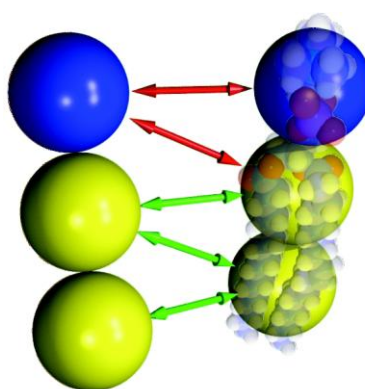


**Figure 5.34** Schematic of the Cooke model. The blue beads are hydrophilic head groups, while the yellow ones are hydrophobic tails. In addition to excluded volume repulsion (red arrows), an attractive potential (yellow arrows) is applied between tail beads.

As witnessed on *Figure 5.35*, particles below certain threshold size can be incorporated only as a group. At the beginning of this simulation, six nanoparticles of diameter  $b_{\text{NPs}} = 30$  nm each are placed in three clusters near a vesicle with diameter  $b_{\text{ves}} = 200$  nm. These three clusters contain one, two, and three nanoparticles, respectively. After a long simulation run, the two clusters that contain more than one nanoparticle were engulfed into the vesicle, while the single nanoparticle remained outside. Each incorporated cluster is surrounded by peanut-like shape bilayer. In order to cross the bilayer via membrane wrapping nanoparticle has to curve the bilayer. This would cost a bending energy regardless of the size of the nanoparticle. The total adhesion energy between the particle and vesicle however, is proportional to the contact area. Thus, for a given size of the NPs, and consequently a limited contact area for each individual nanoparticle, there is a range of the adhesion energy between single particle and bilayer, for which a single nanoparticle cannot accumulate enough energy to bend the bilayer. This could be possible if few of them act cooperatively creating clusters having higher contact area with the vesicle.

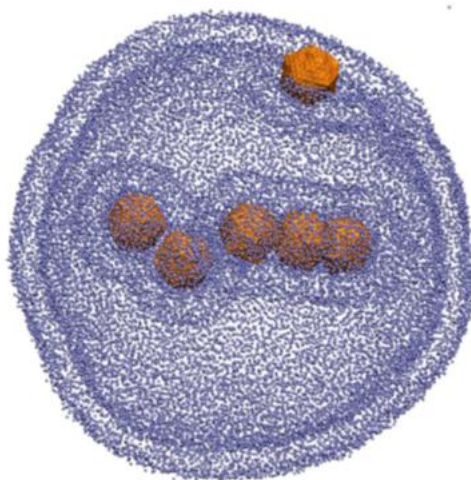


**Figure 5.35** Final snapshot of a simulation with a vesicle  $b_{\text{ves}} = 200$  nm and six nanoparticles  $b_{\text{NPs}} = 30$  nm. Only the head beads of the lipids are shown for clarity. Except for the single nanoparticle on the top, all other nanoparticles enter the vesicle.

Nanoparticle of bigger size which contact area with the vesicle is an equivalent to the one of clustered small particles should be able to enter the vesicle individually. Simulations of the same adhesion but with larger nanoparticle diameter  $b_{\text{NPs}} = 50$  nm confirm the uptake of single nanoparticles (see *Figure 5.36*).

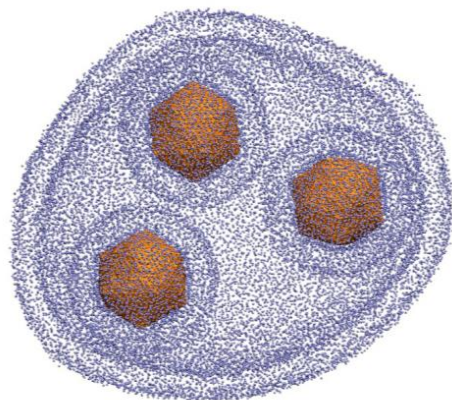


**Figure 5.36** Final snapshot of a simulation with a 200 nm diameter vesicle and three 50 nm diameter NPs. Only the head beads of the lipids are shown for clarity. Both of a single NP and a two-NP pair went into the vesicle.

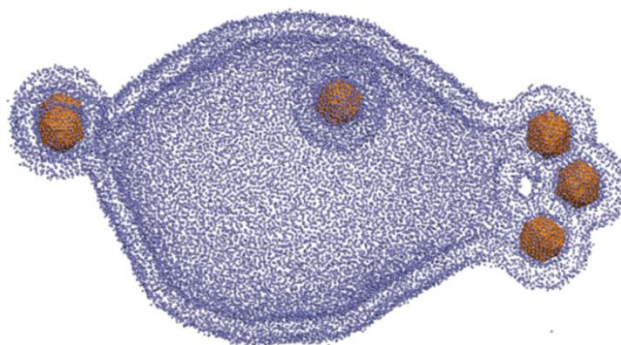


**Figure 5.37** One snapshot of a simulation with a 200 nm diameter vesicle and six 30 nm diameter NPs. Only the head beads of the lipids are shown for clarity. While a single NP now is able to get into the vesicle (the one in the middle), the other NPs in form of clusters are first wrapped by the vesicle, then start to stick outwards. Note there are two NPs on the left overlapping with each other because of the perspective.

An increase of the attraction between particle and bilayer leads to some unexpected behavior. Particles are first embedded inside a pocket-like structure but instead being pinched-off inside the vesicles they are pinched-off outside the vesicle, behaving like “exocytosis”. The ongoing simulation shown in *Figure 5.37* is not finished yet, but by watching the evolution of the system, it has become clear that the vesicle wants to pinch off those pockets.

Following the rate of change in the total adhesion energy between particles and the vesicle, one can predict the periods during which there are NPs being adsorbed onto the vesicle (*Figure 5.38*).

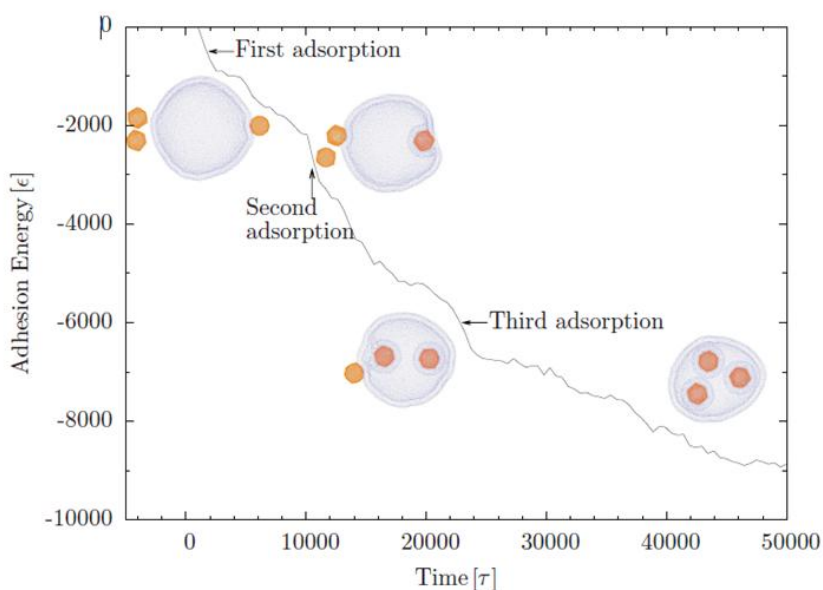


**Figure 5.38** Adhesion energy as function of time. Snapshots were taken from the simulation shown in *Figure 5.36*.

These preliminary simulations are in good agreement with the experimental results which revealed cooperative uptake of  $\text{SiO}_2$  nanoparticles with diameter  $b_{\text{NPs}} = 30$  nm and individual uptake of particles with  $b_{\text{NPs}} = 50$  nm (see *Figure 5.32*).

## 5.5 References

1. Discher, D. E.; Eisenberg, A., Polymer vesicles. *Science* **2002**, *297*, 967.
2. Taubert, A.; Napoli, A.; Meier, W., Self-assembly of reactive amphiphilic block copolymers as mimetics for biological membranes. *Curr. Opin. Cell Biol.* **2004**, *8*, 598-603.
3. Lipowsky, R.; Sackmann, E., *Structure and dynamics of membranes: From cells to vesicles*. Elsevier Science: **1995**.
4. Fery, A.; Weinkamer, R., Mechanical properties of micro- and nanocapsules: Single-capsule measurements. *Polymer* **2007**, *48*, 7221-7235.
5. Munro, J. C.; Frank, C. W., Adsorption of lipid-functionalized poly (ethylene glycol) to gold surfaces as a cushion for polymer-supported lipid bilayers. *Langmuir* **2004**, *20*, 3339-3349.
6. Morigaki, K.; Schönherr, H.; Frank, C. W.; Knoll, W., Photolithographic polymerization of diacetylene-containing phospholipid bilayers studied by multimode atomic force microscopy. *Langmuir* **2003**, *19*, 6994-7002.
7. Ringsdorf, H.; Schlarb, B.; Venzmer, J., Molecular architecture and function of polymeric oriented systems: models for the study of organization, surface recognition, and dynamics of biomembranes. *Angew. Chem. Int. Ed.* **1988**, *27*, 113-158.
8. Spevak, W.; Nagy, J. O.; Charych, D. H.; Schaefer, M. E.; Gilbert, J. H.; Bednarski, M. D., Polymerized liposomes containing C-glycosides of sialic acid: potent inhibitors of influenza virus in vitro infectivity. *J. Am. Chem. Soc.* **1993**, *115*, 1146-1147.
9. Azzam, T.; Eisenberg, A., Control of vesicular morphologies through hydrophobic block length. *Angew. Chem. Int. Ed.* **2006**, *45*, 7443-7447.
10. Sharma, A.; Sharma, U. S., Liposomes in drug delivery: progress and limitations. *Int. J. Pharm.* **1997**, *154*, 123-140.
11. Le Meins, J. F.; Sandre, O.; Lecommandoux, S., Recent trends in the tuning of polymersomes' membrane properties. *Eur. Phys. J. E Soft Matter* **2011**, *34*, 1-17.
12. Bermudez, H.; Brannan, A. K.; Hammer, D. A.; Bates, F. S.; Discher, D. E., Molecular weight dependence of polymersome membrane structure, elasticity, and stability. *Macromolecules* **2002**, *35*, 8203-8208.
13. James, C. M. L.; Santore, M.; Bates, F. S.; Discher, D. E., From membranes to melts, rouse to reptation: Diffusion in polymersome versus lipid bilayers. *Macromolecules* **2002**, *35*, 323-326.
14. Rawicz, W.; Olbrich, K.; McIntosh, T.; Needham, D.; Evans, E., Effect of chain length and unsaturation on elasticity of lipid bilayers. *Biophys. J.* **2000**, *79*, 328-339.
15. Balasubramanian, V.; Onaca, O.; Enea, R.; Hughes, D. W.; Palivan, C. G., Protein delivery: from conventional drug delivery carriers to polymeric nanoreactors. *Expert Opin. Drug Deliv.* **2010**, *7*, 63-78.
16. Tanner, P.; Egli, S.; Balasubramanian, V.; Onaca, O.; Palivan, C. G.; Meier, W., Can polymeric vesicles that confine enzymatic reactions act as simplified organelles? *FEBS Lett.* **2011**.
17. Marsh, D., *Handbook of Lipid Bilayers, Second Edition*. Taylor & Francis: **2010**.
18. Chen, Q.; Schönherr, H.; Vancso, G. J., Mechanical properties of block copolymer vesicle membranes by atomic force microscopy. *Soft Matter* **2009**, *5*, 4944-4950.
19. Yu, K.; Eisenberg, A., Bilayer morphologies of self-assembled crew-cut aggregates of amphiphilic PS-b-PEO diblock copolymers in solution. *Macromolecules* **1998**, *31*, 3509-3518.

20. Lim Soo, P.; Eisenberg, A., Preparation of block copolymer vesicles in solution. *J. Polym. Sci., Part B: Polym. Phys.* **2004**, *42*, 923-938.
21. Jaskiewicz, K.; Larsen, A.; Lieberwirth, I.; Koynov, K.; Meier, W.; Fytas, G.; Kroeger, A.; Landfester, K., Probing Bioinspired Transport of Nanoparticles into Polymersomes. *Angew. Chem. Int. Ed.* **2012**, *124*, 4691-4695.
22. Jaskiewicz, K.; Makowski, M. M.; Kappl, M.; Landfester, K.; Kroeger, A., Mechanical Properties of PDMS-b-PMOXA Polymersomes Probed by AFM. *Langmuir* **2012**, *28*, 12629-12636.
23. Kita-Tokarczyk, K.; Grumelard, J.; Haefele, T.; Meier, W., Block copolymer vesicles—using concepts from polymer chemistry to mimic biomembranes. *Polymer* **2005**, *46*, 3540-3563.
24. Pencer, J.; Hallett, F. R., Effects of vesicle size and shape on static and dynamic light scattering measurements. *Langmuir* **2003**, *19*, 7488-7497.
25. Kroeger, A.; Deimede, V.; Belack, J.; Lieberwirth, I.; Fytas, G.; Wegner, G., Equilibrium length and shape of rodlike polyelectrolyte micelles in dilute aqueous solutions. *Macromolecules* **2007**, *40*, 105-115.
26. Dimova, R.; Seifert, U.; Pouligny, B.; Förster, S.; Döbereiner, H. G., Hyperviscous diblock copolymer vesicles. *Eur. Phys. J. E Soft Matter* **2002**, *7*, 241-250.
27. Lee, J. C.; Bermudez, H.; Discher, B. M.; Sheehan, M. A.; Won, Y. Y.; Bates, F. S.; Discher, D. E., Preparation, stability, and in vitro performance of vesicles made with diblock copolymers. *Biotechnol. Bioeng.* **2001**, *73*, 135-145.
28. Radmacher, M., Measuring the elastic properties of living cells by the atomic force microscope. *Methods in cell biology* **2002**, *68*, 67-90.
29. Dubreuil, F.; Elsner, N.; Fery, A., Elastic properties of polyelectrolyte capsules studied by atomic-force microscopy and RICM. *Eur. Phys. J. E Soft Matter* **2003**, *12*, 215-221.
30. Delorme, N.; Fery, A., Direct method to study membrane rigidity of small vesicles based on atomic force microscope force spectroscopy. *Phys. Rev. E.* **2006**, *74*, 030901.
31. Park, J. W., Sulfatide incorporation effect on mechanical properties of vesicles. *Colloids Surf., B* **2010**, *80*, 59-62.
32. Egli, S.; Nussbaumer, M. G.; Balasubramanian, V.; Chami, M.; Bruns, N.; Palivan, C.; Meier, W., Biocompatible Functionalization of Polymersome Surfaces: A New Approach to Surface Immobilization and Cell Targeting Using Polymersomes. *J. Am. Chem. Soc.* **2011**, *133*, 4476-4483.
33. Peng, X.; Zhang, L., Formation and morphologies of novel self-assembled micelles from chitosan derivatives. *Langmuir* **2007**, *23*, 10493-10498.
34. Reissner, E., Stresses and small displacements of shallow spherical shells. *J. Math. Phys* **1946**, *25*, 80-85.
35. Evans, E. A., Bending resistance and chemically induced moments in membrane bilayers. *Biophys. J.* **1974**, *14*, 923-931.
36. Landau, L. D.; Lifschitz, E. M., *Theory of Elasticity*. Pergamon Press: New York, **1986**.
37. Christenson, H., Adhesion and surface energy of mica in air and water. *J. Phys. Chem.* **1993**, *97*, 12034-12041.
38. Liang, X.; Mao, G.; Simon Ng, K., Probing small unilamellar EggPC vesicles on mica surface by atomic force microscopy. *Colloids Surf., B* **2004**, *34*, 41-51.
39. Liang, X.; Mao, G.; Ng, K., Mechanical properties and stability measurement of cholesterol-containing liposome on mica by atomic force microscopy. *J. Colloid Interface Sci.* **2004**, *278*, 53-62.

40. Evans, E.; Rawicz, W., Entropy-driven tension and bending elasticity in condensed-fluid membranes. *Phys. Rev. Lett.* **1990**, *64*, 2094-2097.
41. Lee, C. H.; Lin, W. C.; Wang, J., All-optical measurements of the bending rigidity of lipid-vesicle membranes across structural phase transitions. *Phys. Rev. E.* **2001**, *64*, 020901.
42. Smith, K. A.; Jasnow, D.; Balazs, A. C., Designing synthetic vesicles that engulf nanoscopic particles. *J. Chem. Phys.* **2007**, *127*, 084703.
43. Hallett, F.; Watton, J.; Krygsman, P., Vesicle sizing:: Number distributions by dynamic light scattering. *Biophys. J.* **1991**, *59*, 357-362.
44. Mornet, S.; Lambert, O.; Duguet, E.; Brisson, A., The formation of supported lipid bilayers on silica nanoparticles revealed by cryoelectron microscopy. *Nano Lett.* **2005**, *5*, 281-285.
45. Yue, T.; Zhang, X., Cooperative Effect in Receptor-Mediated Endocytosis of Multiple Nanoparticles. *ACS nano* **2012**, *6*, 3196-3205.
46. Peterlin, P.; Arrigler, V.; Haleva, E.; Diamant, H., Law of corresponding states for osmotic swelling of vesicles. *Soft Matter* **2012**, *8*, 2185-2193.

## Chapter 6. Summary and Outlook

Transmembrane transport of nanoparticles can be imitated by an artificial polymeric membrane system with suitably designed physical parameters. The process itself can be driven by physical parameters of the system even when cell membrane proteins and other bio-active components as well as supplementary energy are missing. Due to the absence of any external stimuli, curvature-mediated attractive interactions (strong adhesive interactions) between nanoparticles and polymersomes are assumed to be the driving force for this process. A balance between the fluidity of the membrane and a short-ranged adhesive potential, given by the critical ratio of the geometric radii of the nanoparticles and polymersomes, is of importance.

Optical techniques as photon correlation and fluorescence correlation spectroscopies confirm strong adhesive interactions between polymersomes and nanoparticles through the selective probing of the involved species. Rapid internalization of the particles by polymersomes is observed only above a critical threshold particles concentration. The nanoparticles concentration affects the strength of the polymersomes/nanoparticles interactions and thus the number of incorporated particles can be tuned by a proper selection of their initial concentration. In addition to the effect of the concentration the phenomenon of nanosized particles incorporation by polymeric model membranes is found to be also strongly size dependent as it is known from the cellular systems. In this respect, the analogue behavior of the present artificial model system underlines the important role of physical parameters to trigger nanoparticles uptake even when all biofunctional molecules and/or supplementary energy are missing. Over a certain range of nanoparticles concentrations polymersomes were able to incorporate SiO<sub>2</sub> nanoparticles with sizes ranged from  $R_{h\ NP} = 14$  nm to 57 nm via an invagination and subsequent fission of the bilayer membrane. The fact that transmembrane transport of nanoparticles can be performed by

an artificial model system without any additional stimuli has a fundamental impact on the understanding, not only of the nanoparticle invagination process but also of the interaction of nanoparticles with biological as well as polymeric membranes. Many detailed studies can be performed in much less complex systems than the cell. Detailed investigations of size, shape and surface dependence of particle uptake can be carried out utilizing this artificial platform and can then be applied in living systems.

The designed minimal model system can be further modified and specialized to finally provide a generic platform for fundamental understanding, and an efficient tool for the preparation of smart nanoscaled systems for biomedical applications and nanotoxicology research. This project could go further in diverse direction, just to name few of them:

- Variation of the membrane thickness and further membrane proteins incorporation would bring this system closer to the real membranes. The influence of the proteins on membrane dynamics and mechanical response is of a great importance.
- Modification of the polymersomes surface would give an interesting insight into the incorporation process. Polymersomes utilized in frame of this thesis have positively charged surface (piperazyl groups) which is opposite to the negatively charged membrane surface. Adjusting the polymersomes surface to mimic closely cell membrane surface would allow a direct comparison between polymersomes and cells (number of incorporated particles, kinetics of the process).
- The influence of the polymersome size on the uptake mechanism is also of importance. Changing the size of polymersomes with fixed size of the nanoparticle would not only influence the nanoparticle/polymersomes surface ratio but also the curvature which was found to have great influence on the incorporation process.

- In addition to size and concentration uptake which was studied, shape dependent uptake studies are still missing. Here gold nanoparticles and gold nanorods seem to be perfect candidates. Both of them are commercially available, well defined and stable. A prominent spectroscopic feature of noble metal nanoparticles, so-called surface plasmon resonance, gives rise to a sharp and intense absorption band in the visible range. In addition to being size-dependent, the surface plasmon resonance band is also extremely sensitive to changes in the refractive index of the medium surrounding the particle. In this context, the nanoparticles have an inherent sensing ability. Any species adsorbed to the nanoparticle surface will manifest a color change (shift in the SPR peak position) proportional to the magnitude of the change in the refractive index near the nanoparticle surface. Above mentioned properties of gold would let us precisely follow their uptake by polymersomes. They would act as tracers which location can be precisely distinguish.
- Detailed selective kinetics studies should be delivered. Kinetics measurement presented in this thesis probe the time from nanoparticles addition to polymersomes mixture to the moment of reaching the equilibrium. It means that an approximated time include not only single events of a nanoparticle passage through the membrane but also time which particles took to be distributed in the dispersion. By the proper adjustment of the system detailed confocal or STED microscopy studies would deliver information about the time required for the nanoparticles to cross the membrane. This could also be achieved by the application of the selective technique which would allow a precise monitoring of the refractive index change inside polymersomes.



## *Curriculum Vitae and Publications*

**Name:** Karmena Izabela Jaśkiewicz

**Date of Birth:** 11.09.1984

**Place of Birth:** Zgorzelec, Poland

### **Education:**

- 10/2003 – 09/2008    **M.Sc. Eng. Studies**  
Wroclaw University of Technology, Wroclaw, POLAND  
Faculty: Chemistry  
Field of study: Material Science  
Specialization: Engineering of macromolecular materials  
Master thesis: Structure and phase behavior in organic-inorganic hybrid materials  
Supervisor: Dr. Adam Kiersnowski
- 01/2008 – 04/2008    **Leonardo da Vinci fellowship**  
Max Planck Institute for Polymer Research Mainz, GERMANY  
Work on crystallization behavior of polymers near inorganic surface  
Supervisor: Dr Silke Rathgeber
- 10/2008-04/2009    **Scientific co-worker/ tutor**  
Wroclaw University of Technology, Wroclaw, POLAND  
Faculty: Chemistry  
Work on crystallization of poly(vinyl fluoride) in the presence of inorganic nanoparticles  
Supervisor: Prof. Jacek Pięłowski
- 05/2009-09/2009    **The International Max-Planck Research School for Polymer Materials Science Fellowship**  
Max Planck Institute for Polymer Research Mainz, GERMANY  
Work on ATRP polymerization of PMMA brushes in ionic liquids  
Supervisor: Prof. Jochen Gutmann

10/2009 – 09/2012 **PhD studies**

Max Planck Institute for Polymer Research Mainz, GERMANY

Max Planck Graduate Center (MPGC)

Supervisor: Prof. Katharina Landfester and Prof. George Fytas

### **Conferences:**

1. 454. WE-Heraeus-Seminar on Polymer-Nano-Particles Interactions: Concepts, Observations and Applications, March 28 – 31. 2010 Bad Honnef, Germany

Poster: *Endocytic internalization of nanoparticles into polymer vesicles: A model system to study transmembrane transport processes*

2. EUROMAT 2011, September 12-15.2011, Montpellier, France

Talk: *Bioinspired active transport of nanoparticles into polymeric vesicles probed by photon correlation spectroscopy*

3. Polymers for Advanced technologies, PAT2011, October 2-5.2011, Lodz, Poland

Talk: *Endocytosis-like transport of nanoparticles into polymeric vesicles*

4. International Association of Colloidal and Interface Scientists Conference, IACIS2012, May 13-18.2012, Sendai, Japan

Talk: *Active transport of nanoparticles into polymersomes probed by photon correlation spectroscopy*

Poster: *Active transport of nanoparticles into polymersomes probed by photon correlation spectroscopy* (Soft Matter Poster Prize Winner)

**Publications:**

1. **Jaskiewicz, K.;** Makowski, M. M.; Kappl, M.; Landfester, K.; Kroeger, A., Mechanical Properties of PDMS-*b*-PMOXA Polymersomes Probed by AFM. *Langmuir* **2012**, *28*, 12629–12636
2. **Jaskiewicz, K.;** Larsen, A.; Schaeffel, D.; Koynov, K.; Lieberwirth, I.; Fytas, G.; Landfester, K.; Kroeger, A., Incorporation of Nanoparticles into Polymersomes: Size and Concentration Effects. *ACS Nano* **2012**, *6*, 7254–7262
3. **Jaskiewicz, K.;** Larsen, A.; Lieberwirth, I.; Koynov, K.; Meier, W.; Fytas, G.; Kroeger, A.; Landfester, K., Probing bioinspired transport of nanoparticles into polymersomes. *Angew. Chem. Int. Ed.* **2012**, *124*, 4691-4695
4. Zabska, M.; **Jaskiewicz, K.;** Kiersnowski, A.; Szustakiewicz, K.; Rathgeber, S.; Piglowski, J., Spontaneous exfoliation and self-assembly phenomena in polyvinylpyrrolidone/synthetic layered silicate nanocomposites. *Radiat. Phys. Chem.* **2011**, *80*, 1125-1128

## *Declaration*

I hereby declare that I wrote the dissertation submitted without any unauthorized external assistance and used only sources acknowledged in the work. All textual passages which are appropriated verbatim or paraphrased from published and unpublished texts as well as all information obtained from oral sources are duly indicated and listed in accordance with bibliographical rules. In carrying out this research, I complied with the rules of standard scientific practice as formulated in the statutes of Johannes Gutenberg-University Mainz to insure standard scientific practice.

Karmena Izabela Jaśkiewicz

Mainz, September 03, 2012

# Appendix

## 1. Nanoparticles Used in Presented Studies

**Table S1.** Properties of the nanoparticles used in the presented model system.

	$R_h$ / nm	Surface	$\zeta$ -potential / mV	Fluorescent Dye	Excitation/ Emission	$dn/dc$ mLg <sup>-1</sup>	Source	Additional
SiO <sub>2</sub>	14	silanol groups	-14	unknown	485 nm / 510 nm	0.06	Kisker Biotech.	free dye excess
	25		-22					
	35		-29					-
	57		-38					
PS	16	sulfate groups	-23	PMI	479 nm / 540 nm	0.228	in house	Stabilized with Lutensol AT-50

## 2. Stability of PDMS-*b*-PMOXA Polymersomes at Different Temperatures

PDMS-*b*-PMOXA polymersomes are stable in the temperature range from 20 – 50°C. No significant changes of the size and the form factor were observed. The altered diffusion patterns are the result of different temperature and thus the viscosity of the solvent. They lead however to the same hydrodynamic radius of diffusing species. First trials with the nanoparticles uptake at different temperatures did not reveal any significant changes.

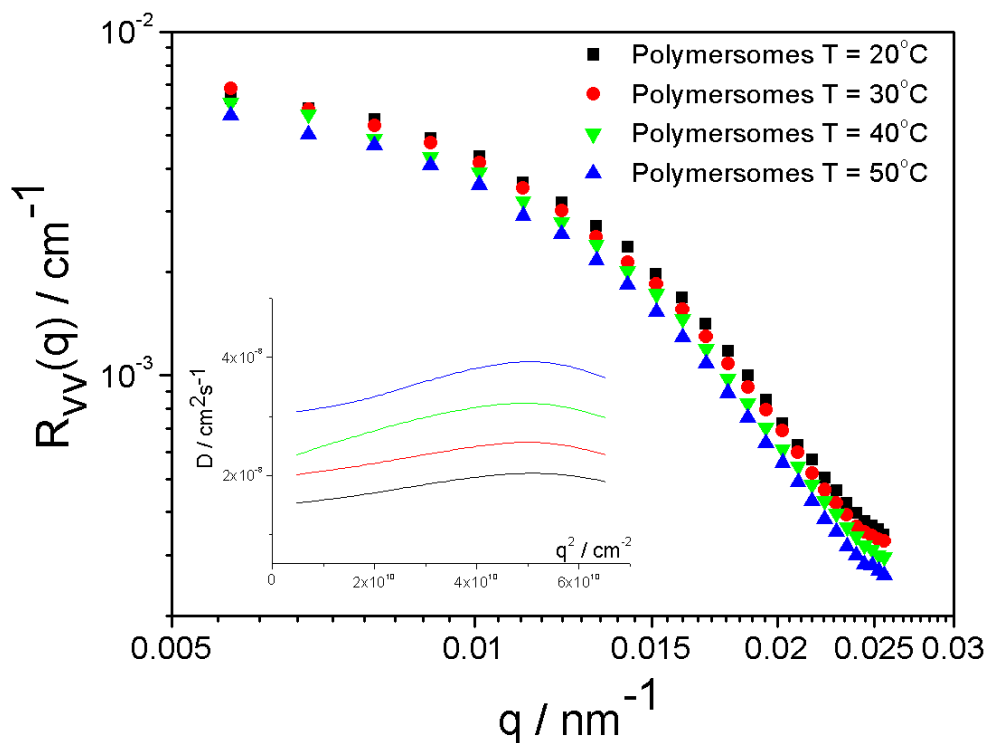


**Figure S1.** Absolute light scattering intensities of empty PDMS-*b*-PMOXA polymersomes with  $c = 0.045 \text{ gL}^{-1}$  at different temperatures; Inset: corresponding  $D(q)$

### 3. Influence of the pH on the PDMS-*b*-PMOXA Polymersomes

#### Stability

Stability of the PDMS-*b*-PMOXA polymersomes at different pH was investigated using sodium phosphate buffers of pH values vary from 2.5 to 9.5. Desired amount of polymersomes prepared in Milli-Q water was diluted using sodium phosphate buffers instead of water. Polymersomes were stable in the buffer solution of pH = 2.5 and pH = 9.5; change in the form factor and size of dispersed polymersomes was observed at pH = 7.0. The issue has to be investigated in details not only for the polymersomes itself but also with the focus on the influence of the solution pH on the nanoparticles uptake. Variation of the interactions strength

could lead to the different uptake pathways and/or different kinetic of the process. Changes in the pH value could act as a switch between interacting and non-interacting species.

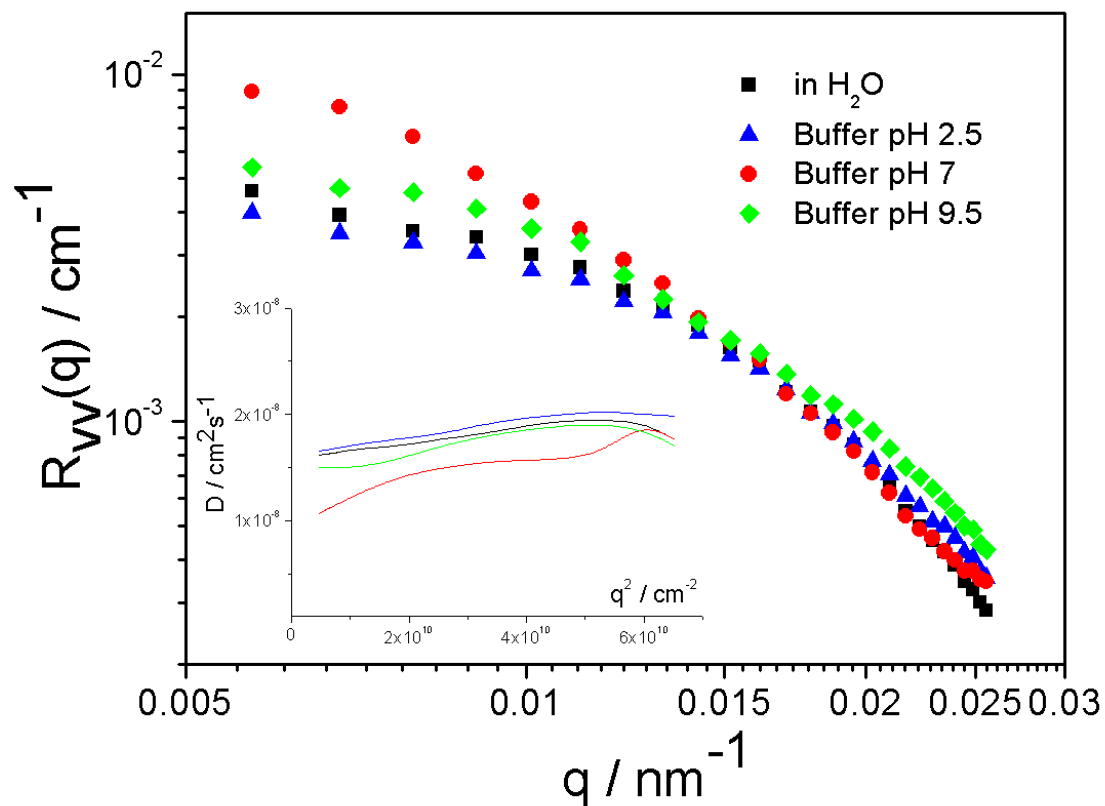


**Figure S2.** Absolute light scattering intensities of empty PDMS-*b*-PMOXA polymersomes with  $c = 0.045 \text{ gL}^{-1}$  in dispersion of different pH values; Inset: corresponding  $D(q)$